Parameterizing Ion–Lipid Interactions from Local Clusters to Reproduce Bulk and Interfacial Properties in Lipid Bilayers

by

Matthew W. Saunders

A thesis submitted in partial fufillment
of the requirements for the degree of
Doctorate of Philosophy in Biology
with a concentration in Cell & Molecular Biology
Department of Molecular Biosciences
College of Arts and Sciences
University of South Florida

Co-Major Professor: Sameer Varma, Ph.D.
Co-Major Professor: Sagar Pandit, Ph.D.
Jianjun Pan, Ph.D.
Libin Ye, Ph.D.
Stanley Stevens, Ph.D.

Date of Approval:

TBD

Keywords: Molecular Dynamics, ???

Contents

List of Tables

List of Figures

Abstract

1 Introduction[1]

1.1 Molecular Simulations

1.1.1 Classical Molecular Dynamics

Molecular Dynamics utilizes computers to simulate systems of molecules in order to study how structure changes with time, and the specific ways that different atomic and molecular species interact. This is done by first creating a model for the Hamiltonian of the system – a "force-field". This consists firstly of the terms for how atoms bond to each other, how these bonds move and stretch, and how they rotate around each other; classical models usually use harmonic potentials for bond and angle stretching and bending, and dihedrals are described using periodic functions.[1] In addition to the bonded terms, we have the non-bonded terms — energy from electrostatic interactions, typically described by Coulomb's law, and dispersion interactions (Van der Waals, or VdW) which arise from instantaneous dipole–induced dipole effects.[1] These are most often modeled using a Lennard–Jones (LJ) potential,[1,2] though other forms are also common, such as the Buckingham (exp–6) potential,[1,3] which replaces the steep r^{-12} repulsive wall with a short-range exponential. In addition to these two, there are many other functional forms used to describe VdW and dispersion interactions, but they are far less common. An example of this Hamiltonian can be seen here:

$$E_{\text{total}} = E_{\text{bonded}} + E_{\text{nonbonded}} \tag{1.1}$$

$$E_{\text{bonded}} = \sum_{\text{bonds}} k_r(r - r_0)^2 + \sum_{\text{angles}} k_\theta(\theta - \theta_0)^2 + \sum_{\text{dihedrals}} V_n \left[1 + \cos\left(n\phi - \gamma\right)\right] \tag{1.2}$$

$$E_{\text{nonbonded}} = \sum_{i<j} \left[4\epsilon_{ij} \left(\left(\frac{\sigma_{ij}}{r_{ij}} \right)^{12} - \left(\frac{\sigma_{ij}}{r_{ij}} \right)^{6} \right) + \frac{q_i q_j}{4\pi\epsilon_0 r_{ij}} \right] \tag{1.3}$$

[1] Will I be reusing part of a publication here???

By using this set of terms one can compute the potential energy of a particular configuration of particles. The forces obtained from the potential energy are used in Newton's equations of motion, which are numerically integrated — most often with algorithms such as the velocity-Verlet method — to update positions and velocities at each time step.[1] The energy of the new configuration can be computed, and the simulation continues. Thus, the careful development and improvement of a force-field is critical to reproduce valid results that can help us understand what is seen in experiments.

1.1.2 *Ab initio* calculations and Density Functional Theory

Do we really want to get into this? Just enough to understand why we are doing this at all... especially since this is our target data! We can talk briefly about the methods and things, enough to introduce pbe0+vdw...

1.2 Comparing Molecular Simulations with Experimental Results

1.2.1 SAXS (and SANS) – and other properties obtained from density distributions

Systems of crystals are often studied using diffraction or scattering experiments. In the case of lipid bilayers, we often use Small-Angle scattering of x-rays (SAXS) or neutrons (SANS) to study the bilayer structure. Lipid bilayers are smectic crystals, and thus give scattering patterns that look like concentric circles – these circles are the bilayer form-factor. This form-factor is the reciprocal-space structure of the bilayer, but phase information of each lobe is lost. Thus, a simple reverse-transformation cannot be perfomed. In order to produce the appropriate density distribution, one can approximate the number density of bilayer parts as gaussian functions, and compute the appropriate scattering density from that. This can then be transformed via a cosine transform into a form-factor. The gaussians are then adjusted until the resulting form-factor fits the data from the experiment.

1.2.2 Electrostatic and dynamic results... such as GC-theory!

1.2.3 Diffusion coefficients

1.2.4 Order parameters

2 A high dimensional parameter search method to determine force field mixing terms in molecular simulations[1]

2.1 Abstract

Molecular dynamics (MD) force fields for lipids and ions are typically developed independently of one another. In simulations consisting of both lipids and ions, lipid-ion interaction energies are estimated using a predefined set of mixing rules for Lennard-Jones (LJ) interactions. This, however, does not guarantee their reliability. In fact, compared to the quantum mechanical reference data, Lorentz-Berthelot mixing rules substantially underestimate binding energies of Na^+ ions with small molecule analogues of lipid headgroups, yielding errors on the order of 80 and 130 kJ/mol, respectively for methyl acetate and diethyl phosphate. Previously, errors associated with mixing force fields have been reduced using approaches like 'NB-fix' in which LJ interactions are computed using explicit cross terms rather than those from mixing rules. Building on this idea, we derive explicit lipid-ion cross terms that also may implicitly include many-body cooperativity effects. Additionally, to account for interdependency between cross terms, we optimize all cross terms simultaneously by performing high-dimensional searches using our ParOpt software. The cross terms we obtain reduce the errors due to mixing rules to below 10 kJ/mol. MD simulation of lipid bilayer conducted using these optimized cross terms resolve the structural discrepancies between our previous simulations and small-angle X-ray and neutron scattering experiments. These results demonstrate that simulations of lipid bilayers with ions that are accurate up to structural data from scattering experiments can be performed without explicit polarization terms. However, it is worth noting that such NB-fix cross terms are not based on any physical

[1]Portions reprinted with permission from Matthew Saunders, Vered Wineman-Fisher, and Eric Jakobsson, *High-Dimensional Parameter Search Method to Determine Force Field Mixing Terms in Molecular Simulations*, *Langmuir*, American Chemical Society, March 1, 2022.

principle; a polarizable lipid model would be more realistic, and is still desired. Our approach is generic and can be applied to improve accuracies of simulations employing mixed force fields.

2.2 Introduction

Cellular membranes function as highly dynamic interfaces with many diverse components, including lipids, peptides, carbohydrates, and charged species like ionic salts. Studies of these complex systems often benefit from computational methods, particularly molecular dynamics (MD) simulations.[4] In our previous MD simulation studies, we characterized the effects of various monovalent and divalent ions on model 1-palmitoyl-2-oleoyl-sn-glycero-phosphatidylcholine (POPC) bilayers.[5–8] We reported that ions modify POPC bilayer structure with significant effects on area per lipid and bilayer thickness. Similar results were also reported in MD simulations by others.[9–13] Experiments characterizing bilayer structures in the presence of ions have not been as numerous as simulation studies. However, experimental findings indicate that dissolved salts at physiological concentrations do not modify bilayer structure significantly.[14–16] Specifically, Petrache *et al.* performed small angle X-ray scattering (SAXS) experiments on multilamellar vesicles of 1,2-dilauroyl-sn-glycero-3-sn-glycero-phosphatidylcholine as well as other lipids in KCl and BrCl salt solutions, and reported that while small changes can be seen in the X-ray scattering form-factor due to the salts, the fitted electron density profiles are essentially identical for systems with and without salt.[15] Similarly, Pabst *et al.* found no significant change in bilayer structure for POPC bilayers in NaCl salt at or below 1 M concentration.[14] Furthermore, Uhrikova *et al.* reported small structural changes using small angle neutron scattering (SANS) experiments on 1,2-dipalmitoyl-sn-glycero-3-sn-glycero-phosphatidylcholine vesicles interacting with $CaCl_2$.[16] Taken together, these results point to a general discrepancy between structural data from MD simulations and scattering experiments.

The reliability of MD simulations depends greatly on the force field (FF) parameters used for describing intra- and inter-molecular interactions. While FF parameters of lipids,

including ours, are developed with great accuracy and care, we note that they are derived in the absence of ions. Similarly, ion parameters are also derived in the absence of lipids.[17] When simulations of bilayers are conducted in salt solution, ion-lipid interactions are computed using FF mixing rules. In our previous MD simulations of POPC bilayers in salt solutions, we employed our gromos43A1-S3 lipid FF parameters[18] that were developed for use with SPC/E water to determine lipid-lipid and lipid-water interactions. Ion-ion and ion-water interactions were described using Joung and Chetham[17] parameters, also developed for use with SPC/E water. Lipid-ion interactions were estimated using Lorentz-Berthelot (LB) mixing rules for Lennard-Jones (LJ) components , and there was a significant change in bilayer structure compared to that of the bilayer without salt despite the relatively small initial salt concentration of 200 mM. Does this suggest that the discrepancy between our MD predictions and experiments is the result of the LB mixing rules? Note that none of the MD simulations of lipid-ion interactions discussed above include explicit terms to describe electronic polarization. Errors in mixing rules may, therefore, emerge if the high electric fields of ions induce cooperativity effects in lipid groups differently from those in water. Quantum mechanical (QM) studies, in fact, suggest that many-body cooperativty effects, such as polarization depend strongly on ion-coordinator chemistry.[19,20] It has also been postulated that these effects, and specifically electronic polarization may play an important role in determining the structure and dynamics of lipid bilayers – especially when interacting with ions.[21–25]

Small deviations from LB rules have been shown to have a significant effect on the behavior of systems of particles,[26] and it is possible that a systematic tuning of these parameters could be used to correct for artifacts in a simulation.[20,27–36] Such a 'Non-Bonded-fix' (NB-fix) strategy has been shown to effectively improve protein-ion , protein-nucleotide, and ion-membrane interactions while retaining the commonly used form of the LJ 6-12 potential .[20,27–36] Building on this idea, here we propose a more general approach to optimize interaction cross terms for use with the 6-12 potential, and also validate its prediction in

condensed phase simulations. We expand on the NB-fix method by (a) optimizing all ion-lipid LJ cross terms simultaneously, and (b) implicitly including many-body cooperativity effects. We consider simultaneous optimization of all cross terms to be critical, because of their strong, interdependent correlation with the target results.[37] This high-dimensional optimization is performed using our software tool ParOpt.[37,38] Many-body cooperativity effects have been shown to be a major contributor to ion binding[19] . Thus, it is important to include them in lipid bilayer simulations where ions are known to coordinate simultaneously with multiple ligands.[7]

We show that the cross terms we obtain from this approach substantially improve ion-lipid interaction energies over those obtained from LB mixing rules. MD simulation of a POPC bilayer in 200 mM NaCl initial solution conducted using these optimized cross terms also resolves the structural discrepancies between our previous MD simulations and small-angle X-ray and neutron scattering experiments at low salt concentrations.

2.3 Methods

The method proposed here is generic and can be applied to any pair of interacting species that use cross terms, and ensures that we are reproducing macroscopic results based on the most accurate representation of the local inter-molecular interactions. We chose small molecular analogues of the important ion binding sites in the polar region of phospholipid molecules. These molecules were also used as building block molecules in development of our lipid FF.[6,18] Specifically, we selected methyl–acetate (MeAc) to represent the ester group binding the acyl–chain to the glycerol backbone, and diethyl–phosphate (DePh) to represent the headgroup phosphate and surrounding carbons (See insert on figure 2.2). The overall goal was to take the substitution energy of ions from water to the selected molecules, along with the corresponding geometries, all computed using a benchmarked quantum mechanical framework, and optimize the interaction cross terms to reproduce these target data within the Molecular Mechanics force-field.

Combined analysis of results from experiments and *ab initio* molecular dynamics simulations in the aqueous phase suggest that Na^+ ions prefer to directly coordinate with $\sim 5-6$ water molecules .[39–43] However, when coordinating with MeAc molecules, steric hindrance restricts the number of binding partners to fewer than four coordinating molecules. Thus, we limited the size of our MeAc clusters to up to four molecules around an ion. DePh has resonant oxygens on each molecule that potentially act as two binding sites, so we limited these clusters to up to two molecules around a Na^+. These were compared to the clusters of Na^+surrounded by up to four water molecules. In this work, we forgo modifying terms for Cl^-, as we have found in our previous work that anions do not bind to the bilayer headgroup significantly, and remain solvated by water molecules.[6]

2.3.1 Quantum Mechanical Calculations

Target data for our parameter optimization consisted of energies and geometries computed using a benchmarked density functional theory as implemented in the FHI-Aims software package.[44] Geometry optimizations were performed on the Na^+–$(Water)_n$, Na^+–$(MeAc)_n, n \leq 4$, and Na^+–$(DePh)_m, m \leq 2$ clusters. These clusters were first optimized using the MM force field used in Kruczek *et al.*and Saunders *et al.*[6,8] MM optimized structures were then further optimized using the PBE0 functional[45,46] with self-consistent vdW corrections.[47] We used the *really tight* basis sets included in the FHI–aims software. This functional and basis set combination has been shown to perform well compared to experiment and high-level quantum methods for many different chemistries of ion-ligand clusters.[20,48,49] Optimizations were performed with a force maxima of 10^{-3} eV/Å , with total energies converged to within 10^{-6} eV. We computed substitution energies of these clusters as:

$$\begin{aligned} E^n_{\mathrm{MeAc}} &= E_{\mathrm{Na^+\text{–}(MeAc)}_n} - nE_{\mathrm{MeAc}} - E_{\mathrm{Na^+\text{–}(Water)}_n} + nE_{\mathrm{Water}} \\ E^n_{\mathrm{DePh}} &= E_{\mathrm{Na^+\text{–}(DePh)}_n} - nE_{\mathrm{DePh}} - E_{\mathrm{Na^+\text{–}(Water)}_{2n}} + 2nE_{\mathrm{Water}}, \end{aligned} \tag{2.1}$$

where n is the number of solvent molecules (see tables 2.1 and table 2.2 for all of the QM data used for this computation). These substitution energies and corresponding configurations were used as targets for the parameter optimization.

Table 2.1: Total energies of systems of small molecules from QM calculations. These energies are computed by taking the total energy from the final step of geometry optimization on clusters of our selected small molecules around a single Na^+following the procedure outlined in the methods section. We computed binding energies using these values.

Cluster Size	Water (kJ/mol)	MeAc (kJ/mol)	DePh (kJ/mol)
1	-9.048×10^5	-1.130×10^6	-2.528×10^6
2	-1.609×10^6	-1.834×10^6	-4.630×10^6
3	-2.313×10^6	-2.538×10^6	N/A
4	-3.018×10^6	-3.243×10^6	N/A

Table 2.2: Self energies of isolated molecules. These are computed by performing geometry optimization on an isolated molecule following the procedure outlined in the methods.

	Water	Na^+	MeAc	DePh
Energy (kJ/mol)	-2.006E+05	-4.253E+05	-7.042E+05	-2.102E+06

2.3.2 Parameter Optimization

Parameter optimization is performed using our ParOpt software package .[37,38] This software is available for download at `https://csmlabfs1.cas.usf.edu/Sites`. We utilized the Nelder-Meade method to perform a search to simultaneously optimize all σ_{ij} and ϵ_{ij} cross terms of Na^+ ions with MeAc and DePh molecules. Specifically, there are seven atom types in these two small molecules (table 2.4), and so we optimized 14 cross terms for the 6-12 LJ potential. Error was determined by comparing the optimized geometries and substitution energies of each new parameter set to the reference data from QM.

Boundary constraints were imposed on ϵ_{ij} and σ_{ij} to keep the search space finite. Table 2.3 shows all of the constraints placed on the parameter search. Additionally, we constrained the NA–OM σ_{ij} to be smaller than the σ_{ij} for NA–P to avoid unphysical conformations of DePh. Boundary constraints are enforced by reassigning σ_{ij} or ϵ_{ij} values that violate the bound to the boundary value. Throughout optimization we monitored constraint violations and ensured that we did not select a final parameter set that is the result of a constraint violation. High–dimensional optimizations of this nature may not have a unique solution; thus, we performed 200 independent optimizations with random initial parameter values. We compared the parameter sets that best improved the substitution energy without significantly compromising the conformational geometries.

Figure 2.1a illustrates a representative NM–trajectory that follows NM–error as a function of optimization step. In this case, the NM–error is defined as an equally–weighted combination of the mean absolute error of the substitution energy and the distances between each atom in the cluster and the Na^+ ion. Each NM–move used is illustrated as a point on the error curve (see Fogarty *et al.* for complete description of NM algorithm and moves[37]). The insert shows the root-mean squared distance (RMSD) between the simplex vertices at each step. As is typical with the NM method, error drops exponentially during the initial steps, and slows down towards the end of the optimization process. The termination condition for the optimization run is the collapse of the NM–simplex (defined by the RMSD $\leq 10^{-10}$). Figure 2.1b shows all of the 291,870 σ_{ij}-ϵ_{ij} pairs tested between Na^+ ions and the non–carbon atoms in the 200 independent optimization runs, and provides a visual perspective of the

Table 2.3: Nelder–Meade constraints. These values were used to constrain the parameter search space during the NM–optimization.

	NA-CH3		NA-CH2		NA-CO*		NA-OA,-OM*,-O*,-P		Additional Constraints
	Min	Max	Min	Max	Min	Max	Min	Max	N/A
σ_{ij}(nm)	0.2	0.5	0.2	0.5	0.2	0.5	0.2	0.5	$\sigma_{ij}^{\text{NA-OM*}} \leq \sigma_{ij}^{\text{NA-P}}$
ϵ_{ij}(kJ/mol)	0	0.79	0	0.81	0	0.83	0.05	7	N/A

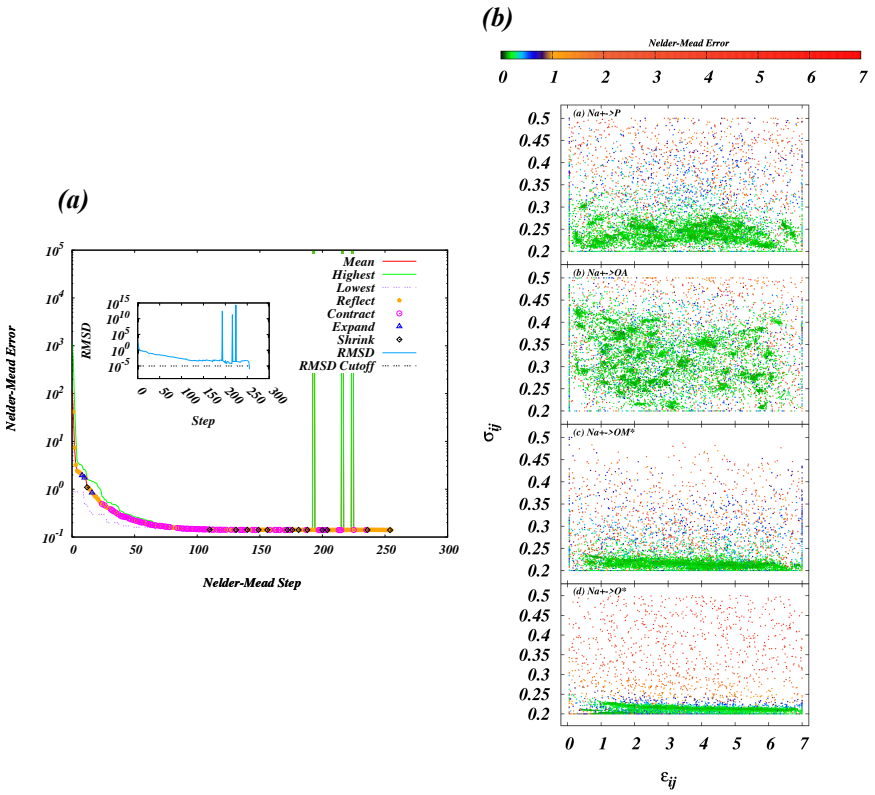

Figure 2.1: (a) Representative Nelder–Meade (NM) optimization run. Each point represents a move that the NM simplex can make while navigating the parameter space (See Fogarty *et al.* for a full description of the Nelder–Meade algorithm and available moves[37]). The insert illustrates the RMSD between the simplex vertices. The optimization is considered converged when the simplex collapses, which is defined by an RMSD $\leq 10^{-10}$. (b) Map of all σ_{ij} and ϵ_{ij} tested for interactions of Na^+ with non–carbon atom types in the 200 optimizations performed to find our final optimized set of cross terms. A total of 291,870 combinations of parameters were tested, shown color-coded according to their NM error.

sampled parameter space. The parameter set that yielded the lowest error, as discussed in the results section, was chosen to perform MD simulations of a POPC bilayer.

2.3.3 Bilayer Construction

We first constructed a monolayer of POPC lipids by placing 100 lipids on a 10 nm by 10 nm grid, with excess space between the lipids to avoid overlaps in the lipid chains. Then we reflected this grid to create the second leaflet of the bilayer, resulting in a bilayer of 200 lipids.

Assuming a conservative estimate of one binding site per lipid, we need at least 200 Na^+ ions in bulk solvent at the beginning of the simulation to avoid complete depletion of bulk ions after equilibration. In order to do this we constructed a system with double the size of the solvent block used in our previous works.[6,7] This larger system was constructed by adding 60,000 waters to the system on a 3-D grid with excess space between waters, and randomly replacing water molecules with 216 $Na^+$and 216 Cl^-. This results in an initial concentration of 200 mM, similar to our previous simulations. This process resulted in a simulation box with dimensions 9.75 nm $\times$ 9.75 nm $\times$ 59.84 nm.

We energy-minimized the simulation box using the steepest descent algorithm with a force tolerance of 50 kJ $mol^{-1}nm^{-1}$. Neighbor searching was performed every 2 steps. The PME algorithm was used for electrostatic interactions with a cut-off of 1.6 nm. A reciprocal grid with a spacing of 0.12 nm^{-1} was used with 6th order B–spline interpolation. A single cut-off of 1.6 nm was used for van der Waals interactions.

We then performed a 200 ps constant pressure simulation at 290 K to ensure the system was relaxed enough for further annealing. The box dimensions at the end of this were 7.86 nm $\times$ 7.86 nm $\times$ 32.90 nm. Annealing was started at 400 K, and the system was cooled to the production simulation temperature of 300 K in steps of 10 K. Each step was simulated for 150 ps, giving a total annealing time of 1.5 ns. The annealing process shrunk the box dimensions to 7.97 nm $\times$ 7.97 nm $\times$ 32.14 nm. This final structure was used as the starting point for production run.

2.3.4 Molecular dynamics

All molecular dynamics simulations were performed with the GROMACS software package, version 5.1.6.[50–54] We have utilized the SPC/E model for all waters.[55] Lipid interaction terms are described using the parameters in the gromos43A1-S3 parameter set developed by our group in previous work.[18] The system temperature was held constant at the production run temperature of 300K using the Nosè–Hoover thermostat with a coupling constant of 0.5 ps.[56]

Pressure coupling was performed using the Parrinello-Rahman semiisotropic barostat, which held the system pressure constant at 1 atm with a coupling constant of 1.5 ps.[57] The P–LINCS algorithm was used to constrain all bonds in the system to allow for a 4 fs integration timestep.[58] Integration was carried out using the Verlet scheme, with neighbor-list updates taken on every other integration step. We used a cutoff of 16 Åfor short–range electrostatics. Beyond this cutoff, we have used the smooth particle–mesh Ewald summation method to describe electrostatics.[59] LJ interactions were calculated with a cutoff of 16 Å. For all systems described, we have simulated continuously for 0.7 μs.

Simulated trajectories were analyzed using a combination of GROMACS built–in analysis tools and in–house software developed on the GROMACS API.

2.4 Results and Discussion

2.4.1 Optimized Cross-Terms

The final optimized parameters are detailed in table 2.4 alongside the original parameters computed using LB rules. We immediately note a general trend of an increase in the value

Table 2.4: Force–field cross terms. Original terms, as used in the system simulated with LB rules were computed by applying Lorentz-Berthelot mixing rules to the LJ parameters of $Na^+$and each lipid component atom type. Optimized parameters are the result of the NM–optimization using ParOpt.[37,38] All constraints on the search space can be seen in figure 2.3

	Original		Optimized	
	σ_{ij}(nm)	ϵ_{ij}(kJ/mol)	σ_{ij}(nm)	ϵ_{ij}(kJ/mol)
NA-CH3	0.295	1.100	0.235	0.700
NA-CH2	0.312	0.772	0.237	0.809
NA-OA	0.256	1.120	0.211	3.035
NA-P	0.277	1.900	0.301	0.483
NA-OM*	0.252	1.221	0.211	1.445
NA-CO*	0.335	0.362	0.315	0.758
NA-O*	0.251	1.221	0.216	2.440

of ϵ_{ij} for the non-carbon atom types. With our constraints on the carbon atoms, we have nudged the optimization into gaining the binding energy by increasing the ϵ_{ij} for the specifically electronegative atoms. Values of σ_{ij} have changed, but remained close to the original values in general, suggesting that the optimum distance to the minimum energy of the LJ potential is estimated well by LB rules. We can also see that no values of σ_{ij} or ϵ_{ij} violate the constraints described in table S3 in supporting information. We examined substitution energies and corresponding conformational geometries by running energy minimization of the QM–optimized structures using the final parameter set. These were then analyzed using the GROMACS built–in energy and distance tools. The substitution energies and the conformations for this parameter set are shown in figure 2.2 and in figure 2.3, respectively. We can see that for MeAc we have substantially improved substitution energies relative to those obtained from using LB mixing rules, which started with an discrepancy of around 30–80 kJ/mol. We have also improved the relative substitution between the clusters of various sizes. The substitution energies for DePh have also improved by a similar magnitude. The conformational geometries are largely unchanged, with a general trend of the binding distance to OM shrinking on the order of 0.25 Å in DePh. This shrinkage is common when optimizing both energies and conformations with the relatively small number of free parameters corresponding to the LJ cross terms.[20]

We also note that the substitution energies for both molecule types improve more in the larger cluster sizes. Larger clusters are more relevant to the dense environment in the lipid headgroup region of the bilayer, as few, if any, ions bind to a single lipid at a time.[6] Furthermore, the substitution energy profile for MeAc has become much closer to that of the QM profile. Thus, these new parameters substantially improve the energetic balance between the lipid–ion, lipid–water and ion–water interactions.

The conformational geometries were mostly unchanged with the new parameter set, as even the original parameters do a good job in reproducing the QM–configurations. The least precise cluster appears to be for 4 MeAc, where the original LB parameters poorly

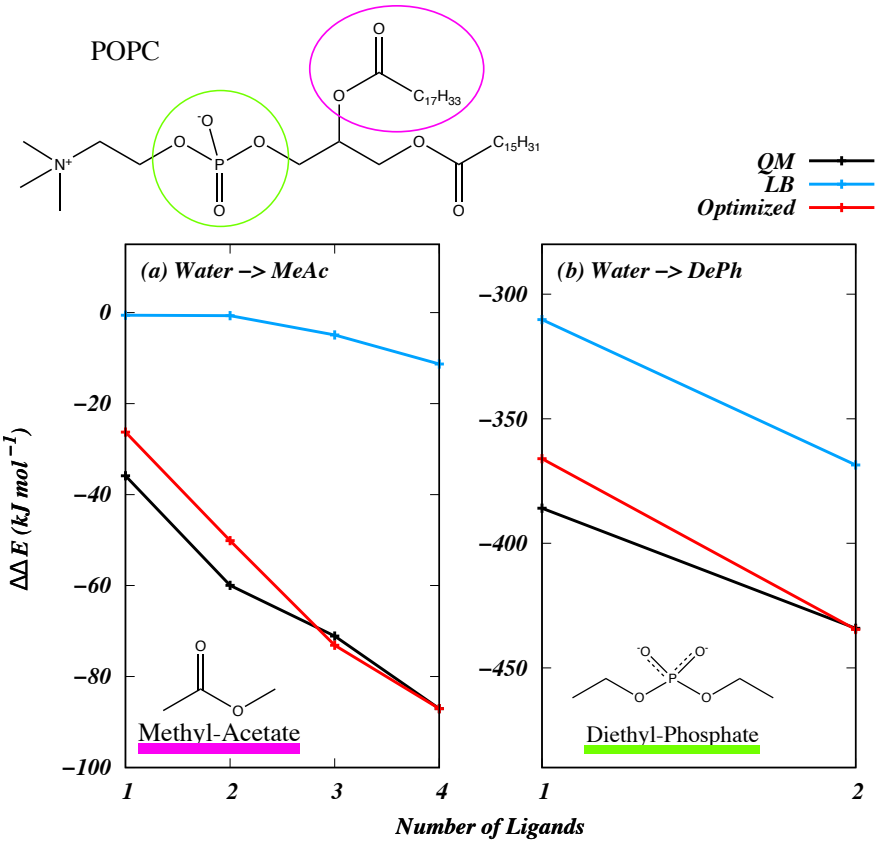

Figure 2.2: Substitution energies for Na^+ clusters computed as described in equation 2.1. In black we see the energies of systems computed using the standard mixing rules, in red we have the energies from benchmarked DFT, and in blue the optimized results. We see a significant error with the standard LB mixing rules, which is substantially improved with our new optimized cross terms. The insert shows an diagram of POPC, and the small molecules Methyl-Acetate (MeAc) and Diethyl-Phosphate (DePh) that were used to represent the major Na^+ interaction sites on the POPC molecule.

represent the symmetries exhibited in the QM data. Even with the improvement from our new parameters, we may be missing behavior from explicit polarization effects that cannot be captured properly by a non–polarizable model.[19]

2.4.2 Validation of Parameters

In order to characterize our new parameter set in a bilayer, we generated a 700 ns simulation of a bilayer of POPC lipids in NaCl salt solution, and we compared the results against a similar system that we simulated using LB rules in our previous works.[6,7] These older trajectories for systems both with salt and without will be referred to, respectively, as

LB and 'without salt.' We simulated our system with optimized cross terms, hence forth will be referred to as the 'optimized' system, long enough to equilibrate the number of bound ions (see figure 2.6). We will further characterize this ion binding in a subsequent section.

Bilayer Structure

Bilayer structural parameters can be seen in table 2.5. The phospholipid component

Table 2.5: Bilayer structural parameters. D_{hh} is the peak–to–peak distance from the electron density of the lipid bilayer, and is a measure of bilayer thickness. Bilayer thickness D_B and chain thickness $2D_C$ are computed from number densities of the solvent and the lipid chains, respectively. V_H, and V_C are the volumes of the headgroup and lipid chains computed using the method from Petrache *et al.*[60] V_L is the sum of V_H and V_C. Rows 7-11 contain kinetic parameters for ion binding to membrane. These parameters come from fitting the equation $N_b(t) = \frac{K_a}{K_a+K_d} N\left(1 - \exp\left[-\left(K_a + K_d\right)\left(t - t_0\right)\right]\right)$ to the data for the number of ions bound to the lipid bilayer across the simulation time. A is the asymptotic number of ions bound to the lipid bilayer, and can be used as the expected number of ions that will bind to the system at equilibrium. τ is the characteristic timescale of the fitted function. n_0 is the number of ions bound at the beginning of the production run of the simulation. K_D and K_A are the computed binding association and dissociation constants, and K_A/K_D is the binding rate constant.

	Without salt	LB	Optimized
D_{HH} (Å)	37.44 ± 1.07	40.18 ± 1.04	37.64 ± 0.88
D_B (Å)	36.54 ± 0.47	40.90 ± 0.31	39.36 ± 0.43
$2D_C$ (Å)	27.07 ± 0.34	30.33 ± 0.29	28.97 ± 0.34
V_H (Å^3)	310.68 ± 1.14	316.13 ± 0.83	314.81 ± 0.75
V_C (Å^3)	904.89 ± 1.28	891.79 ± 1.65	896.50 ± 1.19
V_L (Å^3)	1215.57 ± 1.00	1207.92 ± 1.57	1211.32 ± 1.21
K_A (ns^{-1})	N/A	$7.12\times10^{-3}\pm8.18\times10^{-5}$	$2.65\times10^{-3}\pm1.74\times10^{-5}$
K_D (ns^{-1})	N/A	$3.20\times10^{-3}\pm4.75\times10^{-5}$	$3.58\times10^{-3}\pm2.83\times10^{-5}$
A	N/A	74.51	91.88
τ (ns)	N/A	96.73	160.54
K_A/K_D	N/A	2.225	0.74

volumes V_H and V_C (lines 1 and 2) are computed following the procedure outlined by Petrache

et al.[60] The lipid chains are identified as starting at the first carbon attached to the lipid chain carbonyl oxygen, including the oxygen. The atom groups not part of the lipid chains are partitioned into the headgroup volume. We take the number–density of these component groups along with that of the solvent, and use them to optimize the objective function:

$$\Omega(v_i) = \sum_{z_j}^{\rho_s}(1 - \sum_{i=1}^{N_{\text{Groups}}} (\rho_i(z_j)v_i)^2), \tag{2.2}$$

In the equation above, $\rho_i(z_j)$ is the number density of the i component in the z_j slice of the box and v_i is the corresponding component volume. The component volumes are then multiplied by the corresponding number of particles per molecule per group – 32 for the chain particles, and 20 for the headgroup. This gives us the total volume per molecule for each group. The total lipid volume V_L (line 3 in table 2.5) is taken to be the sum of these two values. These remain relatively similar in all three systems, as this value is intrinsic to the lipid molecule and should not change with the inclusion of ions.

Structural data are obtained for lipid bilayers via small angle X-ray and neutron scattering experiments as a one–dimensional form–factor. Data are then fitted to a continuous function to retrieve number and electron densities for the various lipid components.[61,62] Our simulations allow us direct access to the electron densities and number densities. The entries in table 2.5 are determined from these densities.

Figure 2.4 shows the electron densities and corresponding bilayer form-factors. Form–factors are computed by taking the cosine–transform of the symmetrized electron densities. We note that the simulations carried out using LB rules produced a thicker bilayer and had different details at the peak region of the density. The new parameter set results in similar electron density to that of the system without salt. This is similar to the results reported by Petrache *et al.* and Pabst *et al.*, where for systems with less than 1 M NaCl, the differences in the electron densities were not discernible.[14,15] These electron densities are used directly

to measure the value of D_{hh}, defined as the peak–to–peak distance (see table 2.5 line 4). The new parameter set corresponds to a smaller D_{hh}, similar to the system without salt.

In addition to D_{hh}, different measures are used to assess the bilayer thickness that relies on the probability densities of different components of the system. It can be shown that D_B (see table 2.5 line 5) computed by integrating one minus the probability density of solvent and ions is equivalent to the computation of the Luzzati thickness of the total bilayer.[18,62] We define probability of finding a particular component in a slice of the box as,

$$P_i(z) = \frac{\rho_i(z)}{\sum_j^n \rho_j(z)}, \tag{2.3}$$

where $\rho_i(z)$ are the number densities for the component particles (i) of the system as a function of the z-position of each slice of the box, and the summation ranges over all components in the particular slice. Thus,

$$D_B = \int_{\text{Box length}} \big(1 - P_{\text{water+ions}}(z)\big)\, dz. \tag{2.4}$$

In table 2.5 line 2, the D_B is larger for the systems with ions, but the value obtained using our new parameter set is closer to that of the bilayer simulated without salt.

We use a similar definition of probability density for $2D_C$, computed from the probability distribution of the lipid chains. This component is defined by the hydrocarbon chains starting after the ester–linkage on both the Sn1 and Sn2 terminal of the lipid backbone. This value (line 6 in table 2.5) is increased in the system simulated with LB rules over the system without salt, as we reported in our previous work. However, the new parameter set yields a value similar to the system without salt, which is consistent with the smaller overall thickness of the bilayer simulated with optimized cross terms.

The differences in bilayer thickness are closely related to the packing of the lipid chains in the hydrophobic core of the bilayer. When the chains become more disordered, the bilayer thickness typically drops.[61] Lipid chain ordering can be determined experimentally

by performing NMR on specifically deuterated hydrocarbon chains. Since we lack hydrogen on our coarse–grained lipid chains, we cannot directly access the C–D ordering. Instead, we compute the chain order tensor $S_{\alpha\beta}$ defined as

$$S_{\alpha\beta} = \frac{1}{2}\left\langle 3\cos\theta_\alpha \cdot \cos\theta_\beta - \delta_{\alpha\beta}\right\rangle,$$

where the angles θ_α and θ_β are the angles between the molecular axis and the box z-direction. We then use this tensor to calculate the S_{CD} as

$$-S_{CD}^{\text{Saturated}} = \frac{2}{3}S_{xx} + \frac{1}{3}S_{yy} \tag{2.5}$$

for saturated carbons,[63] and as

$$-S_{CD}^{\text{Unsaturated}} = \frac{1}{4}S_{zz} + \frac{3}{4}S_{yy} \mp \frac{\sqrt{3}}{2}S_{yz} \tag{2.6}$$

for unsaturated carbons.[64] These values are plotted per each carbon in the lipid chain in figure 2.5. As reported in our previous simulations, the addition of salt has an ordering effect on the lipid chains. This effect is also seen in our new parameter set; however, the ordering is less pronounced, which is consistent with the notion that the bilayer structure is not significantly altered at physiological salt concentration.[14,15]

While this result indicates a structure more consistent with experimental results, the detailed structure of a lipid bilayer is a result of the delicate balance between ion–lipid, lipid–water, and ion–water interactions. In order to fully understand how our new parameter set has altered the overall bilayer structure, we next characterize the specific interactions between these moieties.

2.4.3 Membrane-Salt Interactions

Both ions and solvent compete for the binding sites on the lipid headgroup. As seen in figure 2.2, the new cross terms produce a relatively stronger interaction between $Na^+$and lipid headgroup components compared to that of the LB rules. Thus, there is potentially a reduction in the available binding sites for the solvent. To examine how the new cross terms have altered ion interactions with lipids in the bilayer, we first characterize the dynamics of ion binding to the lipid bilayer.

We define ion binding to the lipid bilayer when half or fewer of its first shell coordinators are not waters. In order to compute the equilibrium binding constant, we must determine the equilibrium number of bound ions to the lipid surface. Figure 2.6 shows the number of bound ions as a function of time over the entire duration of the simulation. We note that even after 700 ns of simulation time, the number of bound ions are not fully equilibrated. Thus, we use first–order reaction kinetics to estimate the asymptotic number of bound ions. The first–order reaction kinetics are modeled as a differential equation:

$$\frac{dN_b}{dt} = K_a \left(N - N_b\right) - K_d N_b, \tag{2.7}$$

where N_b are the number of bound ions, and K_a, K_d are the association and dissociation time constants, respectively. The solution of this differential equation is:

$$N_b(t) = \frac{K_a}{K_a + K_d} N \left(1 - \exp\left[-\left(K_a + K_d\right)\left(t - t_0\right)\right]\right). \tag{2.8}$$

This solution is fit to the data in figure 2.6, and the resulting fit is also plotted. The fitting parameters are listed in table 2.5. The first–order reaction kinetic model fits reasonably well to the data from both the systems, except in the beginning of the simulation where the effect of the annealing process is more pronounced; however, we are only interested in the asymptotic behavior of the fit as this is representative of the equilibrium state of the

system. The asymptotic number of bound ions as $t \to \infty$, $A = \frac{K_a}{K_a+K_d}N$ (table 2.5 row 9), is larger in the system simulated with optimized terms. We also report the timescale of ion binding $\tau = \frac{1}{(K_a+K_d)}$ for both systems (table 2.5 row 10). The timescale of binding in the system using optimized cross terms is longer, and suggests that this system would need more time to equilibrate than the system simulated with LB rules. Finally, we report the value of $\frac{K_a}{K_d}$ (table 2.5 row 11), which we observe is much smaller with the new parameter set than compared to that of the system simulated with LB rules.

To examine how specific interactions between ions and lipids are modified by the new parameters, we tracked the binding partners of ions across the box over the last 150 ns of simulation time. Moieties are considered to be bound to an ion if they are within a distance of 3.3 Å from the Na^+ ion. Several electronegative groups in the simulation can potentially bind to the Na^+ ion. We compute the number of these potential binding partners within the first shell of each Na^+ ion across the simulation box. Ions are then sorted according to their box z-positions, and then the data are averaged over the last 150 ns. This is plotted in figure 2.7. We note first that the total number of solvating oxygens of ions within the bilayer headgroup region with the optimized parameter set has dropped by ~ 1 when compared to ions in similar locations in the system simulated using LB rules. This is not surprising, given the dependence of ion coordination preferences on the local environment.[65] The binding to other lipid oxygens has not been altered much by the new parameter set; however, we do note that water within the headgroup region does not appear to be strongly associated with ions.

2.4.4 Water Structure and Dynamics

To further characterize the dehydration of ions in the new simulated system, we look to the lipid– and ion–water interactions. Figure 2.8 shows the number density of water as a function of distance from the bilayer center for each of our simulated systems, with the $2D_C$ and D_B illustrated as dotted lines. We see that our new parameter set produces a bilayer

interface that has more solvent inside the headgroup region, between $10 - 25$ Å from the bilayer center. This density is more similar to that of the system simulated without salt. This suggests that the dehydration of ions in the system simulated with optimized parameters does not correspond to a dehydration of the lipid bilayer.

Next, we characterize the orientational structure of the water. Figure 2.9 examines the water order parameter across the simulation box. We identify perturbed water structure by examining first (P_1) and second (P_2) orientational order parameters for the OW→HW1 bond of water with respect to the z-axis of the simulation box (β). These order parameters are defined using the first and second Legendre polynomials with respect to the angle β,

$$\begin{aligned} P_1 &= \langle \cos(\beta) \rangle \\ P_2 &= \frac{1}{2} \left\langle \left(3\cos^2(\beta) - 2 \right) \right\rangle, \end{aligned} \tag{2.9}$$

where average is over all the waters in a particular volume slice of the box and then over simulation time. We plot these values as a function of distance from the bilayer center. P_1 denotes dipolar ordering of the bond vector and the bilayer normal direction, with a positive value indicating an average outward orientation and a zero value corresponding to an average perpendicular orientation to the bilayer normal or a uniformly random orientation. We observe a similar pattern of ordering across the box in all systems; however, we see an overall reduction in ordering with our new parameter set when compared to both the LB and the no–salt system. We also see the inner minimum of the order parameter moved further into the bilayer when compared to LB, which is consistent with the larger quantity of water in this region that we observe in the water densities.

Following the protocol established in our previous work,[8] we identify three regions within the bilayer interface, B_{-1}, B_{+}, B_{-2}. The B_{-1} region is defined as the region of negative ordering starting at the bilayer center, and ending when the order parameter values cross zero at the start of the B_{+} region. The B_{+} region starts at the end of the B_{-1} region, and is the area of positive ordering, ending where the order parameter crosses zero again. The B_{-2}

region starts at the end of the B_+, and extends out to where the second order parameter goes to zero. This was found by fitting an exponential function to this region and taking the scale parameter from that fit as the boundary with bulk solvent. We find that water is significantly less perturbed by the bilayer with our new parameter set. We have also computed $P_2 \cdot \rho_{\text{Water}}$, shown in shown in figure 2.9(c). This value relates the amount of water in each region of the box and the overall ordering in the region. We still see significantly less ordering with the new parameter set, and even with the larger number of waters in the bilayer headgroup. The integral of this curve is related to the quadrupole splitting $\Delta\nu$ observed in in deuterium NMR experiments.[6,66]

This suggests that while there is more solvent in the interface, it is perhaps not associated with either Na^+or lipids, and may remain less structured than in the system simulated with LB rules. This can be further ascertained by the lateral diffusion coefficients of waters in each of the regions defined by P_2. We compute the mean square displacement (MSD) for water oxygens in each region by first tracking which waters remain in the region. Any waters that leave the region are removed from the MSD calculation. We chose a duration of 100 ps to track the MSD in order to have a sufficiently long time for the MSD to become linear, while still maintaining a statistically significant number of waters in the slice. A line is fit to the middle 80% of the MSD, and the fitted slope is used to calculate the diffusion coefficient following Einstiein's relation for 2D diffusion

$$\lim_{t\to\infty} \frac{\left\langle (r(t) - r(0))^2 \right\rangle}{(t - t_0)} = 4D. \tag{2.10}$$

These values can be seen in table 2.6. We note that the water in the headgroup region, corresponding to B_{-1} and B_+, diffuses slightly faster with the new parameter set, indicating more mobile water in these regions. However, the computed diffusion coefficients are within the error bars that of the system simulated with LB rules. Diffusion in the B_{-2} and $Bulk$

Table 2.6: Diffusion coefficients of water in different regions of the lipid bilayer, defined by the shape of the second orientational order parameter of water molecules in the box. These regions are defined by the shape of the distribution of the second orientational order parameter across the simulation box. B_{-1} is the region of negative ordering starting at the bilayer center, and ending when the order parameter values cross zero. B_{+} starts at the end of the B_{-1}, and is the region of positive ordering ending where the order parameter becomes negative. This starts the B_{-2} of negative ordering, extending out to where the second order parameter goes to zero, where we have $Bulk$ solvent. We see that the optimized parameters result in slightly increased diffusion in the solvent, which correlates with the reduced ordering of the water dipoles and quadrupoles in the system.

	LB ($\times 10^{-10} m^2/s$)	Optimized ($\times 10^{-10} m^2/s$)
B_{-1}	1.11 ± 1.10	1.88 ± 2.41
B_{+}	4.23 ± 1.14	6.11 ± 2.83
B_{-2}	18.11 ± 4.23	21.29 ± 4.12
$Bulk$	27.32 ± 1.15	27.25 ± 1.36

regions are similar in both systems, as these are mostly outside of the bilayer and should not be affected by the new parameter set.

2.4.5 Bilayer Electrostatics

We further characterize the electrostatic properties of our bilayer systems by computing the electrostatic potential across the simulation box. We do this following the protocol used in Saunders *et al.*[8] We first compute the charge density of the system components. We integrate this distribution twice, setting both constants of integration to be zero to enforce a zero value for the electric field in bulk solvent and a zero electrostatic potential at the box edge. This is accomplished by taking the average value of the electric field in the *bulk* region of the box defined earlier, and subtracting this value from all points. Due to the larger system size in the optimized system, we needed to compute the average value of a much larger region than in LB in order to apply boundary conditions. We then integrate again to get the electrostatic potential. This result can be seen in figure 2.10 in supporting information. The shape of the potential is largely unaltered within fluctuations. Systems

simulated with the optimized parameters and with LB rules both have a similar bilayer dipole potential, which remains elevated over the system without salt, by $\sim$ 220 mV. We report that the optimized system has a slightly elevated bilayer dipole potential compared to the system simulated with LB rules, increased by $\sim$ 12 mV. This may be a direct result of the larger number of ions bound to the bilayer in this system. We also note the system simulated with optimized cross terms has different details throughout the electrostatic potential compared to the system simulated with LB rules and in the system without salt, however these are within fluctuations and cannot be used to draw conclusions.

Poisson–Boltzmann (PB) theory is a mean field approximation for solvated ions near an interface. Experimentally PB theory is used to assess the surface potential of the lipid bilayers. We also examine the behavior of the ions in bulk solvent under the framework of PB theory. Following the procedure used in our previous work,[8] we fit the number density of Cl^-ions in the solvent–occupied region of the box to a Poisson-Boltzmann distribution, using the inverse Debye length K and the density of Cl^-at the center of the solvent occupied region of the box ρ_0 as fit parameters. The density is modeled as:

$$\rho(z) = \rho_0 \exp\left(-\bar{z}e\beta\psi(z)\right), \tag{2.11}$$

where ρ_0 is the number density of the ion at the center of the solvent–occupied region of the box, $\bar{z} = 1$ is the valency of the ion in the system, $\beta = \frac{1}{k_b T}$, e is the charge on an electron, and $\psi(z)$ is the electrostatic potential. We then assume the form of $\psi(z)$ to be the sum of two Debye-Huckel potentials[67] reflected across the center of the solvent–occupied region of the box:

$$\begin{aligned} \psi_1(z) &= \psi_s \exp(-K(z + \frac{D}{2})) \\ \psi_2(z) &= \psi_s \exp(K(z + \frac{D}{2})) \\ \psi(z) &= \psi_1 + \psi_2, \end{aligned} \tag{2.12}$$

where D is the distance from the hydration boundary of one bilayer leaflet to the next across the solvent, K is the inverse Debye length, and ψ_s is the surface potential:

$$\psi_s = \frac{\varsigma}{\varepsilon_0 \varepsilon K}. \tag{2.13}$$

The LB system yielded a value of $D = 13.167$ nm and the system simulated with optimized parameters, containing twice as many solvent molecules, gave a value of $D = 27.01$ nm. We take the surface charge density ς from the charge density inside of the hydration boundary of the lipid bilayer. Since only ions contribute a net charge to our system, we compute this using only the charge density of ions in the system. This value was computed to be $\varsigma = 0.13\ e\ \text{nm}^{-2}$ for the system simulated with LB rules, and $\varsigma = 0.11\ e\ \text{nm}^{-2}$ for the system simulated with the new parameters. Our fitting procedure yielded number densities $\rho_0 = 0.043\text{nm}^{-3}$ for the system simulated with LB rules, and $\rho_0 = 0.079\text{nm}^{-3}$ for the system simulated with optimized parameters. The fitted inverse screening lengths were found to be $K = 0.91 \pm 0.014\ \text{nm}^{-1}$ for the LB rules simulation and $0.94 \pm 0.018\ \text{nm}^{-1}$ for the system simulated with optimized parameters. The resulting fit and predicted density of Na^+ions and electrostatic potential can be seen in figure 2.11. We see the results from our simulation represented by points with error bars, while PB theory results are shown in solid lines. We see excellent agreement in the Na^+density profile away from the bilayer surface, and reasonable agreement in the electrostatic potential. From this we can see that the optimized and LB systems both exhibit similar ionic distributions with models used to describe electrophoretic mobility experiments.[67]

2.5 Conclusions

Mixing rules are often relied upon to compute non–bonded cross terms for interacting molecules in molecular simulations. However, when mixing force–fields that have been developed independently of each other, inaccuracies may develop. Here we demonstrate one such case and propose a rigorous solution. MD simulations conducted using predefined

mixing rules for non-polarizable force fields developed separately for ions and lipids have always produced very pronounced salt-induced structural changes in lipid bilayers. Contrary to this, most experimental observations point to a moderate or even an insignificant change in bilayer structure at physiological salt concentrations. We resolve this discrepancy by explicitly parameterizing ion–lipid cross terms using our procedure *"Many Body Non Bonded fix"* (MB-NB-fix). It is based on the NB-fix method employed in previous works [27–35] and utilizes ParOpt software developed in our lab[37].[38] We note that after applying the optimized parameters for Na^+–lipid interactions, the bilayer structure conforms more to experimental observations while all other properties such as solvent structure, electrostatic potential, and dynamic properties are approximately similar to that obtained with those obtained with LB parameters. We note that we have not applied this method to optimize Cl^- interactions terms, which may still further affect the bilayer structure. This will be the subject of future work.

The MB-NB-fix method proposed here is a general method which can be used to derive mixing terms for simulations with independently developed force fields. This method will be used in future work to improve other sets of mixed force-fields, including those of other monovalent ions and the gromos 43A1-S3 lipids, and between these lipids and amino-acids for use in proteins. Furthermore, many body cooperativity effects, such as ion-induced polarization in lipid molecules may be critical to further improving the reproduction of lipid bilayer structure. A correct approach to incorporate these effects to our simulation would be to have explicit polarization terms in our simulation models. This is complicated, as most existing polarizable simulation models are either not very effective at accurately reproducing polarization effects or are much more computationally expensive compared to classical non-polarizable simulations. The MB-NB-fix method has potential to become an ideal solution for mixing force-fields, including polarizable and non-polarizable models in the same system to construct simulations that are tractable yet accurate.

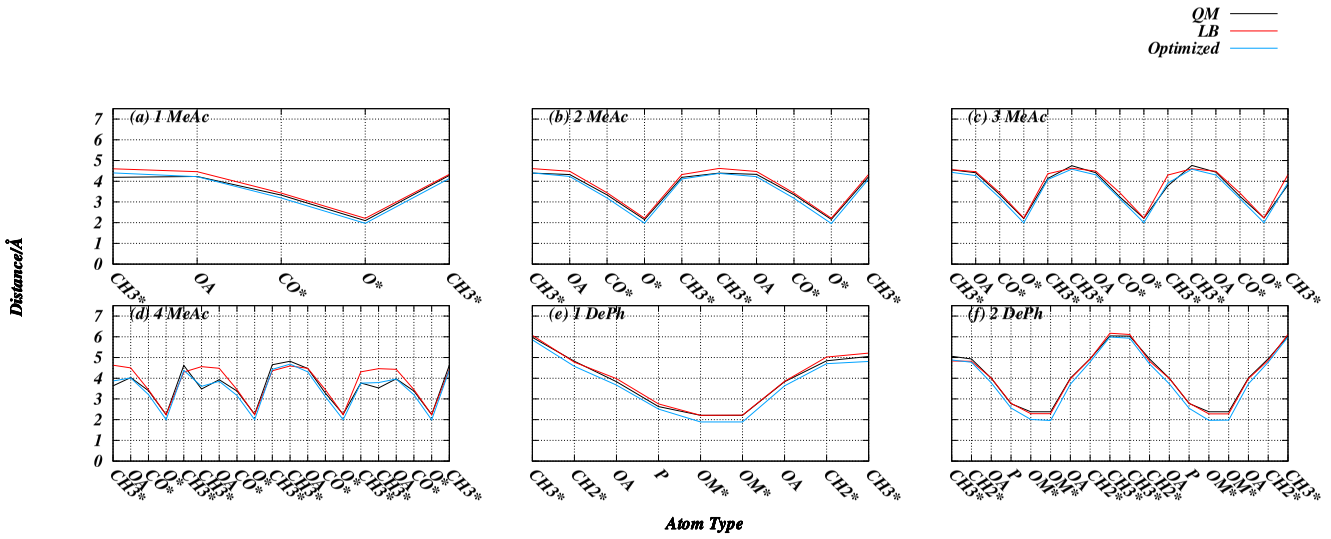

Figure 2.3: Distances from $Na^+$to each component atom in sample clusters. We compute the geometry of our sample clusters by computing the distance from the ion to each other atom in the system, shown per atom type. These distances are used in combination with the substitution energies in figure 2 to compute the error for the NM optimization.

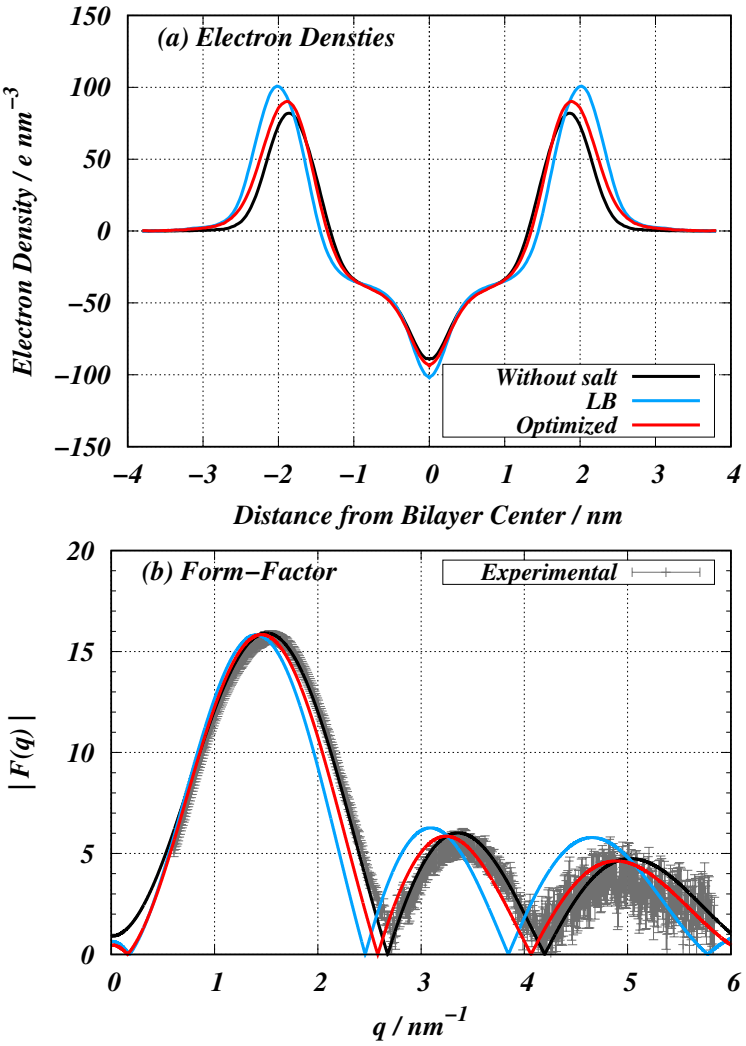

Figure 2.4: Electron densities of the simulated bilayers (a), and corresponding bilayer form–factors (b). Electron densities as obtained using the GROMACS density tool, centered at the minimum to define the bilayer center, and with the electron density of solvent subtracted. The simulated with optimized parameters appears to lack the large peak seen in the system simulated with LB rules, and appears more similar to the bilayer structure of a bilayer simulated without salt. This is further reflected in the bilayer form–factor, computed by taking the cosine–transform of electron density. Experimental SAXS results are for a POPC bilayer in pure solvent.[62] We see the first lobe of the optimized system moves closer to the experimental results and the form–factor of a system without salt. This lines up with experimental results, that have shown small, if any, change in the bilayer SAXS form–factor.[14–16]

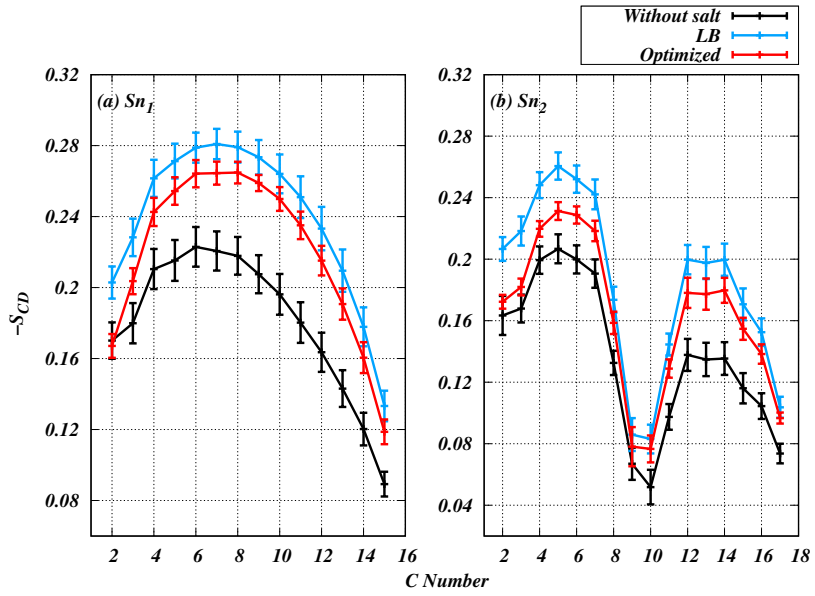

Figure 2.5: Lipid chain deuterium order parameters. S_{CD}s are computed for each carbon for the chains Sn1 (a) and Sn2 (b), starting at the second carbon in the chain. We see that the optmized system is still showing significant ordering in the lipid chains as a result of ion binding; however, the ordering is less pronounced than in the system simulated with LB rules, and is closer to that of the simulation without salt. This result corresponds with the smaller bilayer thickness in the optimized system.

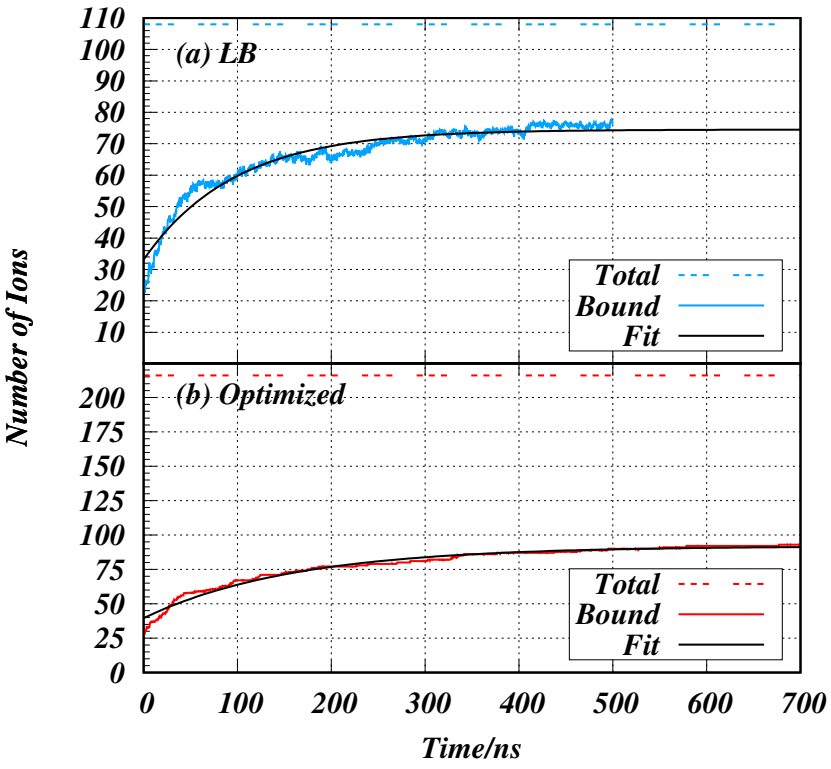

Figure 2.6: Number of ions bound to the lipid bilayer as a function of simulation time. The exponential fits to this data are also shown. These fits are used to compute the asymptotic number of ions bound as well as binding rate constants. 'Total' refers to the total number of ions in each simulation box. A membrane bound ion is defined as having half or fewer of its first coordination shell occupied by water molecules.

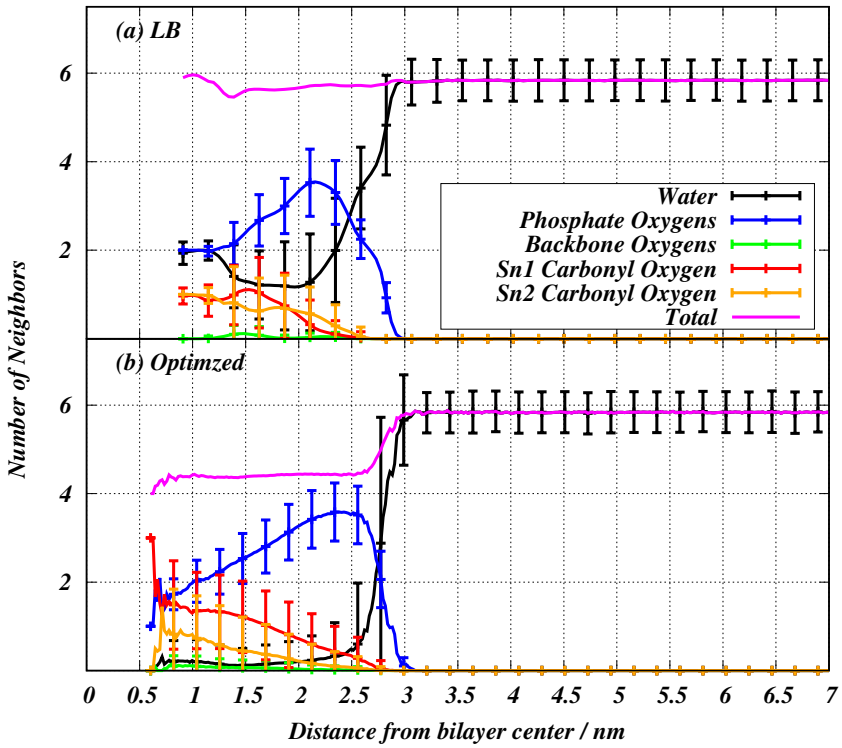

Figure 2.7: Chemistry of Na^+ inner shell coordination as a function of distance from bilayer center. Compared to the system simulated with LB rules (a), the system simulated with optimized cross terms (b) yields a lower Na^+ total coordination number within the headgroup region of the bilayer. This drop in coordination appears to be due to a greater dehydration of the ions in this system.

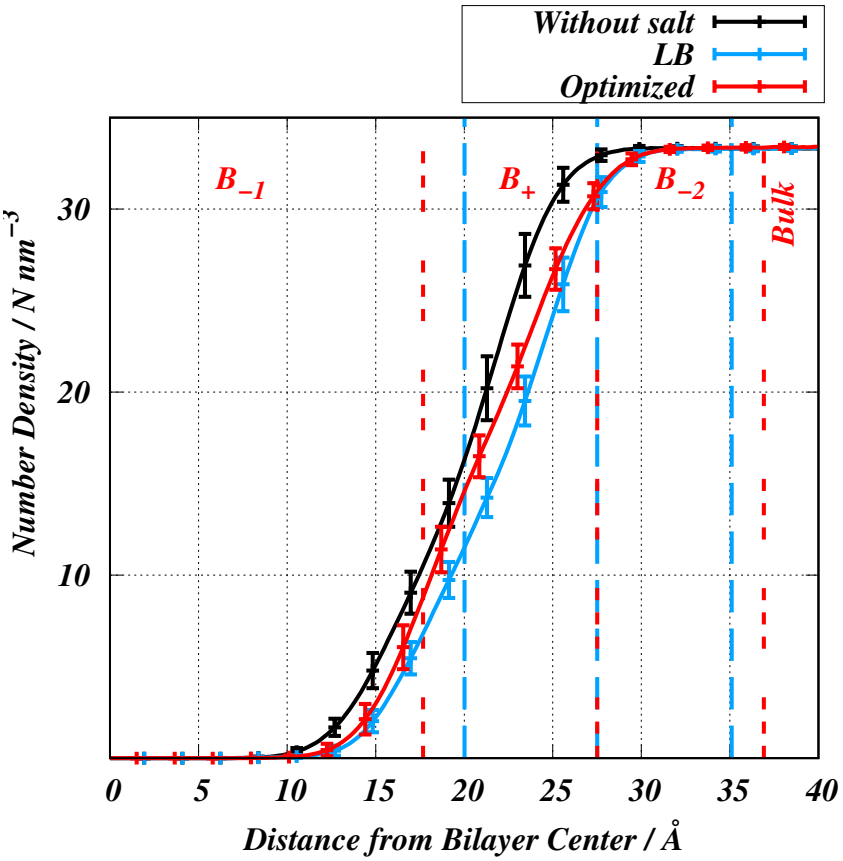

Figure 2.8: Water density at the bilayer interface. We illustrate the regions regions B_{-1}, B_{+}, B_{-2} and $Bulk$ for each system with dotted lines. We see that the optimized cross terms yield a greater density of solvent in the B_{+} and B_{-1} regions over the system simulated with LB rules. We also see the density in these regions of the system optimized with optimized cross terms is more similar to that of the system without salt.

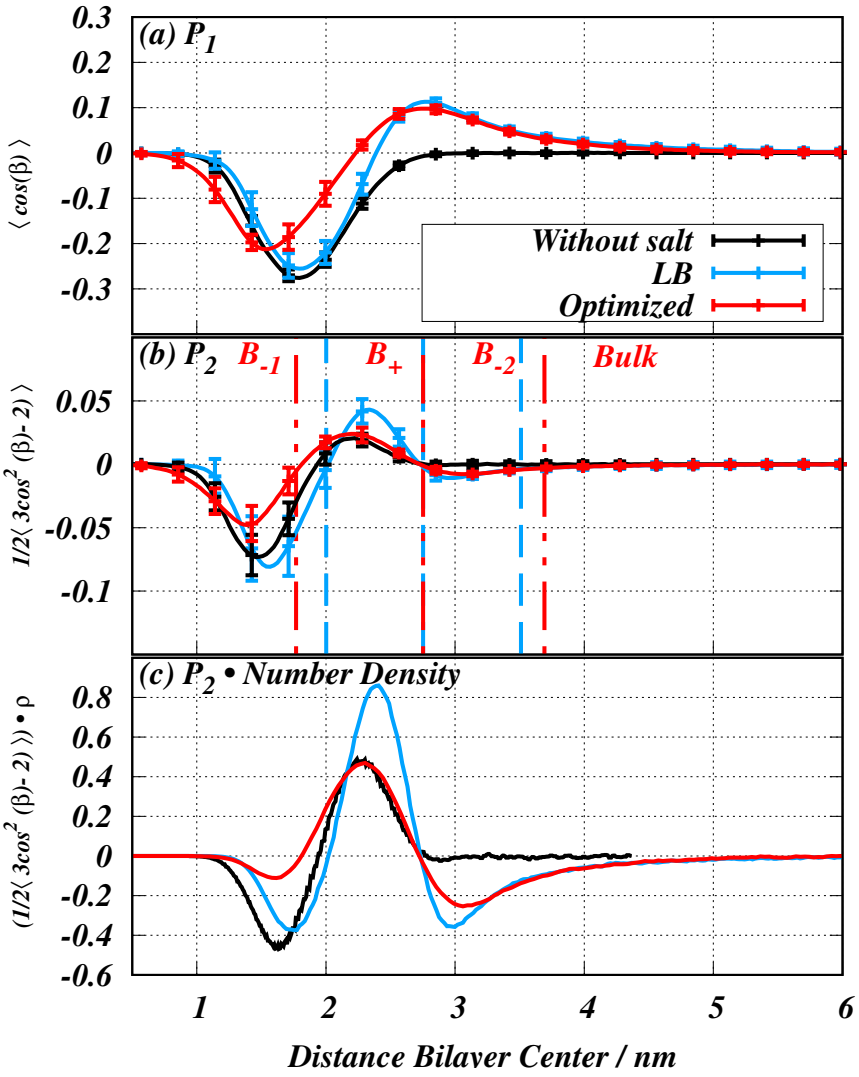

Figure 2.9: Water orientational order parameters P_1 (a) and P_2 (b), and the product of the water number density and P_2 (c). We see in P_1 and P_2 less ordering in the waters in the optimized system, suggesting that waters may be less strongly interacting with ions or lipid components. We denote the four regions of the lipid bilayer based on the shape of the P_2 data as dotted lines in (b).[8] We have not included these regions for the system without salt, as the P_2 data does not include the same details as the systems with salt. The integral of (c) is related to the quadrupolar splitting constant $\Delta\nu$ found in deuterium NMR experiments. This also gives a closer look at how solvent is ordered in the headgroup while accounting for the amount of solvent in the region. We see that optimized cross terms result in a significant drop in the area under the curve, which is much closer to the shape of the data from the system without salt. The regions B_{-2} and $Bulk$ are not within the bilayer headgroup, and are expected to be less affected by the new parameter set.

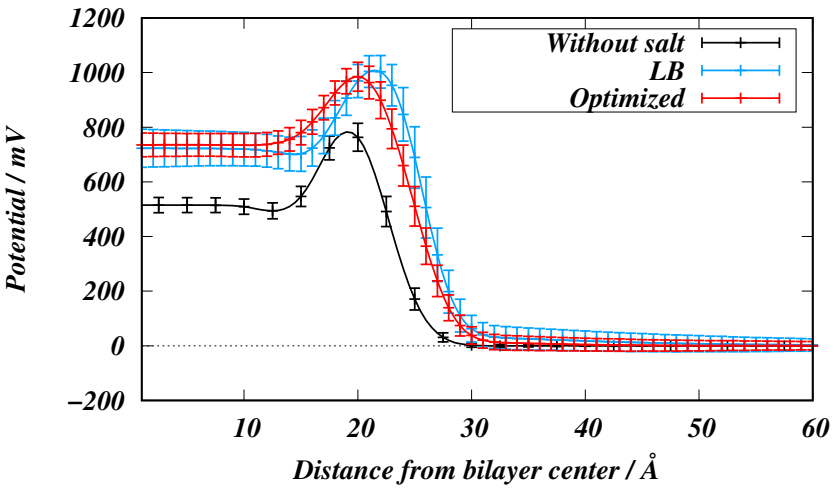

Figure 2.10: Electrostatic potential as a function of distance from bilayer center. The optimized cross terms yield a small change in the location of the peak of the potential in the bilayer simulated with optimized cross terms, as well as the loss of the valley behind the peak.

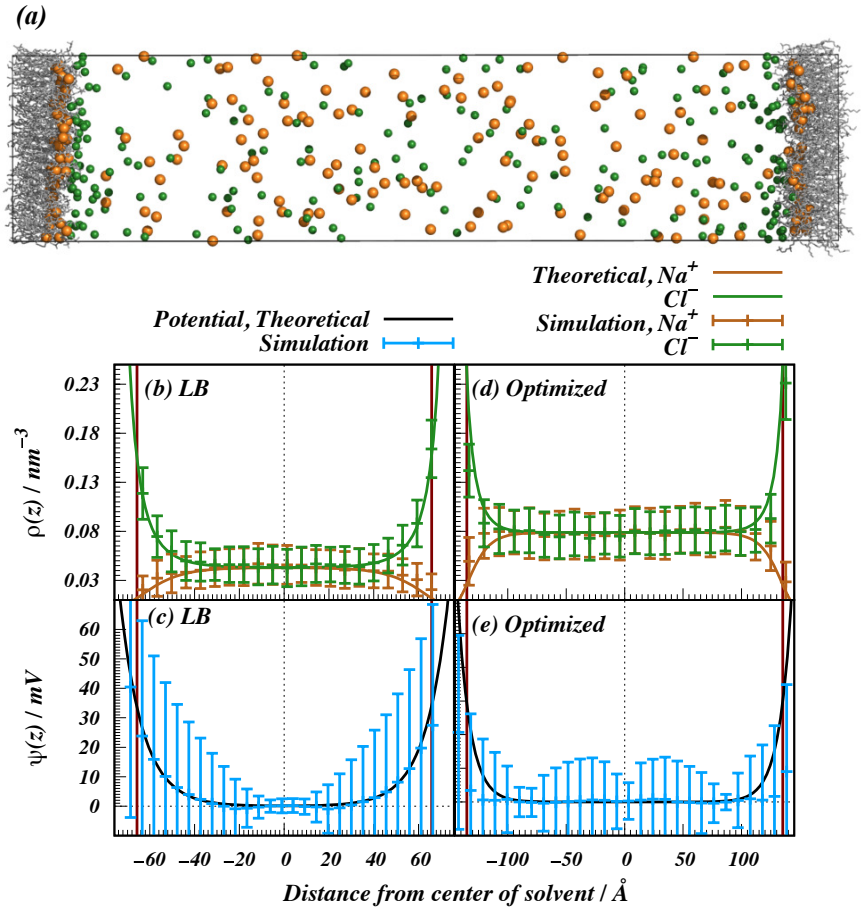

Figure 2.11: Poisson-Boltzmann theory predictions and simulation results. (a) shows a snapshot of the system simulated with optimized cross terms, translated to center the solvent occupied region. Water has been hidden for clarity. (b) and (d) show the number density of ions in the solvent occupied region of the box. (c) and (e) show the corresponding electrostatic potential in solvent. We illustrate theoretical predictions as solid lines, with corresponding simulation results as points with error bars. Red vertical lines denote the *hydration boundary* of the lipid bilayer. Cl^- density data is used for fitting in both systems.

3 Adsorption modes of Na^+, Li^+, and Mg^{2+} to a model zwitterionic lipid bilayer[1]

3.1 Abstract

The adsorption of ions to soft-porous interfaces plays a critical role in many physical and biological processes, such as the function of electrochemical energy storage devices or the attachment of membrane proteins to cells surfaces. In this work we characterize different adsorption modes, and describe the adsorption behavior of Na^+, Li^+, and Mg^{2+} onto a porous substrate. We identify three categories of adsorption based on the degree of dehydration of the ion, viz., steric adsorption corresponding to a lack of dehydration, imperfect adsorption with partial dehydration, and perfect adsorption representing total dehydration. Using 1-palmitoyl-2-oleoyl-sn-glycero-3-phosphatidylcholine (POPC) in salt solution as a generic model system for salt at a soft and porous interface, based on the simulation model used we find that anions, Cl^-, always adsorb sterically. Among cations, the divalent Mg^{2+}does not dehydrate, and is also adsorbed sterically. On the other hand, Na^+adsorbed to a large fraction perfectly and Li^+ exhibits a significant fraction of imperfectly adsorbed ions, We demonstrate that, with everything else held fixed, the adsorption mode of a cation is determined solely by the strength of the electric field produced by the ion at the distance of the hydration shell.

3.2 Introduction

Interactions of ions with soft, porous, and charge-neutral substrates such as zwitterionic lipid bilayers are important and a common system of interest in soft matter physics and biophysics. Empirical studies towards these use simplified models to interpret observations,

[1]Portions reprinted with permission from Matthew Saunders, Abibat Adekeye-Olowofela, and Sabrina Downing, *Adsorption Modes of Na^+, Li^+, and Mg^{2+} to a Model Zwitterionic Lipid Bilayer*, *Langmuir*, American Chemical Society, December 1, 2024.

e.g. assuming the water as a dielectric continuum, or taking the ions as a spherical entity surrounded by a neatly organized hydration shell.[67]

A simple way of defining adsorption of ions to a substrate comes from the Poission-Boltzmann (PB) theory.[67] This mean-field approximation predicts accumulation of ions near a surface due to the mutual electrostatic repulsion of the ions and entropic factors. Deviations in ion distribution from the predictions of PB theory near a substrate are the defining characteristic of the specific adsorption phenomenon .[68,69]

Experimental studies of ion adsorption can be broadly classified into two main groups – methods that examine the electric field/surface potential produced by the adsorbed ions, e.g, electrophoretic mobility[70] or measurement of the forces between bilayers,[71] and methods that can more directly characterize the location and dynamics of ions such as x-ray or neutron scattering,[16,40,61,62,72,73] and NMR.[31,61,74]

At the atomistic level, identifying adsorbed ions poses a different kind of challenge. We have addressed this issue previously, where we characterized adsorption by examining the dehydration of ions near the interface.[6,7,75,76] This is similar to the kind of adsorption described by the Langmuir isotherm model, where it is assumed that ions stick to a soft, porous interface through direct interaction.[77] Adsorption defined thusly has been reported in our previous works for monovalent ions such as $Na^+$and Li^+.[6–8,78] Further, our previous work on divalent ions exhibited that Mg^{2+}maintains its hydration structure regardless of where the ion is located in the lipid bilayer,[7] yet maintaining a distribution distinct from that predicted by PB theory. Hence, in this work we characterize different modes of adsorption corresponding to different ions. Here we categorize the adsorption behavior based on degree of dehydration, starting from no dehydration at all as in the case of $Mg^{2+}$and Cl^-, extending to complete dehydration as in the case with Na^+. In the somewhat different context of RNA, which is not a soft, porous substrate, the specific binding of ions has been addressed extensively [79–83] based on the mobility of cations and further characterized by models that describe the structure of their coordination shell. Cations bound to RNA are frequently

distinguished as being diffuse (similar to our steric adsorbed case), and the site-bound ions are further characterized by outer-shell (again analogous to our steric adsorption ions) or inner shell binding (analogous to the imperfect or perfect adsorbed ions), depending on the folded conformation of the RNA or nearby nucleotides.[79–83]

Along with dehydration, we use specific adsorption in the context of PB density as the defining property of adsorption phenomenon. Based on our previous as well as current atomistic simulations we broadly classify adsorption of ions into three categories – viz. *perfect adsorption*, *imperfect adsorption*, and *steric adsorption*. We also demonstrate that, using different force-field for $Mg^{2+}$the predominant mode of adsorption of $Mg^{2+}$to 1-palmitoyl-2-oleoyl-sn-glycero-3-phosphatidylcholine (POPC) is always *steric adsorption*.

3.3 Methods

We perform multiple simulations of POPC bilayers with LiCl and $MgCl_2$ salt. Configurations for each simulation are listed in table 3.1. Bilayers are constructed of 200 lipids, with 100 lipids per leaflet. Simulations are all performed with 60,000 water molecules to ensure that the simulation box was large enough to have no long-range dipole moment, and have a significant sampling of bulk water. The inclusion of ions substantially increases the region of ordered waters in the system.[7,78] We simulate these systems with a starting concentration of 200 mM salt, in order to ensure that the equilibrium bulk concentration is physiologically

Table 3.1: Simulation system details. Each simulated system is started with 200 mM salt, and the final bulk concentration is computed from the average number density of ions at the center of the solvent occupied region of the box, from the last 150 ns of simulation time. Na^+–Saunders *et al.*simulation trajectories are published in our previous work, and are re-analyzed in this work. The Mg^{2+}–Li *et al.*system is extended to 2.5 μs to ascertain if any exchange of waters from the first shell of Mg^{2+}could be observed. Li^+ (a) parameters are obtained from the work by Joung and Chetatham III.[17] Mg^{2+}(b-c) parameters are obtained from Li *et al.*[84] and Grotz *et al.*,[85] respectively.

System	No. of Cations	No. of Anions	Starting Bulk Salt Concentration	Final Bulk Salt Concentration	Simulated Time
Na^+From Saunders *et al.* 2022[78]	216	216	200mM	103mM	0.7μs
Li^+ (a)	216	216	200mM	102.0mM	1μs
Mg^{2+}(b)	216	432	200mM	152mM	2.5μs
Mg^{2+}(c)	216	432	200mM	153mM	1μs

relevant and yet statistically viable. Systems with $Mg^{2+}$are simulated with twice the number of anions to counter the +2 charge of the cation. All the systems are simulated for 1 μs of simulated time. The Mg^{2+}–Li *et al.*system is extended to 2.5 μs to confirm the long residence time of waters in the first coordination shell of Mg^{2+}.[86] It is observed that ions in the bilayer still do not exchange of waters from their first coordination shell, so another 1 μs simulation is performed using the water-Mg^{2+}interaction model developed by Grotz *et al.*, which significantly increase the water-exchange rate to be closer to the value observed experimentally.[86] All the simulations are performed using the GROMACS molecular dynamics software package, version 5.1.6,[50–54] and analysis is performed using GROMACS built–in analysis tools and in–house software developed on the gromacs API or using the MDanalysis python package.[1,87,88]

3.3.1 Bilayer Construction

Lipid bilayers in solvent are constructed by placing POPC lipids on a 10 x 10 grid, and reflecting to create the second bilayer leaflet. 60,000 solvent molecules are then placed into the box above the bilayer grid, with random solvent molecules replaced to add ions (see table 3.1 for numbers of ions and types in each system). Systems are energy minimized using the steepest-descents algorithm to remove bad-contacts. Following energy-minimization, both systems are allowed to settle in an NPT dynamic run at a temperature of 250K for 1 ns. Systems are then annealed by heating to 350K, and cooling in steps of 10K to the simulation run temperature of 300K in steps of 155 ps. The final annealed configurations for each system are used as the initial configuration for the production molecular dynamics simulations.

3.3.2 Molecular dynamics

For total length of simulation runs, see table 3.1. All systems are simulated with a time step of 4 fs. Neighbor searching is performed every 2 steps. The PME algorithm is used for electrostatic interactions.[59] with a cut-off of 1.6 nm. A reciprocal grid of $56 \times 56 \times 224$

cells is used with 4th order B-spline interpolation. A single cut-off of 1.6 nm is used for Van der Waals interactions. Temperature coupling is imposed with the Nose-Hoover algorithm.[56] Pressure coupling is imposed with the Parrinello-Rahman algorithm.[57]

3.3.3 Force-field parameters

Lipid-lipid and lipid-water interactions are described using our gromos43a1-s3 model,[18] which is calibrated to work with the SPC/E water model.[55] Li^+-water interactions are described using Joung and Cheatham parameters.[17] We use the method described in Saunders *et al.* 2022[78] to compute non-aqueous cross-terms for Li^+ (see table 3.3,and figures 3.1 and 3.2 for details). Describing the interactions of $Mg^{2+}$with water presents several challenges, and there are numerous models developed to describe Mg^{2+}–water interaction.[84,85,89] These

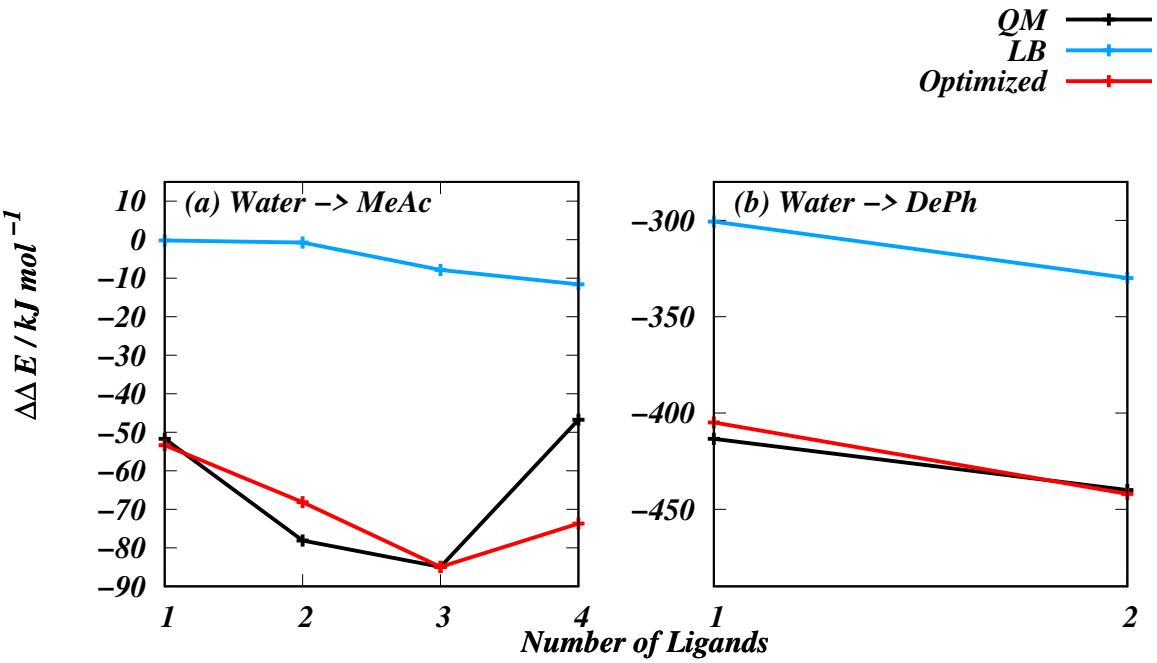

Figure 3.1: Substitution energies of Li^+ from clusters of solvent to clusters of methyl-acetate and diethyl-phosphate. The *ab initio* substitution energies in black were used as the target for the optimization of the non-aqueous ion cross-terms. The blue line is the result of the Lorentz-Berthelot mixing rules, and the red line is the result of our optimized parameters. We see a substantial improvement in the substitution energies for both methyl-acetate clusters and diethyl-phosphate clusters.

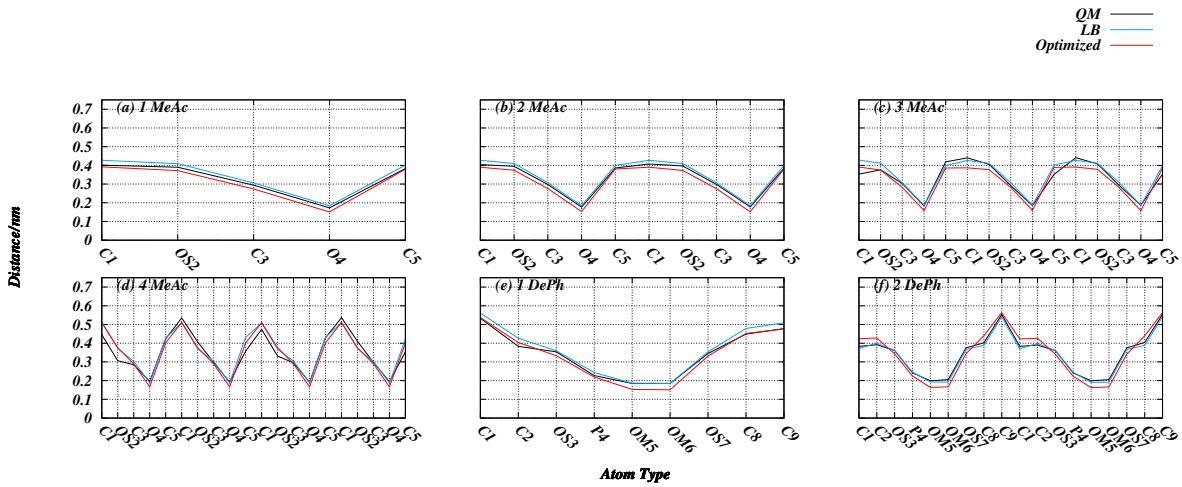

Figure 3.2: Distances of all ligand atoms from ion, for each cluster. Lorentz-Berthelot parameters result in geometries that are very similar to the target data – in general, the optimized parameters result in the ion being slightly closer to the electronegative oxygens in each cluster.

models are optimized to improve the hydration free energies as well as binding energies with various solvent models.[84,85,89] Previous work by our group has examined Mg^{2+}models from Li *et al.* and Allner *et al.*[84,89] in simulations with POPC lipids,[7] and found little variation among them in terms of their effects on lipid bilayer properties. With this in mind, we chose to focus our work here on the parameters developed by Li *et al.* because their optimization procedures closely follow our focus on binding energies. In recent work it has been reported that the existing Mg^{2+}parameters, including those developed by Li *et al.* overestimate the residence time for a water molecule in the first coordination shell of an ion.[85] In our past works using this force-field we reported insignificant Langmuir type adsorption of Mg^{2+}ions to the POPC bilayer, with waters retained in the first coordination shell of the ion.[7] We have also performed simulations with the parameters developed by Grotz *et al.* that directly reduce residence times while not significantly changing other solvation properties of the ion.[85,86] This was done to study how the interactions with water could affect the first-shell coordination of Mg^{2+}in the bilayer interface. We have computed the interaction cross-term

for the Mg^{2+}ion from Grotz *et al.* with SPC/E water explicitly, using the Lorentz-Berthelot mixing rules. Similarly to Li^{+}, we selected LJ cross-terms for use in our simulation following the procedure from Saunders *et al.* 2022.[78] Target QM data for clusters of water with $Mg^{2+}$are shown in table 3.2.

Table 3.2: Mg^{2+} binding energies to water clusters determined using different QM theories and classical force fields. All energies are in kJ/mol. These are used when computing the energies of substitution from water to lipid parts, which we use as our optimization target when selecting LJ cross-terms.

Waters	CCSD(T)/CBS[48]	PBE0+vdW[48]	AMOEBA-HFC[48]	Li et al.[84]	Grotz et al.[85]	Allner *et al.*[89]
1	-344.8	-349.9	-349.8	-276.8	-282.8	-270.3
2	-651.0	-657.6	-657.3	-544.3	-557.3	-531.5
3	-898.7	-904.6	-902.5	-792.1.	-815.2	-774.3
4	-1101.2	-1103.4	-1100.4	-1018.3	-1055.3	-995.7
MAE	-	4.9	4.0	91.1	71.3	106.0

These energies for water were similar enough across force-fields that we chose to use only the values from Li *et al.*[84] for use in computing substitution energies for our target data. The result of our parameter search are shown in table 3.3.

Table 3.3: Lennard-Jones cross-terms used in each Mg^{2+}simulation. We have computed LB-terms using Lorentz-Berthelot (LB) mixing rules, starting with the self-terms for Li^{+} from Joung and Chetatham III*et al.*[17] and the self terms from $Mg^{2+}$from the work of Li *et al.* [84] The MB-NB-fix parameters are chosen following the method described in section **??**. The Grotz *et al.* parameters for Mg^{2+}only change the cross-term for OW-Mg^{2+}, and were computed using LB-rules to mix the self-terms from Grotz *et al.*[85] with those of SPC/E water, without changing the cross-terms with anything else in the system. ϵ are in units of / Kj/mol and σ are presented in units of /nm.

Atom type	Li^{+}				Mg^{2+}					
	LB-Rules		MB-NB-fix		LB-Rules		MB-NB-fix		Grotz *et al.*	
	ϵ	σ	ϵ	σ	ϵ	σ	ϵ	σ	ϵ	σ
CH3	1.07485	0.25797	0.99872	0.30898	0.19239	0.30856	0.68709	0.14257	0.68709	0.14257
CH2	0.75411	0.27432	1.05729	0.20001	0.13238	0.32468	0.63126	0.20617	0.63126	0.20617
OA	1.09408	0.21821	2.91925	0.20020	0.19044	0.26890	5.05190	0.26223	5.05190	0.26223
P	1.85667	0.23975	6.99324	0.21844	0.32318	0.29044	3.89200	0.27811	3.89200	0.27811
OM*	1.19328	0.21400	0.23749	0.20015	0.20771	0.26469	3.22262	0.17691	3.22262	0.17691
CO*	0.35344	0.29727	0.48204	0.35920	0.06152	0.34796	0.56152	0.37127	0.56152	0.37127
O*	1.19328	0.21400	0.06248	0.20068	0.20771	0.26469	2.43058	0.13069	2.43058	0.13069
OW	0.95709	0.22875	0.95709	0.22875	0.16659	0.27944	0.16659	0.27944	13.75000	0.21010

3.4 Results and Discussion

3.4.1 Bilayer simulations of Li^+ and Mg^{2+}

Lipid bilayer structure

The distribution of electron dense and heavy atoms is often studied by using scattering techniques, like small-angle x-ray and neutron scattering. These methods yield a scattering form-factor. Densities can be obtained from the form-factor by solving the inverse problem, which is a technically hard problem. In experiments this is usually solved by fitting a model to the form-factor. Simulations give us direct access to atomic positions, and consequently the densities. This allows us to compute a scattering form-factor by taking a cosine transform of the density. The computed form-factor can be compared with the direct measurements of the experiment. The simulated lipid bilayer x-ray scattering form-factors and associated electron densities for each system are shown in figure 3.3. We compare all form-factors for

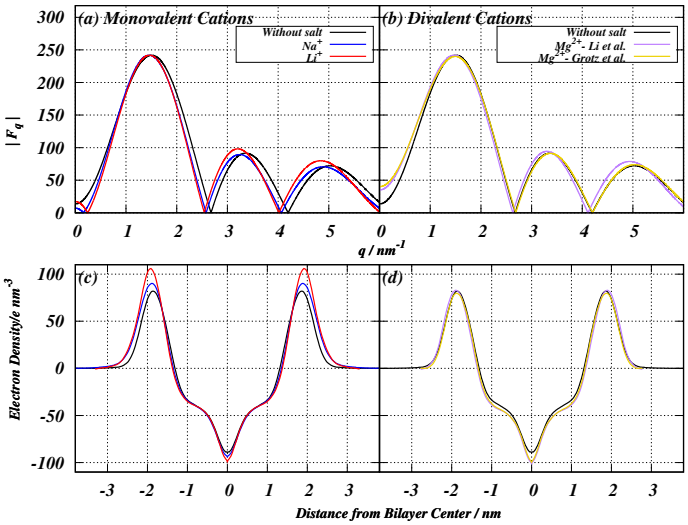

Figure 3.3: Comparison of x-ray scattering formfactors (a,b) and associated electron densities (c,d) for simulated systems. The system with Li^+ salt has a slightly thicker bilayer compared to $Na^+$and the simulation without salt (a,c) and, Mg^{2+}does not significantly change the bilayer thickness under any parameter set studied (b,d).

each system to that of a system simulated without salt, published in our previous work.[6] The bilayer thickness D_{hh} is determined by measuring the distance between the peaks in the

electron density, which roughly localize the electron-dense phosphates in the lipid headgroup – the values for this can be seen in table 3.4.

Experiments often report various types of thicknesses, volumes, and cross-sectional areas that are model dependent. We also compute these quantities to compare the simulation results with experiments. These values are presented in table 3.4. Based on the D_{hh} and the $2D_C$ there is a slight thickening of the bilayer in the Li^+ simulation above that seen in the Na^+simulation. The Mg^{2+}simulations , irrespective of the parameter set, yield much less thickening than the Li^+ simulation. The volumes per lipid (V_L), headgroup (V_H), and chains (V_C) are computed using the method of Petrache *et al.*[60] This is done by optimizing the function:

$$\Omega(v_i) = \sum_{z_j}^{\rho_s}(1 - \sum_{i=1}^{N_{\text{Groups}}} (\rho_i(z_j)v_i)^2), \tag{3.1}$$

Table 3.4: Bilayer simulation details, and structural parameters. Here we detail the various structural measurements of each simulated bilayer. D_{hh} is the distance measured between the peaks in the electron density, which localize the electron-dense phosphate moiety in the lipid headgroup. D_B is a distance between the Gibb's surfaces[62] on the probability density of solvent as it approaches the lipid bilayer. $2D_C$ is the distance between the Gibb's surfaces on the probability density of lipid chains, and represents the lipid chain thickness. Volume per lipid V_L is measured by dividing the volume of the entire system into solvent and ions, and lipid following the method by Petrache *et al.*[60]. This V_L is the sum of the V_H and V_C, which are the volume per lipid headgroup and volume per lipid chains respectively. Area per lipid molecule A_L is computed as the ratio of twice the lipid chain volume V_C with $2D_C$. We also report the position of the hydration boundary of each system, which we compute as the point where the second water order parameter $P_2(cos(\beta)) \approx 0$ as was done in Saunders *et al.* 2019[8].

	No Salt	Na^+	Li^+	Mg^{2+}–Li *et al.*	Mg^{2+}–Grotz *et al.*
D_{hh}(nm)	3.744 ± 0.107	3.764 ± 0.088	3.864 ± 0.070	3.832 ± 0.364	3.768 ± 0.525
D_B(nm)	3.654 ± 0.047	3.936 ± 0.043	4.511 ± 0.048	4.325 ± 0.044	4.213 ± 0.049
$2D_C$(nm)	2.707 ± 0.034	2.897 ± 0.034	3.015 ± 0.034	2.880 ± 0.029	2.809 ± 0.032
V_L($\times 10^{-3}$nm^3)	1215.57 ± 1.0	1211.32 ± 1.21	1201.2 ± 1.05	1219.8 ± 1.24	1227.7 ± 1.24
V_H($\times 10^{-3}$nm^3)	310.68 ± 1.14	314.81 ± 0.75	306.0 ± 1.01	324.0 ± 1.26	327.9 ± 1.10
V_C($\times 10^{-3}$nm^3)	904.89 ± 1.28	896.50 ± 1.19	895.3 ± 0.91	895.8 ± 1.05	899.8 ± 1.06
A_L($\times 10^{-2}$nm^2)	66.86 ± 0.85	61.89 ± 0.73	59.39 ± 0.69	62.21 ± 0.63	64.35 ± 0.82
Hydration Boundary (nm)	2.79	3.69	3.63	3.48	3.33

where $\rho_i(z_j)$ is the number density of the i component in the z_j slice of the box and v_i is the corresponding partial component volume. N_{Groups} is the number of atom groups for which we are dividing the system volume into component volumes – we have groups for solvent plus ions, lipid chain without the terminal methyls (CH_*), terminal methyls (CH_3), and the lipid headgroups (H). The lipid volumes are then computed as

$$\mathrm{V_C} = N_{\mathrm{CH_*}} \times v_{\mathrm{CH_*}} + N_{\mathrm{CH_3}} \times v_{\mathrm{CH_3}} \tag{3.2}$$

and

$$\mathrm{V_H} = N_H \times v_{\text{headgroup}}, \tag{3.3}$$

where $N_{\mathrm{CH_*}} = 30$, $N_{\mathrm{CH_3}} = 2$, $N_{\mathrm{H}} = 20$ are the number of united atoms per atom group for CH_*, CH_3, and H. The chain volume $\mathrm{V_C}$ is similar for all systems studied, and there is some variation in the headgroup volume $\mathrm{V_H}$. However, this method of dividing up the volume is more prone to errors in the headgroup region due to significant overlap between the headgroup and solvent densities. Thus, we also see similar variation in the total lipid volume $\mathrm{V_L}$. The two-dimensional area per lipid $\mathrm{A_L}$ is defined as $\frac{2V_c}{2D_c}$ as is often reported from SAXS and SANS experiments,[61] and is an important measure of how the lipids condense as the bilayer thickens. Both the simulations with Mg^{2+}yield bilayers with a larger $\mathrm{A_L}$ than the monovalent ions studied in this work, and are closer in area to the simulation without salt.

The detailed structure of molecules and their neighborhoods are often studied using various nuclear magnetic resonance (NMR) techniques. At present, these experiments with various salts are sparse. Thus, we report these data with anticipation that future experiments will fill this gap and validate or invalidate these numbers. Lipid chain ordering is determined via the acyl chain S_{CD} per carbon atom. These can be seen in figure 3.4.

There is significant increase in chain ordering in the systems with $Na^+$and Li^+, which is consistent with the slight thickening of the bilayer seen in the $\mathrm{D_B}$ values. The less coordinated Mg^{2+}systems have remained much closer to the ordering seen in the no-salt simulation.

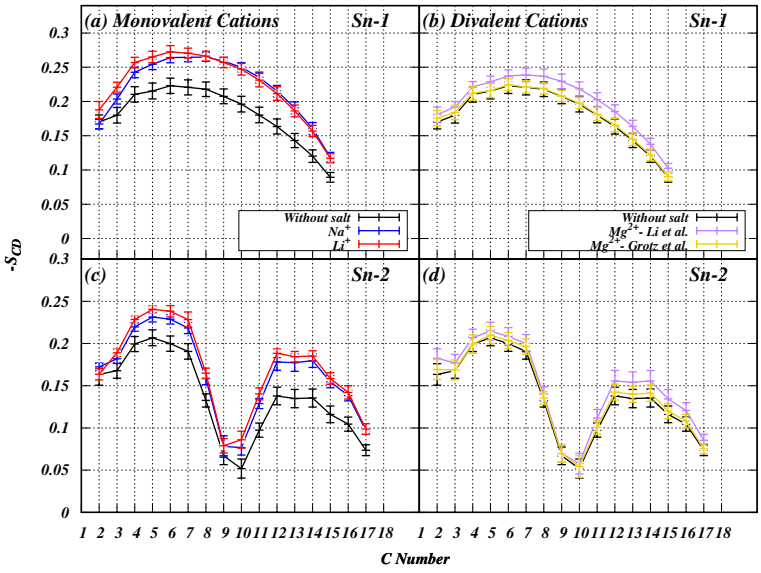

Figure 3.4: Acyl chain carbon-deuterium order parameters. These are computed for the Sn1 and Sn2 chains of each lipid starting at the second carbon in the chain.[63,64] We note that the lipids simulated in systems of monovalent ions (a,c) show a significant increase in the lipid chain ordering for both acyl chains. The systems simulated with Mg^{2+}(b,d) are much closer in ordering to that of a system simulated without ions.

3.5 Specific ion adsorption

3.5.1 Bulk ions

Interfaces in salt solutions give rise to a double layer of cations and anions at the surface.[67] Ions in these double layers get stuck to the surface, or adsorb, which is sometimes referred to as specific binding. Zwitterionic lipid bilayers have no net charge before ions are adsorbed, so this adsorption determines the surface charge density on the substrate. This charge is measured experimentally using the electrophoretic mobility of the vesicle. Interpretation of such experiments requires one to define a surface, often called the "slip-surface" where solvent beyond that point can be represented by a dielectric continuum. The electrostatic potential at this surface is the ζ–potential. In simulations the interface is not a simple surface, but a region without a clear point of delineation.

Hydration boundary

We identify this slip-surface boundary as the point where water orientational ordering is negligible, i.e. beyond the "slip-surface" boundary water quadrupoles are sufficiently isotropic, giving dielectric properties of water similar to that of bulk solvent. We compute this by first dividing the box into slices along the direction normal to the bilayer. For each water within a slice we compute the average value of first and second order legendre polynomial of the cosine of the angle between the box z-axis and the water O-H bond vector, and then average these values over the last 150 ns of simulated time. Figure 3.5 shows the water order parameters as a function of the distance of a slice from the bilayer center.

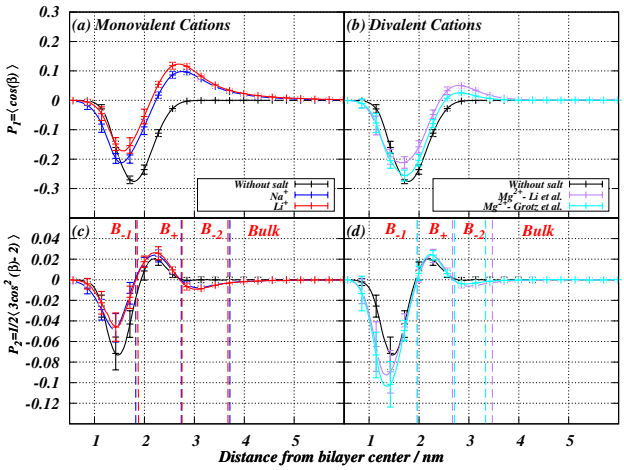

Figure 3.5: Water order parameters. The P1 and P2 calculated for monovalent cations (a,c) show greater organization in the bulk region and the B_{-2} regions, and less organization within the lipid-occupied regions of the system (B_{+} and B_{-1}) compared to the simulation without salt. On the other hand, with the presence of Mg^{2+}salts we observe an overall less pronounced effect in the bulk and B_{-2} regions compared to the system without salt (b,d).

The first order parameter describes the in-out ordering of the bond vector with respect to the box z-axis – a vector parallel to the axis and pointing normal to the bilayer would have a positive ordering, and a vector pointing into the bilayer would have a negative ordering. We see that waters at the surface of each bilayer have a significant outward orientation at the bilayer surface, and that reverses as we move closer to the bilayer center. When compared to

the system simulated without ions, we see that the monovalent ions perturb the water in-out orientation more than Mg^{2+}, especially in the case of the Mg^{2+}–Grotz *et al.*parameters.

The second order parameter roughly describes the organization of the quadrupole moments of water, and the value of this parameter can be used to compute the quadrupolar splitting values determined in deuterated water NMR experiments.[66,90] The vertical dotted lines in figure 3.5 denote regions of interest in the bilayer based on the sign of the second order parameter. We call the innermost region of negative ordering B_{-1}, which ends when the values become positive. This next region of positive ordering is called B_{+}, and the following region of negative ordering is B_{-2}. Each bilayer system with ions has these regions, but they are at differing distances from the bilayer center. It should be noted that beyond the B_{-2} region the ordering does not abruptly reach zero in the systems simulated with salt.

Figure 3.5 shows monovalent ions have less organization in the B_{-1} region (inside the lipid headgroup) when compared to that of the divalent ions, whereas in regions B_{+} and B_{-2} (closer to the bilayer surface) the divalent ions show significantly less organization compared to that of monovalent salts. The hydration boundary is determined by fitting an exponential decay to the second water order parameter starting at the minimum of the B_{-2} of the histogram. The decay length is used to demarcate the point where the ordering becomes zero – water beyond this region is regarded as bulk solvent. The location of the hydration boundary is noted in figure 3.5, and the distance to this point from the bilayer center is listed in table 3.4.

Poission-Boltzmann Theory

With the boundary defined, we look to the region of bulk solvent to examine the behavior of ions and ascertain that they follow the predictions of PB-theory.[67] The purpose of this endeavor is to distinguish the ions in bulk solvent from those that are adsorbed, as the density of the adsorbed ions are expected to deviate from PB-theory predictions. We must first compute all the model parameters for the number density and electrostatic potential

predicted by PB-theory, and compare our simulation results to this prediction. The PB-theory assumes that the number density of ions follow a Boltzmann distribution:

$$\rho(z) = \rho_0 \exp\left(-\bar{z}e\beta\psi(z)\right), \tag{3.4}$$

where ρ_0 is the ion density in the center of the dielectric continuum, $\bar{z}$ is the valency of the ion, $\beta = (k_b T)^{-1}$, e is the charge on an electron, and $\psi(z)$ is the electrostatic potential. The surface is defined by the hydration boundary of each system. The lengths of the solvent occupied regions, D, in each system is found by measuring the distance across the solvent from the hydration boundary of one leaflet of the bilayer to the other. These values are listed in table 3.5. This places the surfaces at $z = \pm D/2$ nm, where $z = 0$ is the center of the

Table 3.5: Poisson-boltzmann theory parameters. These parameters are computed for each simulated system studied (excepting the bulk density ($\rho_{0,i}$), which we fit to our simulation results). These are then used to compute the number density distribution and the electrostatic potential as described by Poisson-Boltzmann theory to compare to our simulation results. $\sigma$is the surface charge density of the bilayer, D is the length of the bulk-solvent occupied region of the box, K is the Debye screening length, and $\rho_{0,i}$ is the number density of the particular ion at the center of bulk solvent.

Parameter	Na^+	Li^+	Mg^{2+}–Li *et al.*	Mg^{2+}–Grotz *et al.*
$\sigma(e/nm^2)$	0.161	0.182	0.0690	0.0476
D (nm)	26.927	26.557	26.658	25.226
K (nm^{-1})	3.331	3.333	3.913	3.921
$\rho_{0,cation}$ (nm^{-3})	0.059	0.060	0.091	0.092
$\rho_{0,anion}$ (nm^{-3})	0.062	0.063	0.183	0.185

solvent-occupied region of the simulation box. The electrostatic potential $\psi(z)$ is modeled as a sum between two Debye-Huckle potentials:[67]

$$\psi_1(z) = \psi_s \exp\left(-K(z + \frac{D}{2})\right) \tag{3.5}$$

$$\psi_2(z) = \psi_s \exp\left(K(z - \frac{D}{2})\right) \tag{3.6}$$

$$\psi(z) = \psi_1(z) + \psi_2(z) - \big(\psi_1(0) + \psi_2(0)\big), \tag{3.7}$$

where $\psi_s = \frac{\sigma}{\epsilon_0 \epsilon} K$ is the electrostatic potential at the bilayer surface as defined by the hydration boundary, ϵ is the dielectric constant of SPC/E water $\epsilon = 70.7$,[91] and σ is the surface charge density of the bilayer leaflet.[67]

σ is determined for each system by integrating the charge density of all species within the hydration boundary on either side of the bilayer. This charge divided by the box area is the surface charge density. These values can be seen in table 3.5. Since our phospholipid is zwitterionic, all of the surface charge comes from the ions that have accumulated within the hydration boundary (see figure 3.6)

Returning to equation 3.7, K is the inverse Debye length,

$$K = \sqrt{\sum_i \rho_{0,i} \bar{z}_i^2 \frac{e^2}{\epsilon_0 \epsilon k_b T}}, \tag{3.8}$$

where $\rho_{0,i}$ is the density of each ion in a given system at the center of bulk solvent. This is taken as an average of the number density of each ion in the solvent occupied region of the box.

Finally, we fit equation 3.4 to the density of anions in bulk solvent via ρ_0. The comparisons can be seen in figure 3.7. Past the hydration boundary of the lipid bilayer, it can be seen that the density of anions continues to climb monotonically. Additionally, the density of cations drops monotonically to a trough value before climbing closer to the bilayer center, near the phosphate groups (see figure 3.6 and 3.7).

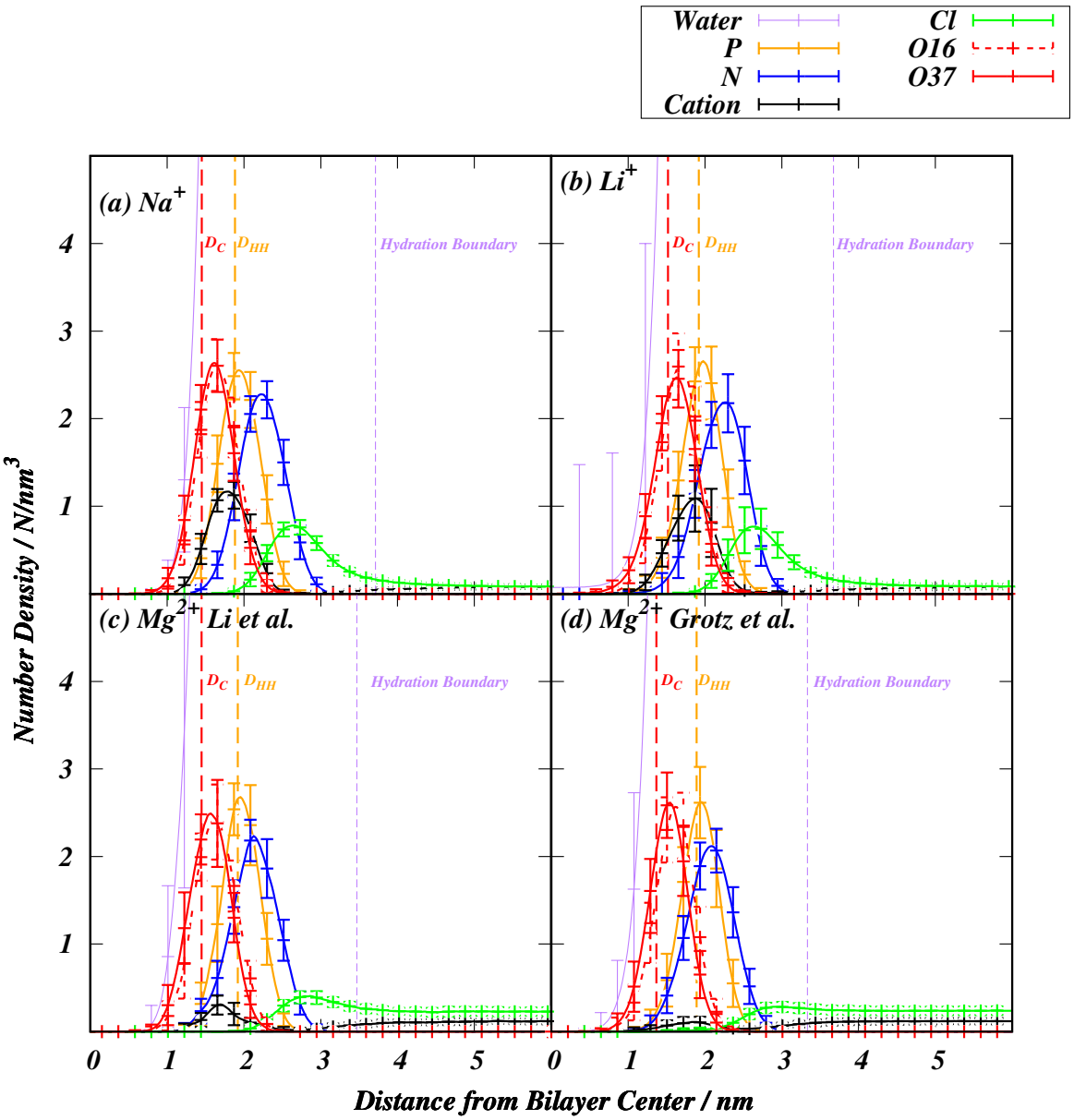

Figure 3.6: Number density of lipid headgroup species and ions near the bilayer interface. (a-b) We report that the monovalent cations show peaks near the phosphate, with accumulation of an anion peak that resembles the double layer. (c-d) Mg^{2+}does not show significant accumulation in the lipid bilayer headgroup compared to the monovalent ions, with a similarly small anion peak. However, in all systems studied, ions are accumulated near the phosphorus. Integrating the number density of cations within the hydration boundary, denoted by the purple vertical dashed line, gives the number of ions that are sterically bound. The orange vertical dashed line delineates the D_{hh} and the red vertical dashes delineate the D_C of the bilayer.

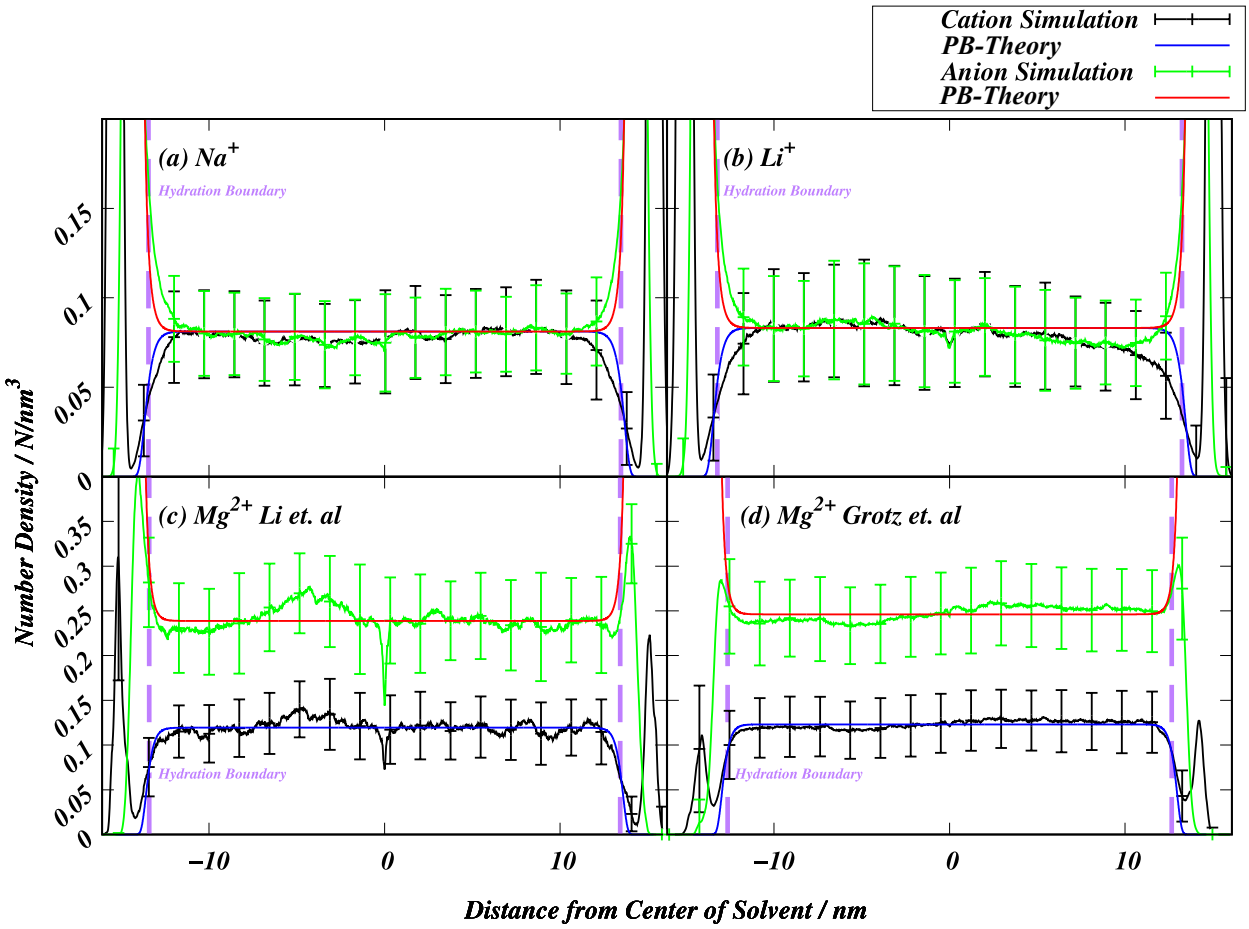

Figure 3.7: Number density of cations and anions in the bulk solvent-occupied region of each simulated system, compared with theoretical predictions from PB-theory for each calculated σ. PB-theory predictions correspond well with the simulation results within the region bounded by the hydration boundary.

We also compare the electrostatic potential from our simulations to the potential from PB-theory (figure 3.8). The electrostatic potential for each simulated system can be computed by twice integrating the Poisson equation

$$\phi(z) = -\frac{1}{\epsilon_0}\int_0^z \int_0^{z'} \rho(z) dz dz' + C_1 z + C_2. \tag{3.9}$$

We set the boundary conditions that the electric field in bulk solvent must be zero, and the electrostatic potential at the box edge must be zero. The electrostatic potential from simulation agrees well with the prediction from PB-theory.

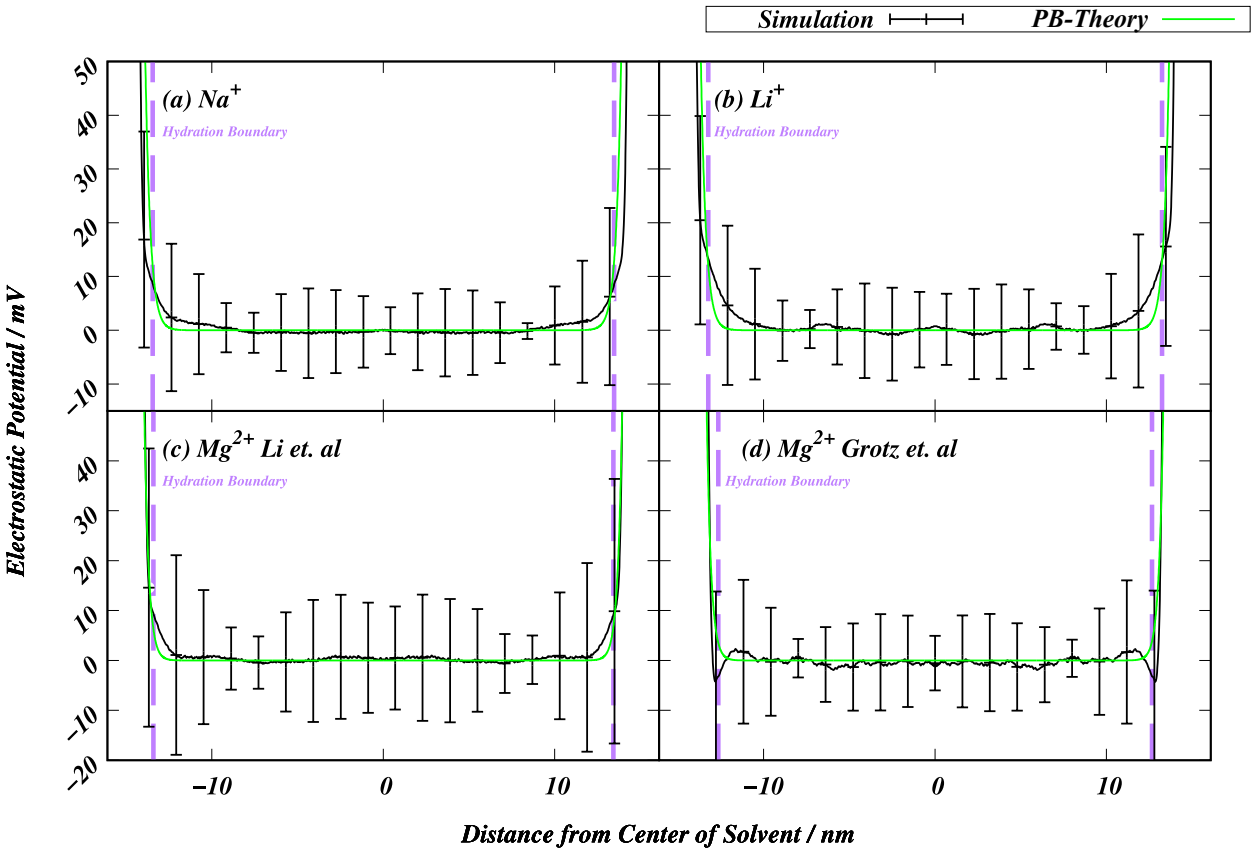

Figure 3.8: Electrostatic potential in the bulk solvent-occupied region compared to predictions from PB-theory. We report good agreement between the theoretical potential shown in green, and the simulation results shown in black, within the region bounded by the hydration bounds of the lipid bilayer.

3.5.2 Adsorbed ions

The total number of adsorbed ions are counted as the number of ions within the "slip-surface" or "hydration-boundary" of the bilayer, and further characterization is based on the level of hydration of the ion. Binding constants from the Langmuir Isotherm model are often computed in experiments to describe ion binding affinity for surfaces; however, this model requires a fixed number of binding sites per lipid. The actual number of binding sites per lipid is not known. Therefore, we report the number of ions adsorbed per lipid (θ), which is related to the binding affinity of each ion for the lipid bilayer. We observe 0.51 Na^+per lipid bound, 0.57 Li^+ per lipid, 0.13 Mg^{2+}per lipid in the Mg^{2+}–Li *et al.*system, and 0.10 Mg^{2+}per lipid in the Mg^{2+}–Grotz *et al.*system. We see a substantially larger number of $Na^+$and Li^+

adsorbed per lipid than Mg^{2+}, which may be reflective of the amount of space occupied by each ion, and seems to follow the binding modes such that the more dehydrated ions correlate with a larger number of ions adsorbed per lipid. The fraction of cations adsorbed in each mode of adsorption can be seen in table 3.6, and the fractions of Cl^-anions adsorbed can be seen in table 3.7. Cl^-adsorption fractions follow a similar trend to that of the total number of cations bound, but adsorption is almost entirely in the steric modality.

Adsorption modalities

Further characterization of the adsorbed ions begins by examining the first-shell coordination partners of cations in each system. This can be counted by first determining a cutoff value for the first hydration shell of each ion – the values for this cutoff are 3.2 Å for Na^+, 2.7 Å for Li^+, 3.3 Å for Mg^{2+}, and 3.0 Å for Cl^-. These values are determined from radial distribution functions for water oxygen (or water hydrogen in the case of Cl^-) around

Table 3.6: Fractions per lipid of cations perfectly adsorbed, imperfectly adsorbed, sterically adsorbed, and non-adsorbed cations averaged over the last 150 ns of simulation time. These are computed by counting the number of waters in the first-coordination shell of every ion in the simulation box in every frame. For the total number of adsorbed ions, we only check if the ion is within the hydration boundary of the bilayer. We then subtract the number within this region that are completely dehydrated – these are the perfectly adsorbed ions. We further subtract any ions that have lost one or more waters – the imperfectly adsorbed ions. The remaining are considered sterically adsorbed. We also report the total number of bound ions per lipid as a measure of the affinity of the ion to the lipid bilayer – the number of Mg^{2+}ions per lipid is fall smaller than that for the more perfectly adsorbed ions Li^+ and Na^+.

Adsorbed cations / lipid	Na^+	Li^+	Mg^{2+}–Li *et al.*	Mg^{2+}–Grotz *et al.*
Total θ	0.472	0.575	0.129	0.091
Steric θ_s	0.010	0.015	0.116	0.071
Imperfect θ_I	0.068	0.165	0.008	0.020
Perfect θ_P	0.394	0.395	0.005	0.000

Table 3.7: Fractions per lipid of anions perfectly adsorbed, imperfectly adsorbed, sterically adsorbed, and non-adsorbed anions in each simulation, defined in the same way as we define adsorption of cations. These are computed by counting the number of waters in the first-coordination shell of every anion in the simulation box in every frame. For the total number of adsorbed anions, we only check if the anion is within the hydration boundary of the bilayer. We then subtract the number within this region that are completely dehydrated – these are the perfectly adsorbed anions. We futher subtract any ions that have lost one or more waters – the imperfectly adsorbed ions. The remaining are considered sterically adsorbed. We indicate each system by the cation name, as the anion in the system is always Cl^-. We note that the anion binding fractions follow the trend seen in the total number of cations bound for each system, due to the formation of the ionic double-layer at the bilayer-water interface. Most anions adsorb sterically in each system, with some adsorbing imperfectly as they approach the positively charged choline trimethylammonium in the lipid headgroup.

Adsorbed anions / lipid	Cl^-in Na^+System	Cl^-in Li^+ System	Cl^-in Mg^{2+}–Li *et al.*System	Cl^-in Mg^{2+}–Grotz *et al.*System
Total θ	0.423	0.463	0.186	0.208
Steric θ_s	0.209	0.213	0.107	0.126
Imperfect θ_I	0.214	0.250	0.079	0.082
Perfect θ_P	0.000	0.000	0.0	0.0

each. This cutoff is used to produce a neighborlist for ions across each simulation in every frame, and count the number of neighbors within this cutoff. These data are histogrammed and averaged over the last 150ns of simulation time. The results for this are presented in figure 3.9.

The number of perfectly adsorbed ions is determined by counting the number of ions without any remaining waters in their first coordination shell. It is observed that in the Na^+system, a majority of the ions adsorbed to the bilayer are completely dehydrated. The Li^+ system has a similar fraction of perfectly adsorbed ions compared to Na^+, and practically no perfectly adsorbed ions are seen in any of the Mg^{2+}simulations. Cl^-anions are not seen adsorbed perfectly in any simulation.

Similarly to the perfect adsorption case, imperfectly adsorbed ions are counted as ions with one or more waters in their first coordination shell, but missing at least one water from the shell. We use the number of coordinating waters of an ion in the bulk solvent region of our simulation as the maximum coordination number for the ion (Figure 7). This gives a coordination number of 4 for Li^+ and 6 for Mg^{2+}. We calculate the number of

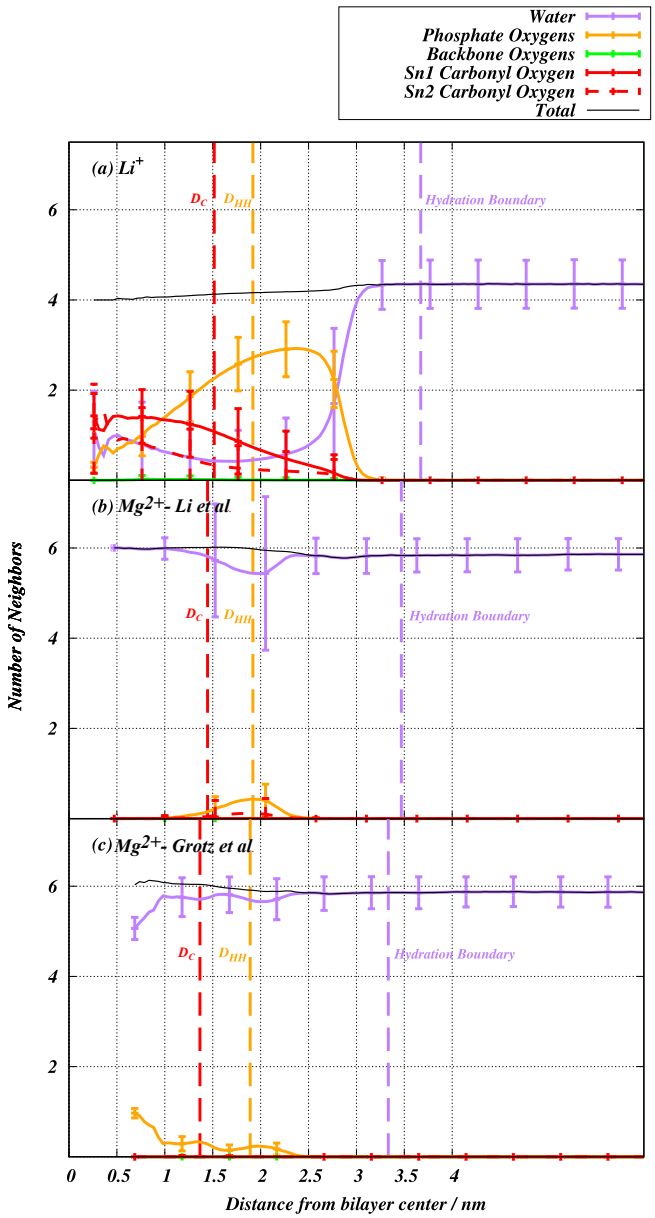

Figure 3.9: First shell coordination partners for Li^+ and Mg^{2+}in each simulation. These are computed over the last 150ns of simulation time in each system by counting the atoms of each species within a cutoff of each ion in the system, and histogramming the data based on the position of the ion. The dotted vertical lines denote the various bilayer surfaces – the vertical black line delineates the hydration boundary of the bilayer, the vertical blue line delineates the D_{HH}, and the vertical red line delineates the D_C. Li^+ (a) retains some water coordination well into the bilayer interface. Mg^{2+}–Li *et al.*(b) on the other hand does not lose nearly any first-shell coordinating waters in the bilayer, with some exchange for phosphate oxygens. The Mg^{2+}–Grotz *et al.*(c) parameters yield again more exchange but relatively far less than the monovalent ions.

imperfectly adsorbed ions by counting the number of ions with one or more water missing from their hydration shell, and then subtracting the number of perfectly adsorbed ions. We see more than twice the fraction of these ions in the Li^+ system compared to the Na^+system. Mg^{2+}shows an insignificant number of imperfectly adsorbed ions. Cl^-adsorbs in a large fraction imperfectly, as they begin to interact with the headgroup trimethylammonium.

The remaining ions are considered sterically adsorbed – this number is whatever ions remain after subtracting the perfect and imperfectly adsorbed ions from the number of overall adsorbed ions based on the position of the hydration boundary. Mg^{2+}seems to have most of the ions in this adsorption mode, where $Na^+$and Li^+ do not adsorb in this way in significant numbers. Additionally, Cl^-shows significant steric adsorption.

These data raise the question, what determines the mode of adsorption for a given ion? Since everything else, such as the substrate and the solvent, are held constant, the magnitude of the electric field at the position of the hydration shell of each ion is all that remains to determine the adsorption modality of the ion (figure 3.10). The electric field strength of each ion is calculated by applying Coulomb's law to a point charge, placing the test charge at the position of the first hydration shell of the ion in question. We note that the Mg^{2+}–Li *et al.*ion keeps waters slightly closer in the hydration shell compared to the Mg^{2+}–Grotz *et al.*model,resulting in a stronger electric field produced at this point by that ion. The largest ion with the smallest charge-density Na^+dehydrates completely in the largest fraction. Li^+ is smaller, and thus the field near the first shell is stronger and can hold waters a little better than Na^+. $Mg^{2+}$is similar in size to Li^+, but has a 2+ charge and holds onto waters substantially more than either of the monovalent ions. We also note that the $\left\|\vec{E}\right\|$ does not exhibit strong correlation with the fraction of the total number of ions adsorbed in each system, it only determines the adsorption mode.

3.6 Conclusions

Ion adsorption to porous interfaces is a complex interplay between solvent–surface, solvent–ion, and solvent–solvent interactions. With the solvent–surface and solvent–solvent interac-

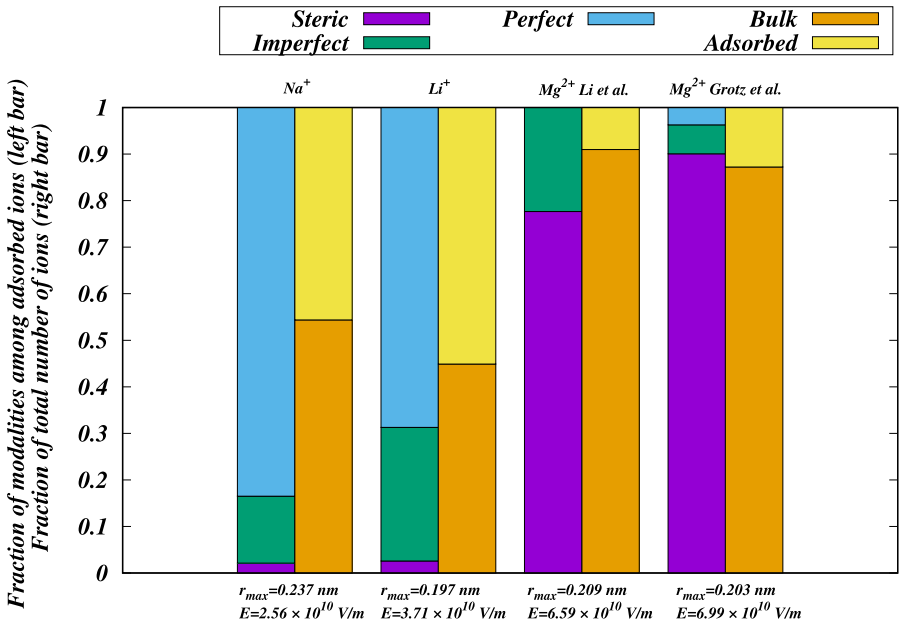

Figure 3.10: Fractions of ion-adsorption modality per each simulated system as a function of electric field strength. Here we show that the fractions of ions adsorbed in each modality follow a trend with an increasing electric field strength at the hydration shell of the cation. The overall trend is that the cations with the weakest field at the hydration shell position adsorb more perfectly, and as the field strength increases more ions adsorb imperfectly and then sterically. We note that little correlation with field strength can be seen in the total number adsorbed per ion.

tions held constant, we identify three different adsorption modalities of ions based on the degree of dehydration of the ion upon adsorption. The binding modality of a particular ion is significantly correlated with the electric field strength of the ion at the position of the first hydration shell, with stronger fields encouraging less dehydration of the ion upon adsorption to the surface (figure 8). This affect appears irrespective of the force-field used in the case of Mg^{2+}, which primarily adsorbs in the non-Langmuir type steric modality.

Furthermore, we identify several bilayer structural parameters that can be verified experimentally via x-ray scattering, neutron scattering, or various NMR methods (figures 1, 2, and 3 respectively). While the effect on lipid bilayer structure is not obvious in the electron density (figure 1), the pertubation can be seen in the D_B and water density – the less hydrated ions induce slight thickening of the lipid bilayer. This is reinforced by the chain ordering, where these ions increase chain ordering (figure 2) while the hydrated ions leave the

lipid bilayer structure similar to that of the no-salt case. These two results can be verified experimentally via solvent deuterium NMR, and lipid chain NMR. In the case of POPC, we expect deuterium solvent quadrupolar splitting values will be larger for the less hydrated ions $Na^+$and Li^+ when compared to the more hydrated Mg^{2+} (figure 3). We also expect the lipid chain order parameters to follow the opposite trend, with the monovalent ions inducing more ordering and Mg^{2+}inducing a smaller change from the no-salt system. We also expect that the adsorption of Mg^{2+}will be less detectable via the electrophoretic mobility of a vesicle in an MgCl salt solution, as the energy required to remove a hydrated ion from beneath the slip-surface of a vesicle may be low enough to allow their escape, while a dehydrated ion may remain adsorbed. These experiments are needed to verify these conclusions.

4 Alteration of bilayer structure by Mg^{2+}

4.1 Abstract

Developing molecular mechanics force fields to model interactions of biological membranes with Mg^{2+} cations is challenging. There are no direct estimates of the binding modes of Mg^{2+} ions with lipid headgroups or other phosphates in the condensed phase. Experimental data on lipid bilayers in Mg^{2+} solution are sparse and limited to biologically relevant but very low ion concentrations. At these concentrations, no statistically discernible effects on bilayer properties are observed. Simulations at these concentrations are difficult due to system size and the extensive conformational sampling required for force-field development. Considering these issues, we previously calibrated Mg^{2+}-lipid Lennard-Jones cross-terms using benchmarked quantum mechanical (QM) target data on small clusters of ions and ligands representative of common cation binding sites on 1-palmitoyl-2- oleoyl-sn-glycero-phosphatidylcholine (POPC). Our simulations with these new Mg^{2+} parameters yielded bilayer structures very similar to those without salt, in agreement with available experimental data. We adopted this strategy because it worked well for modeling membrane interactions with monovalent cations, for which additional experimental data are available. However, newer studies from our group show that for Mg^{2+} ions, the choice of target Mg^{2+}-lipid mimetic clusters is non-trivial. Inclusion of fully coordinated (6-fold) Mg^{2+} ions, which better represent potential ion-lipid structures in the condensed phase, may be critical for selecting models that reproduce experimental condensed-phase interactions of Mg^{2+} with nucleotide phosphates. Using this new protocol, we propose an additional set of Mg^{2+}-lipid interaction Lennard-Jones cross-terms. With this parameter set, we find that at concentrations between 100-200 mM, there is a systematic thickening of the lipid bilayer, not observed with our previous Mg^{2+}-lipid model. Additionally, compared to the earlier model, we observe more

Mg^{2+} adsorbed on the bilayer and a larger fraction directly coordinating lipid headgroups. However, the new model does not alter our previous observation that structural changes in the bilayer correlate with the amount of ionic charge directly coordinating lipid molecules.

4.2 Introduction

Salts have a well characterized behavior at interfaces in the condensed phase – ions form a classic double layer, where one charge accumulates near the substrate's surface, and the second charge then accumulates to compensate for that charge.[67] This can be explained using a mean-field approximation. However, the mean-field approximation does not provide details on specific interactions between ionic species and interface moieties. These details are non-trivial, especially in the case of phospholipid membranes, where the substrate itself is liquid and can adopt new conformations in response to ion adsorption.

Molecular dynamics (MD) simulations can, in principle, provide such details. However, the development of MD force fields for Mg^{2+}, and modeling their interaction with lipid bilayers poses significant challenges. Firstly, experimental data needed for force field development and validation is scarce. To our knowledge, there are no direct estimates on the binding modes of Mg^{2+} ions with lipid headgroups or any other phosphates in the condensed phase. Secondly, the effects of Mg^{2+} on lipid bilayer structure are only known for small concentrations of salt.[92,93] Simulations such low salt concentrations push the limits of hardware requirements for conformational sampling and force field testing. For example, in our previous simulations with Na^+,[78] we observed between 75-90 Na^+ ions adsorbed to an equilibrated lipid bilayer of 100 POPC molecules per leaflet. If we assume similar numbers of $Mg^{2+}$to be adsorbed, simulating at a biologically relevant concentration of 0.5 mM[94] will require more than 11 million waters. Additionally, since the residence time of waters in the first shell of Mg^{2+} is of the order of a microsecond,[95–97] capturing statistics on water-lipid exchanges in the first shell of Mg^{2+} requires prohibitively long MD simulations.

Considering these issues, we previously chose to calibrate Mg^{2+}-lipid Lennard-Jones (LJ) terms using benchmarked quantum mechanical (QM) target data clusters of small molecules

representative of the ion binding sites on 1-palmitoyl-2-oleoyl-sn-glycero-phosphatidylcholine (POPC).[78] Methyl acetate (MeAc) and diethyl phosphate (DEPh) were taken as small molecule representatives for lipid headgroups, and we targeted the changes in energy and structure associated with replacing water molecules in Mg^{2+}-water clusters with these smaller molecules. Using this model we found that at about 100 mM concentration, Mg^{2+}adsorbed into the headgroup region of POPC bilayer, but without losing its inner-shell waters (steric binding mode). We also observed formation of ion double layer at the headgroup-water interface. However, Mg^{2+} adsorption had a negligible effect on POPC bilayer structure. We posited that since our model at high salt did not affect bilayer structure, our model at low experimental salt concentration will also not affect POPC bilayer structure; making the result consistent with experiment. We adopted this strategy because we showed that it worked well for modeling interactions of lipid bilayers with monovalent cations.[78] Prior to our development, all simulations, irrespective of the employed force field, reported that monovalent salts thickened POPC bilayers.[6,13,23,98] In contrast, experiments reported insignificant changes in POPC lipid bilayer structure.[15,99] The use of our new Na^{+}-lipid LJ terms resolved this discrepancy to a large extent.[78] Recent developments in our lab, however, motivate us to explore a modified strategy for developing Mg^{2+}-lipid LJ terms. Our recent work of polarizable force fields for describing Mg^{2+}-protein/nucleotide interactions[100] suggests that perhaps within the classical framework, a single set of force field parameters for Mg^{2+}do not perform well at simultaneously reproducing energies of both fully coordinated (6-fold) and partially coordinated Mg^{2+} structures. Furthermore, force field developed using 6-fold coordinated structures performed excellently at reproducing not only local interactions of Mg^{2+} ions in clusters containing nucleotide phosphates but also condensed phase binding free energies of Mg^{2+} ions with nucleotides.[100] We have shown that this strategy also works for other cations[101] Fully coordinated 6-fold clusters of Mg^{2+} were not considered in the development of our previous Mg^{2+} model,[102] in which target data consisted of only partially coordinated structures of Mg^{2+}.

Here we apply this new protocol to develop a new set of Mg^{2+}-lipid LJ terms. Our target data consists exclusively of full 6-fold coordinated Mg^{2+} clusters with different combinations of waters and MeAc/DEPh ligands representative of the common binding sites on POPC. This allows us to focus our model parametrization on clusters that are more representative of the dense, bulk phase systems that we are interested in studying. As before, target data are obtained from benchmarked quantum mechanical (QM) vdW-inclusive density functional theory (DFT).

Using these new parameters, we perform MD simulations of POPC in $MgCl_2$ solution with the aim of comparing these results with those of our previous interaction model parameters. We also characterize their behavior using two different ion-water interaction parameter sets, parameters from Grotz *et al.*[86,103] that are developed to improve the first shell water residence times in comparison to experiments, and parameters from Li *et al.*[104] which target experimental hydration free energies.

In this way, we aim to test how changes to the Mg^{2+}–water and Mg^{2+}–lipid interaction models affect adsorption behavior and the resulting perturbations to bilayer structure. Our goal is not to validate a specific force field parameterization scheme, but to identify which structural metrics are most sensitive to these parameter choices and to provide a framework for future comparisons with experimental results. Essentially, in absence of appropriate experimental data, we have two competing models for describing Mg^{2+}-lipid interactions in MD simulations that point to different adsorption behavior.

4.3 Methods

4.3.1 Mg^{2+} Model Parameters

We perform a parameter search for the 7 pairs of Lennard-Jones (LJ) σ_{ij} and ϵ_{ij} interaction cross-terms of Mg^{2+} with lipid headgroup oxygens, carbon, and phosphorus atoms (see Table 4.2). This search is performed using target Mg^{2+} clusters containing water molecules and ligands that represent the major cation binding sites in phospholipid headgroups. The

clusters contain exactly 6 Mg^{2+} coordinators, representing a full first-shell coordination shell of Mg^{2+}.

These target clusters are geometry optimized at the DFT level using PBE0,[46] with the Tkatchenko–Scheffler dispersion corrections[47] as implemented in FHI-aims.[44] Geometry optimizations are first performed with the "light" basis set as provided in the FHI-aims software package, and then with the "really-tight" basis. Both geometry optimizations are performed with a force convergence threshold of 0.005 eV/Å. Energies of these optimized clusters are used to compute substitution energies, and geometries are computed as an array of distances between all particles in the cluster and the cation. As before,[78] we do not target the interaction energies of Mg^{2+}in clusters. Instead we target substitution energy, that is the energy associated with replacing water molecules with ligands (X) representing the POPC headgroup:

$$(\mathrm{MgW}_6)^{2+} + n\mathrm{X} \longleftrightarrow (\mathrm{MgW}_{6-n}\mathrm{X}_n)^{2+} + n\mathrm{W}. \tag{4.1}$$

The substitution energy associated with this reaction is

$$\Delta E_{sub} = E_{MgWX} + nE_W - E_{MgW} - nE_X \tag{4.2}$$

where E_{MgW} is the energy of the optimized geometry of Mg^{2+} cluster with 6 waters and E_{MgWX} is the energy of optimized geometry the mixed cluster of Mg^{2+} consisting of n X ligands and $6-n$ waters. We use two different ligands, methyl acetate that represents the ester-fragment connecting the lipid acyl chains to the glycerol backbone, diethyl phosphate that represents the phosphate fragment in the lipid headgroups. E_W and E_X are, respectively, the energies of the optimized geometries of the isolated water and isolated ligands.

Parameter optimizations were performed using the ParOpt software package developed by our group.[37] We used the Nelder-Mead optimizer to simultaneously optimize the 14 LJ cross terms for each atom type in our target clusters. Constraints are detailed in Table **??**. We first perform parameter searches using a full-random simplex initialization, to obtain 400

Table 4.1: Parameter bounds and active constraints. ε and σ correspond to Lennard-Jones well depth and size.

Parameter	Min	Max	Additional Constraint
MGCH3-ε	0.0	2.19239	
MGCH3-σ	0.2	0.5	
MGCH2-ε	0.0	2.13238	
MGCH2-σ	0.2	0.5	
MGOA-ε	0.0	30.0	
MGOA-σ	0.2	0.5	
MGP-ε	0.0	30.0	
MGP-σ	0.2	0.5	
MGOM*-ε	0.0	30.0	
MGOM*-σ	0.2	0.5	$\sigma_{\text{MG-OM*}} = \min\{\sigma_{\text{MG-P}},\ \sigma_{\text{MG-OM*}}\}$
MGCO*-ε	0.0	2.06152	
MGCO*-σ	0.2	0.5	
MGO*-ε	0.0	30.0	
MGO*-σ	0.2	0.5	

converged simplexes, regarding a simplex as converged if the RMSD collapses to 10×10^{-3}. The best parameters from this search are then used to perform another search using around-point initialized simplex, with an RMSD cutoff of 10×10^{-5}, again for 400 converged simplexes. From this search, we select the parameters that balance the error in substitution energies and geometries simultaneously. These optimized parameters are provided in table 4.2. We denote these parameters as the Mg^{2+} 2025 model, and compare them with our parameters from Saunders *et al.* 2024,[102] which we will refer to as the Mg^{2+} 2024 model. There are substantial differences between the Mg^{2+} 2024 and Mg^{2+} 2025 models, with the greatest changes in the size of the well depth ϵ_{ij} for MG-OA, MG-P, and MG-OM*

The substitution energies before and after optimization are compared to target QM values in Table 4.3. The geometries before and after optimization are compared to QM geometries in figure 4.1.

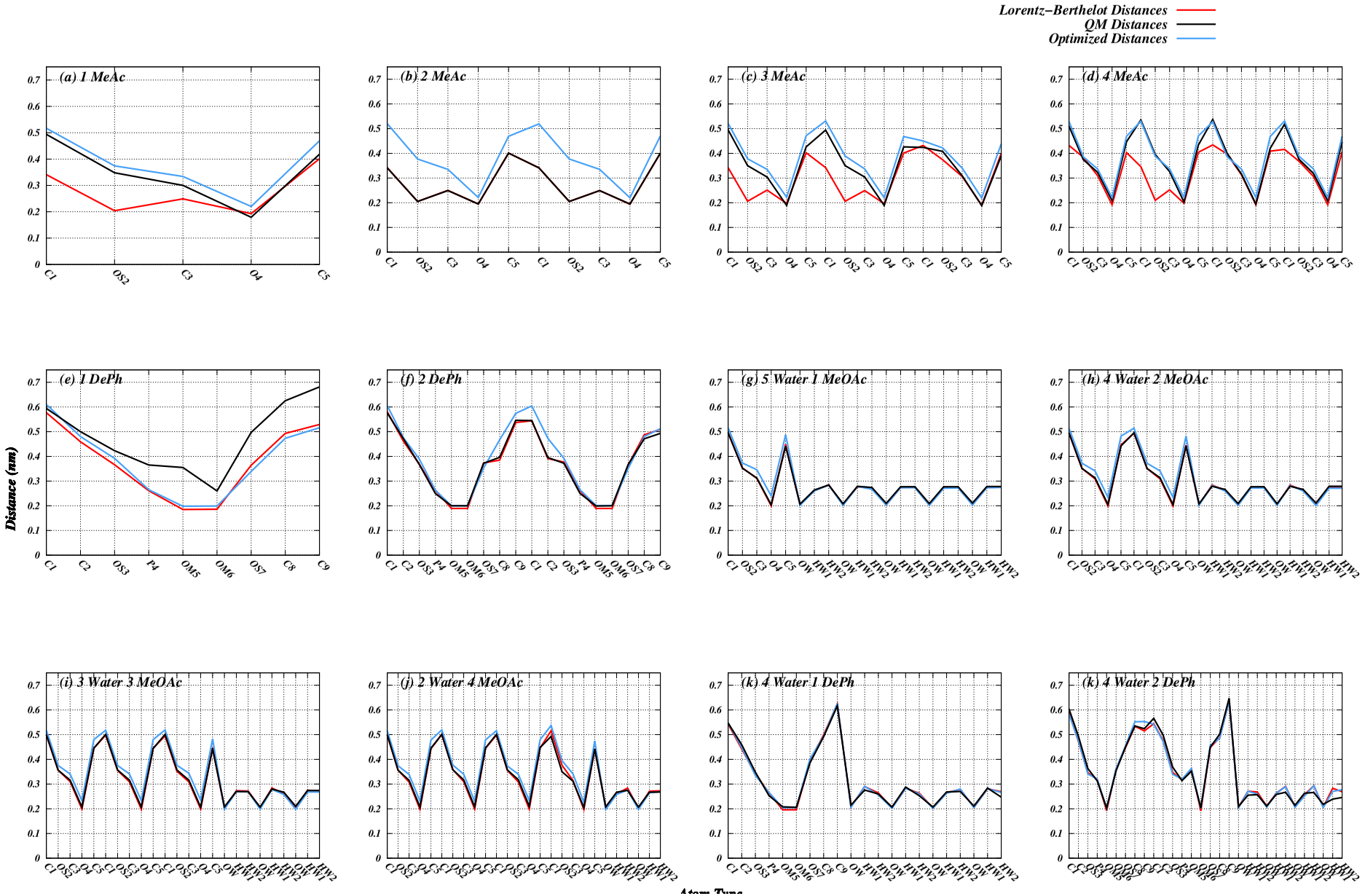

Figure 4.1: Comparison between distances of Mg^{2+} atom from other atoms in clusters optimized using QM and MM.

We note substantial improvements in both substitution energies with a minimal loss of accuracy in geometries, with parameter optimization reducing mean absolute error in ΔE_{sub} from 0.26 to 0.01.

Table 4.2: Lennard-Jones parameters for magnesium interactions: well depth ϵ_{ij} (kJ/mol) and distance parameter σ_{ij} (nm), comparing the 2025 optimized model, the 2024 model, and the original LB-rules.

	2025		**2024**		**LB-rules**	
Parameter	$\boldsymbol{\varepsilon}$	$\boldsymbol{\sigma}$	$\boldsymbol{\varepsilon}$	$\boldsymbol{\sigma}$	$\boldsymbol{\varepsilon}$	$\boldsymbol{\sigma}$
MG-CH3	0.60498	0.22161	0.68709	0.14257	0.19239	0.30856
MG-CH2	1.36553	0.41404	0.63126	0.20617	0.13238	0.32468
MG-OA	25.25725	0.30372	5.05190	0.26223	0.19044	0.26890
MG-P	29.74732	0.23348	3.89200	0.27811	0.32318	0.29044
MG-OM*	22.04699	0.20018	3.22262	0.17691	0.20771	0.26469
MG-CO*	0.57040	0.42212	0.56152	0.37127	0.06152	0.34796
MG-O*	2.06827	0.24468	2.43058	0.13069	0.20771	0.26469

Table 4.3: Energies (kJ/mol) associated with substituting n water molecules in low coordination clusters, and in 6-fold Mg-water clusters with n methyl acetates (MeAcs) or n diethyl phosphates (DEPhs). Substitution energies are defined in equation 4.2.

	PBE0+VdW	LB Rules			2024			2025		
System	Ref.	Energy	Abs.%	MAPE	Energy	Abs.%	MAPE	Energy	Abs.%	MAPE
1MeOAc	−268.702	−130.319	0.515		−299.844	0.116		−32.724	0.878	
2MeOAc	−449.770	−243.856	0.458		−545.386	0.213		−59.544	0.868	
3MeOAc	−550.360	−263.968	0.520		−598.606	0.088		−42.191	0.923	
4MeOAc	−609.631	−341.534	0.440	0.483	−690.483	0.133	0.137	−98.578	0.838	0.877
1DEPh	−942.545	−972.812	0.032		−1063.300	0.128		−772.729	0.180	
2DEPh	−1302.053	−1051.842	0.192	0.112	−1488.761	0.143	0.136	−1248.054	0.041	0.111
5W 1MeOAc	−71.288	−91.759	0.287		−165.829	1.326		−71.280	0.000	
4W 2MeOAc	−127.201	−177.528	0.396		−316.012	1.484		−122.881	0.034	
3W 3MeOAc	−166.160	−253.576	0.526		−402.648	1.423		−167.835	0.010	
2W 4MeOAc	−192.534	−317.715	0.650	0.465	−507.049	1.634	1.467	−192.275	0.001	0.011
4W 1DEPh	−775.546	−640.060	0.175		−848.090	0.094		−754.821	0.027	
4W 2DEPh	−1279.754	−1198.284	0.064	0.119	−1519.772	0.188	0.141	−1333.653	0.042	0.034

Table 4.4: Shifts in substitution energies relative to LB Rules: $\Delta E_{\text{sub}}^{202X} - \Delta E_{\text{sub}}^{\text{LB}}$ for 2024 and 2025, and their difference [2025−2024]. Positive values mean 202X is less stabilizing (less negative) than LB; negative values mean more stabilizing than LB.

Cluster	$\Delta E_{\text{sub}}^{2024} - \Delta E_{\text{sub}}^{\text{LB}}$	$\Delta E_{\text{sub}}^{2025} - \Delta E_{\text{sub}}^{\text{LB}}$	[2025−2024]
1MeOAc	−169.525	97.595	267.120
2MeOAc	−301.531	184.311	485.842
3MeOAc	−334.638	221.777	556.414
4MeOAc	−348.949	242.956	591.905
5W 1MeOAc	−74.071	20.479	94.550
4W 2MeOAc	−138.484	54.647	193.131
3W 3MeOAc	−149.072	85.741	234.813
2W 4MeOAc	−189.334	125.440	314.774
1DEPh	−90.488	200.083	290.571
2DEPh	−436.919	−196.211	240.708
4W 1DEPh	−208.031	−114.761	93.270
4W 2DEPh	−321.488	−135.369	186.119

4.3.2 Bilayer Construction

Simulation systems are prepared following the procedure in Saunders *et al.*2024,[102] by creating a bilayer leaflet of 100 POPC lipids along a 10 by 10 grid. This leaflet is reflected along the z-axis to produce the second leaflet. Then 60,000 waters are added along the box z-dimension. $MgCl_2$is added by randomly replacing 216 waters with Mg^{2+}, and 432 waters with Cl^- for a starting concentration of 200 mM $MgCl_2$. The resulting simulation box is used in both Mg^{2+} 2025 HFE and micro simulations – energy minimization and annealing were done under the matching parameter set for the simulation. Systems are energy minimized using the steepest-descents algorithm to remove bad-contacts. Following energy minimization, both systems are allowed to settle in an NPT dynamic run at a temperature of 250 K for 1 ns. Systems are then annealed by heating to 350 K, and cooling in steps of 10 K to the simulation run temperature of 300 K in steps of 155 ps.

4.3.3 Molecular Dynamics

The Mg^{2+} 2025 parameters are used in two 1 μs long simulations of POPC with $MgCl_2$, one using the water–Mg^{2+} interaction term computed using Mg^{2+} HFE model of Li *et al.*,[104] and one using the Mg^{2+} micro from Grotz *et al.*[86,103] Lipid bonded and non-bonded interactions are described using the gromos 43-a1s3 force-field.[18] Simulations were performed using Gromacs version 2024.0[105] with an integration time step of 4 fs. Neighbor searching is performed every 2 steps using Verlet neighbor-lists. The PME algorithm is used for electrostatic interactions. with a cut-off of 1.6 nm. A reciprocal grid of 52 x 52 x 240 cells is used with 4th order B-spline interpolation. A single cut-off of 1.6 nm is used for Van der Waals interactions. Temperature coupling is done with the Nose-Hoover algorithm holding the system temperature at 300 K.[56] Pressure coupling is done with the Parrinello-Rahman algorithm holding the system pressure at 1 atm.[57]

Trajectories are analyzed using tools provided in the Gromacs software package,[105] in-house code developed using the Gromacs API, and using the MDanalysis python package.[87,88]

4.4 Results and Discussion

4.4.1 Water structure, and hydration boundaries

To differentiate interfacial ions from those in the bulk solvent, we first need to define at interfacial boundary. As before,[102] we do this using the orientational ordering of water molecules. Waters near the lipid bilayer interface are ordered due to the electrostatic and steric interactions with the lipid bilayer, as well as interactions with dissolved salts. The orientation of these waters can be probed by computing the orientational order parameters $P_1 = \langle \cos\beta \rangle$ and $P_2 = \langle \frac{1}{2}(3\cos^2\beta - 1 \rangle$, where β is the angle made between the water OW-HW1 vector and the box z-axis. The hydration boundary marks the location where water molecules become orientationally isotropic, beyond which they no longer contribute to quadrupolar NMR splitting. We use this boundary to distinguish between adsorbed ions and ions in bulk solvent. In our previous work,[102] we demonstrated that ion densities outside this boundary follow Poisson–Boltzmann theory, while those inside deviate from it. This breakdown in mean-field behavior indicates a specific interaction with the membrane.

To compute P_1 and P_2, we divide the simulation unit cell into 2000 slices along the membrane transverse (z-) axis. The average values over the last 150 ns of the simulation are plotted in figure 4.2, with points shown for every 200 slices.

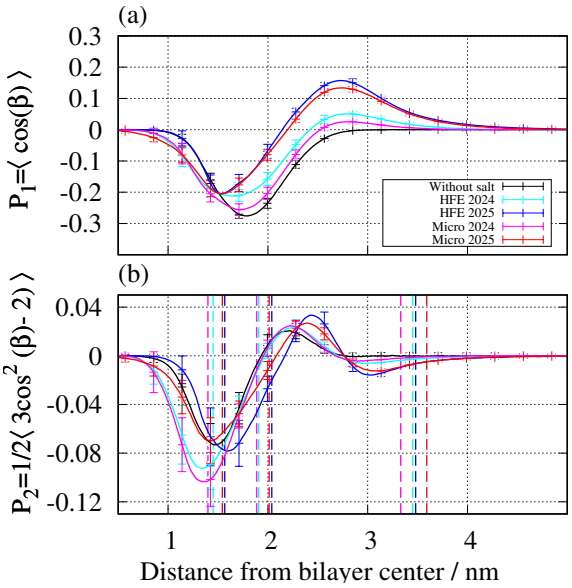

Figure 4.2: Water orientation order parameters. The first order parameter represents an in-out ordering with respect to the bilayer center, and the second is related to the orientation of the quadrupole moment of the box. A value of zero is completely parallel with the box axis. The first order parameter indicates a significant increase in the positive ordering induced by the Mg^{2+} 2025 parameters compared to the no-salt and the Mg^{2+} 2024 simulations. The second order parameter indicates increased ordering as on approaches the bilayer starting from the boundary with bulk solvent, indicated by the set of dotted lines furthest from the bilayer center point. Ordering increases as we approach the bilayer D_{hh}, indicated by the second set of dotted lines. There is also a steeper decline as one follows the plot into to the acyl chain region denoted by the bilayer $2D_C$ – denoted by the innermost dotted lines – in the Mg^{2+} 2025 Micro system. We note that the hydration boundary of both of the 2025 simulations is further from the bilayer center compared to the 2024 simulations, resulting in a larger region of biological water at the bilayer surface. This alone can result in a greater number of ions adsorbed in at least the *steric* adsorption mode.

The histogram of P_2 is used to calculate the *hydration boundary* of the lipid bilayer system. The outermost region of negative ordering is fitted to an exponential function, and the length scale of the exponential is used to find the location where P_2 is considered to be effectively zero. Lines to delimit these values are drawn on the plot in figure 4.2, and these positions are noted for each bilayer in table 4.5.

4.5 Mg^{2+} Adsorption Behavior

We classify any ion within the hydration boundary as at least sterically adsorbed, with further distinction – steric, imperfect, or perfect – based on how much dehydration the ion

Table 4.5: Bilayer structural parameters. The bilayer hydration boundary is defined as the position away from the bilayer center beyond which solvent is isotropic, and denotes bulk solvent from bound solvent. The number of adsorbed charges in each adsorption mode are within the hydration boundary of the system, and are further classified by the degree of loss of hydration water – steric adsorbed have lost no water, imperfect have lost at least one, and perfect have replaced all water oxygens for lipid oxygens. The bilayer thickness D_{hh} is defined as the distance between the peaks in the electron density of the system, roughly localizing the phosphate groups. $2D_C$ is the thickness of the acyl-chain region of the bilayer, and is measured as the distance between the Gibb's surfaces of the acyl-chain probability density. Lipid component volumes V_{CH3} and $V_{CH1/CH2}$ are computed using the method of Petrache *et al.*[60] V_C is computed from the component volumes by multiplying by the number of these components in each acyl chain. $A_L = \frac{V_C}{D_C}$ is the two-dimensional area occupied per lipid on the bilayer surface. We note a correlation between simulations with larger numbers of adsorbed charges and perturbation of the bilayer structure from that of the simulation without salt, especially in the bilayer $2D_C$.

	Without salt	Mg^{2+} 2024 HFE	Mg^{2+} 2024 Micro	Mg^{2+} 2025 HFE	Mg^{2+} 2025 Micro
Hydration Boundary (Å)	N/A	34.5	33.3	34.8	35.9
Perfectly Adsorbed Charges	0	1.90	0.00	0.00	0.00
Imperfectly Adsorbed Charges	0	3.68	6.23	28.43	96.93
Sterically Adsorbed Charges	0	37.11	31.45	106.00	20.11
D_{HH} (Å)	37.57 ± 1.27	38.15 ± 1.20	37.75 ± 1.19	40.75 ± 0.92	40.26 ± 0.96
$2D_C$ (Å)	26.98 ± 0.35	28.99 ± 0.31	28.08 ± 0.40	31.45 ± 0.29	30.84 ± 0.29
$V_{CH1/CH2}$ (Å^3)	26.33 ± 0.05	26.21 ± 0.05	26.33 ± 0.05	26.22 ± 0.04	26.12 ± 0.04
V_{CH3} (Å^3)	54.97 ± 0.39	54.77 ± 0.39	54.98 ± 0.40	54.74 ± 0.24	55.19 ± 0.26
V_C (Å^3)	899.72 ± 1.01	895.85 ± 1.05	899.83 ± 1.06	895.94 ± 0.95	894.00 ± 1.11
$A_L = \frac{V_C}{D_C}$	66.71 ± 0.89	61.80 ± 0.66	64.10 ± 0.92	56.97 ± 0.54	57.98 ± 0.57

undergoes when approaching the bilayer center. A *perfectly* adsorbed ion has lost all waters in its first hydration shell and an *imperfectly* adsorbed ion has lost at least one water from its first coordination shell. *Sterically* adsorbed waters have their first shell of waters intact, but they are spatially located within the *hydration boundary* of the lipid bilayer. To evaluate this, we define a cutoff to the first hydration shell, computed from radial distribution functions. The cutoff used for Mg^{2+} in all systems is 3.3 Å, which captures the first peak for Mg^{2+} and lipid oxygens, water, and Cl^-. We compute the nearest oxygens (lipid phosphate, glycerol, ester fragment, Cl^-, or water) within these cutoffs of cations across the simulation system, and generate a histogram averaged over slices and then over the last 150 ns of simulation time. This histogram is shown in figure 4.3.

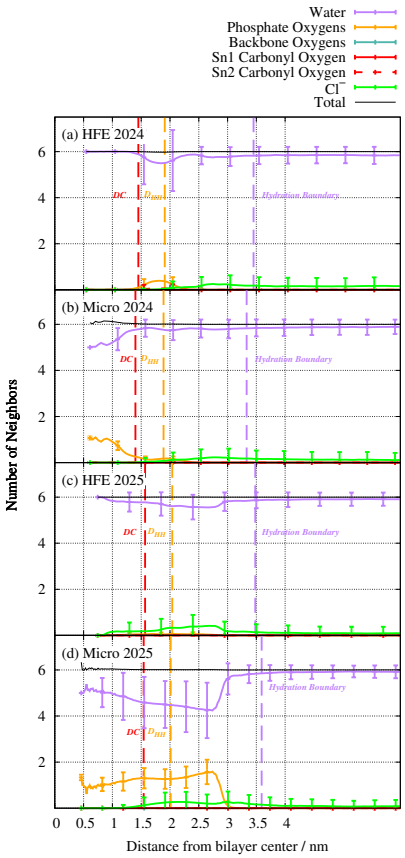

Figure 4.3: Coordination partners of Mg^{2+}. We note that while the Micro water with the 2024 parameters do result in some dehydration of the Mg^{2+} in the headgroup region of the bilayer, both 2024 parameters yield nearly no dehydration of Mg^{2+} at any location in the simulation box. The 2025 HFE parameters still largely do not dehydrate, but the 2025 Micro parameters do result in loss of 1-2 waters from the Mg^{2+} coordination shell within the headgroup region. We see substantial interaction with the headgroup phosphate oxygens, and no significant interaction with the glycerol or ester linkage oxygens. We also note the increased interaction with Cl^- in the simulations using the 2025 parameters compared to both simulations with the 2024 parameters. The number of first shell Cl^- remains below one per ion in any simulation.

We note that the Mg^{2+} 2024 parameters result in very little dehydration of ions, throughout the simulation box. The 2025 parameters result in loss of 1-2 waters as the ion approaches the bilayer center, with the Mg^{2+} 2025 Micro parameters resulting in the greatest degree of dehydration among parameter sets. The Mg^{2+} 2025 HFE parameters result in some loss of first shell water, but no replacement in the first shell with lipid oxygens. There are a significant number of Mg^{2+}-Cl^- pairs, where a single Cl^- replaces a water in the first shell

of Mg^{2+} as the ion moves into the lipid-occupied region of the bilayer. If these ions do not otherwise lose water for lipid parts, they are counted as *sterically* adsorbed.

The Mg^{2+} 2025 Micro parameters appear to have a preference for direct interaction with the phosphate group oxygens when dehydrated, and none of the Mg^{2+} parameters studied result in significant direct interaction with the ester fragment and glycerol oxygens. There are also far fewer pairs with Cl^- under this parameter set. Fractions of ions in each adsorption mode have been computed by counting the number of ions in each frame within the hydration boundary, and the number of those that have lost one water, or all of their waters. We compute averages over the last 150ns, and then fractions of the total adsorbed ions present in each mode. These values are shown in figure 4.4, alongside the fraction of ions adsorbed vs the fraction remaining in bulk solvent.

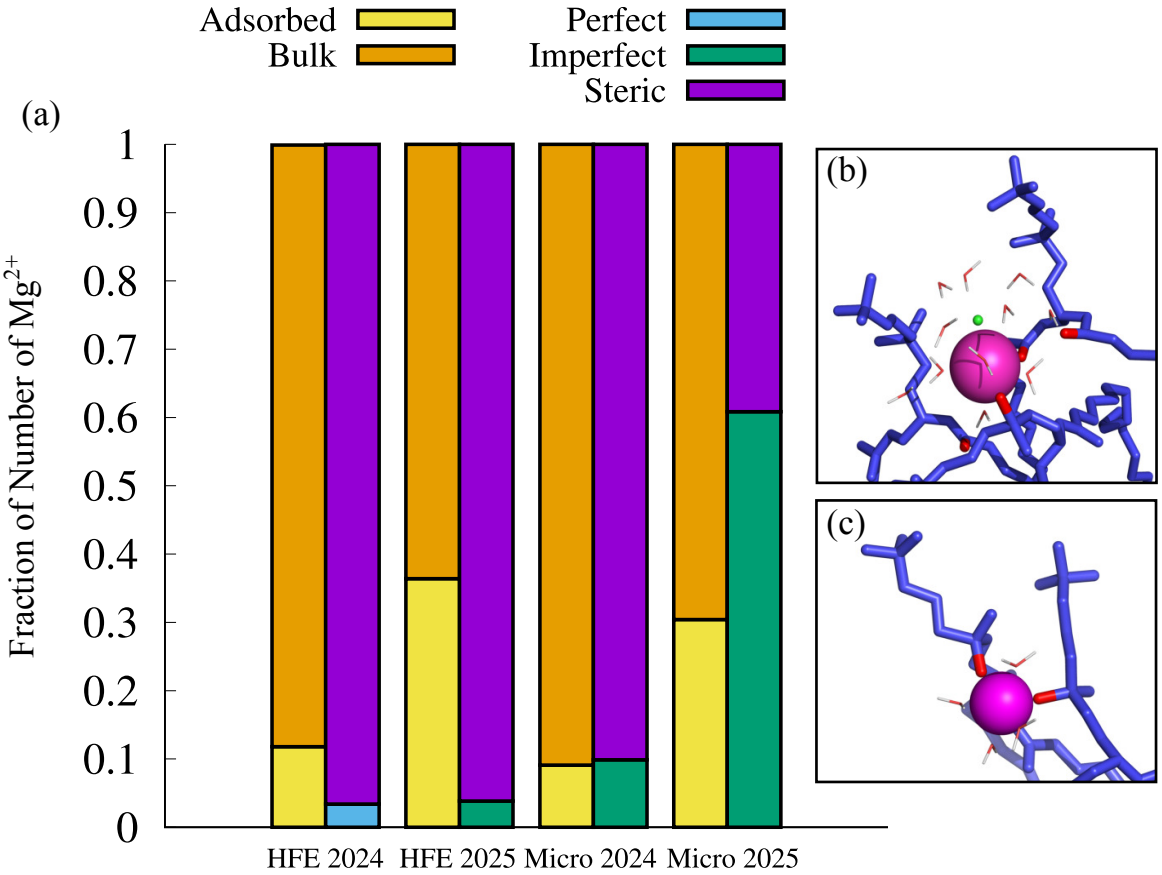

Figure 4.4: (a) Distribution of Mg^{2+} ions in different membrane adsorption modes. Mg^{2+} are first classified into those in bulk and those adsorbed in membranes. Among those adsorbed in membrane, Mg^{2+} are further classified into those that are perfectly, imperfectly and sterically adsorbed. We note that compared to the 2024 models, the 2025 models result in increased membrane adsorption, and among the adsorbed Mg^{2+}, the 2025 models result in increased direct coordination with lipid headgroups. Next to the plot, we show examples of Mg^{2+} in the *steric* (b) and *imperfect* (c) adsorption modes from our simulations. The *perfect* adsorption mode does not occur in a significant frequency in Mg^{2+}, so an example is not included. We note that in this example of the *steric* adsorption mode (b) there is a Cl^- (green) included in the hydration shell of the Mg^{2+} ion (magenta). This is an example of a partial-ion pair, which while having lost a water from the first-shell, it is not coordinating lipid components directly – these are counted as sterically adsorbed.

The 2025 parameters result in significantly more adsorbed ions and as a result more adsorbed charges in both cases, with the most increased in the Mg^{2+} 2025 HFE simulation. We count the number of adsorbed charges in each adsorption mode by multiplying the number of ions in each mode by their charge; this would be 2 charges per Mg^{2+}, and a Mg^{2+} paired with a Cl^- counts a single charge. These numbers can be seen in table 4.5 rows 2-4. We also

note an increase in imperfectly adsorbed ions in the Mg^{2+} 2025 HFE simulation. However, the Mg^{2+} 2025 Micro parameters result in ions shifting to the majority in the imperfect adsorption mode from the steric mode seen in both 2024 simulations. The Mg^{2+} 2025 HFE parameters still remain with the largest fraction of ions in the steric adsorption mode. These differences in the distribution of adsorbed Mg^{2+} ions – particularly the rise in imperfect adsorption for Mg^{2+} 2025 Micro – raises the question of how such interactions reshape the membrane itself. We therefore turn to a structural analysis of the lipid bilayer to evaluate the consequences of these adsorption patterns.

4.6 Bilayer Structure

The effect of changes in ion adsorption on bilayer structure was assessed through several structural parameters. Electron densities were computed using the `gmx density` tool included in the GROMACS software suite. Histograms were calculated in 1 ns chunks along the bilayer normal (z-axis) and centered at zero using the position of minimum density, corresponding approximately to the bilayer midplane. These histograms were then symmetrized about the center and averaged over the final 150 ns of each trajectory.

From the resulting profiles, we calculated the small-angle X-ray scattering (SAXS) form factor by subtracting the average water electron density and applying a cosine transform. Electron density profiles and corresponding simulated SAXS form factors are shown in Figure 4.5.

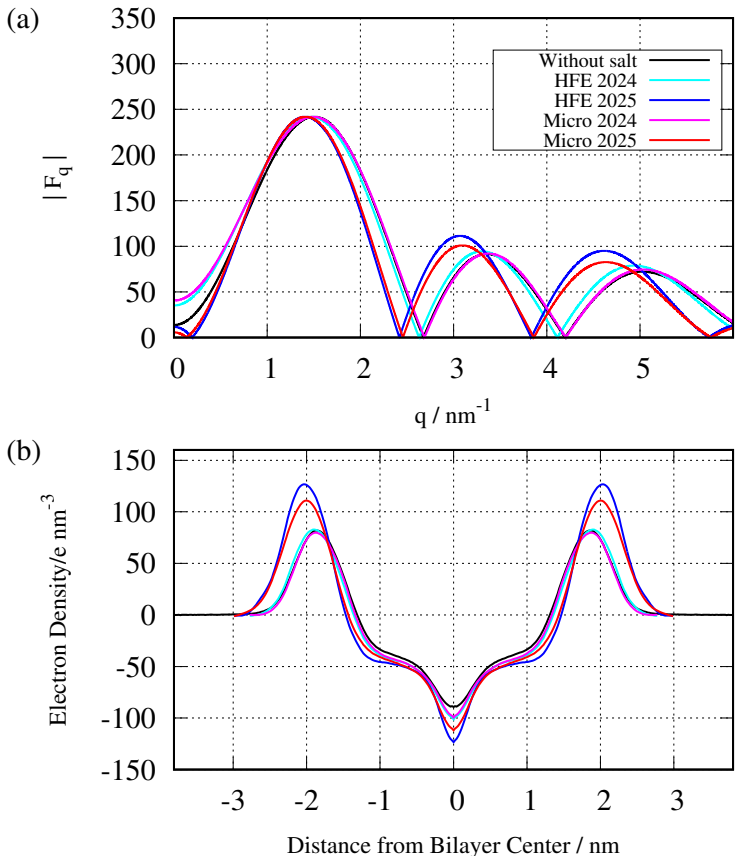

Figure 4.5: SAXS form-factors and associated electron densities for Mg^{2+} simulations. (a) Mg^{2+} 2024 under both Micro and HFE has little effect in changing the bilayer form-factor compared to that of the no-salt simulation, consistent with the available experimental results at lower ion concentrations. Conversely, both of the simulations with 2025 parameters result in significant thickening of the bilayer. This is also seen in the associated electron densities (b), where we see much taller peaks that are further apart in the Mg^{2+} 2025 simulations than that obtained from the 2024 simulations.

We note significant broadening of the bilayer peak-to-peak distance in the electron densities of the 2025 systems, compared to the 2024 systems. Additional structural parameters are computed from the various number density histograms of our simulations. Similarly to the electron densities, we use the gromacs GMX density tool to compute the number density histogram over 1ns chunks of our simulation. We then center these histograms using the centerpoint found from the electron density at each 1ns chunk. These histograms are then symmetrized, and averaged over the last 150ns of simulation time. These can be seen for solvent and lipid headgroup components of in figure 4.6. We note greater accumulation of

Mg^{2+} in the Mg^{2+} 2025 simulations, with greater peak densities of cations in the headgroup regions, with the largest peak in the Mg^{2+} 2025 HFE system.

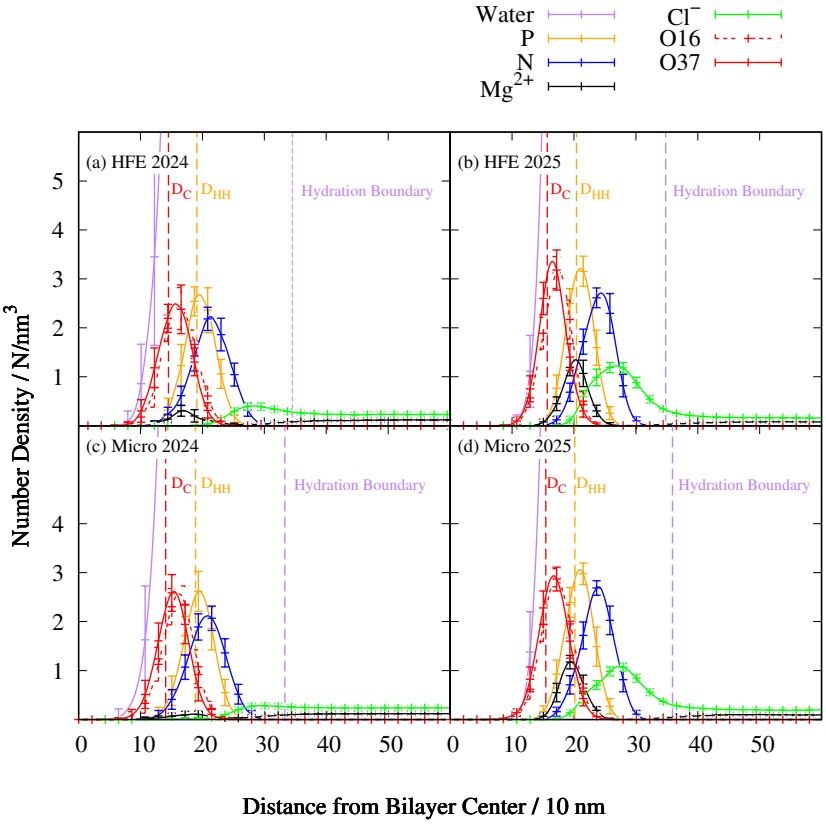

Figure 4.6: Number density histograms of lipid headgroup components. Vertical lines denote the bilayer structural features such as the hydration boundary in purple, the D_{hh} in orange and the $2D_C$ in red. We note that within the hydration boundary of each system there is accumulation of ions – anions accumulate near the trimethylammonium nitrogen and cations accumulate near the phosphate group. The Mg^{2+} 2025 parameters have a much larger accumulation of both ions in the headgroup region of the bilayer compared to the Mg^{2+} 2024 systems.

The bilayer thickness D_B and the acyl-chain region thickness $2D_C$ are computed as the distance between the Gibb's surfaces of the probability densities of solvent and the lipid acyl-chain carbons, respectively.[62] These are computed from the number densities of these species for each 1ns chunk of the simulation, and then averaged over the last 150ns of the simulation time. The values for these are listed in table 4.5. We also compute the lipid component volumes using the method of Petrache *et al.*[60] To do this, we partition the lipid

number densities into headgroup and chains, with the headgroup consisting of any particles above the acyl chain ester fragment and the chains as just the acyl chain carbons. We partition the chains into groups of CH2+CH1, and the terminal CH3 atoms. We optimize the following objective function to partition the volume in each histogram slice z_j from the number densities to these groups:

$$\Omega(v_i) = \sum_{z_j}^{\rho_s} \left(1 - \sum_{i=1}^{N_{\text{groups}}} \left(\rho_i(z_j)(v_i)^2\right)\right). \tag{4.3}$$

From this we obtain partial volumes for the groups $v_{\text{CH1\&CH2}}$, v_{CH3}, $v_{\text{Headgroup}}$. We equate the $V_{CH2} = v_{CH1\&CH2}$ as these densities have significant overlap, and thus the volumes cannot be separated. This, along with the $V_{\text{CH3}} = v_{\text{CH3}}$ can be seen in table 4.5. These volumes multiplied by the number of each moiety in a lipid are used to compute V_C. Finally, we compute the $\text{A}_\text{L}$as the ratio $2 \times V_c/2D_C$.

4.6.1 Acyl-Chain order parameters

Acyl-chain order parameters are computed using the method outlined by Douliez *et al.*[64] (see figure). We note that the 2024 Mg^{2+} parameters do not significantly increase the acyl-chain ordering from that of the system simulated without salt.The 2025 Mg^{2+} parameters have a much greater effect on the ordering. We can compute the lipid bilayer thickness using the acyl-chain order parameter by using the "first-order mean-torque model" of Petrache *et al.*[61,106] This is done by taking the average S_CD from the experimental plateau region – the set of carbons where the experimental S_CD does not change detectably.[61,107] This can be used to compute the average segmental projection onto the bilayer normal $\langle x \rangle$:

$$\langle x \rangle = 1 - \frac{1}{\varepsilon_1}, \varepsilon_1 = \frac{2}{1 - \sqrt{\frac{-8\left\langle S_{CD}\right\rangle - 1}{3}}}, \tag{4.4}$$

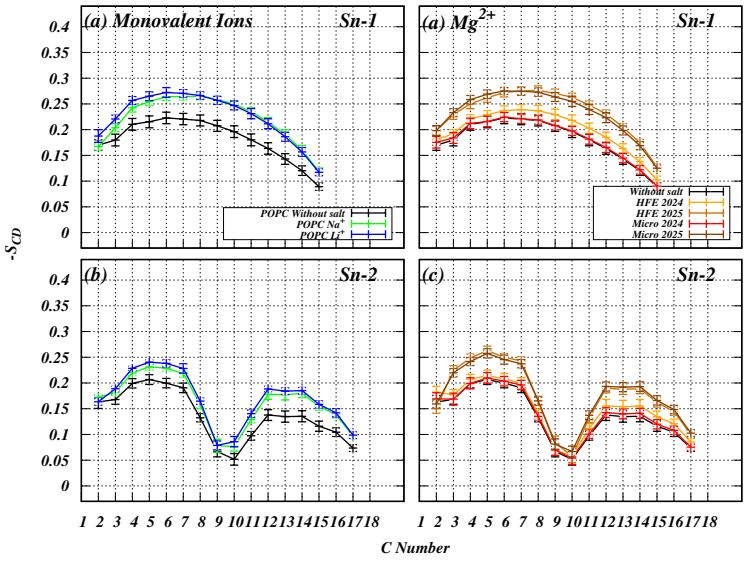

Figure 4.7: Acyl-chain CD Order parameters. We note increased ordering in the simulations using the 2025 model parameters, while the 2024 parameters result in bilayers that remain very similar to the simulation without salt.

where ε_1 is the mean-torque parameter. We compute the corresponding squared projection $\langle x^2 \rangle$ from the S_{CD} using the following equation:

$$\langle x^2 \rangle = \frac{1 - 4\langle S_{CD} \rangle}{3}, \tag{4.5}$$

which can be used together to compute the area factor:

$$q = 3 - 3\langle x \rangle + \langle x^2 \rangle. \tag{4.6}$$

This is then used to compute both the area per lipid and the thickness of the acyl-chain region of the lipid bilayer:

$$\langle A \rangle = q \frac{4V_{\mathrm{CH_2}}}{D_M}, \tag{4.7}$$

Using V_{CH_2} computed from the number densities, and the bond length $D_M = 2.54$. We approximate the V_{CH2} in two ways from the $v_{CH2\&CH1}$ – first by directly using $V_{CH2} =$

$v_{CH2\&CH1}$, and second by using the common approximation of $\frac{V_{CH2}=v_{CH3}}{2}$.[61] These values are listed in table 4.6. We can also compute the acyl chain thickness:

$$D_C = \frac{n_c D_M}{2q}, \tag{4.8}$$

with $n_c = 16$ as the number of carbons in the Sn-1 chain. These values can be seen in table 4.6. Notably, the $2D_C$ for all systems studied is slightly smaller than what we compute from the number densities, but follows similar trends. The A_L computed here only relies on the volume of the CH2 moiety, and ends up with again quite different results than what we computed from $2V_C/2D_C$.

We note that in the systems with the smallest number of adsorbed charges in non-steric modes (perfect and imperfect) – in this case the 2024-Mg^{2+}parameters, show the smallest increase in $2D_C$. The Mg^{2+} 2025 systems have the greatest number of adsorbed charges in non-steric modes, and have the largest increase in $2D_C$ over the system simulated without salt. We note that this trend is not followed necessarily in the D_{hh}, which is not a reliable measures of bilayer thickness due to the effect of headgroup tilt angle, and overlapping number densities of water and salt in the headgroup region. Together, we note that the systems with the greatest number of charges in the Langmuir-type (non-steric) modes correlate with an increase the bilayer thickness (figure 4.8)

Table 4.6: Area factor, acyl chain region thickness and area per lipid. These values are computed via the method described in Petrache *et al.*[106] This provides us with another measure of the acyl chain thickness. We note that the thickening of the lipid bilayer remains consistent with the acyl chain thickness $2D_C$ computed from the number densities.

				2024		2025	
	Without salt	Na^+	Li^+	Mg^{2+}-HFE	Mg^{2+}-Micro	Mg^{2+}-HFE	Mg^{2+}-Micro
q	1.39 ± 0.14	1.30 ± 0.11	1.29 ± 0.02	1.36 ± 0.02	1.41 ± 0.03	1.24 ± 0.01	1.26 ± 0.01
$2D_C$ NMR (Å)	28.67 ± 2.97	30.85 ± 2.57	31.53 ± 0.53	29.98 ± 0.47	28.84 ± 0.57	32.66 ± 0.33	32.17 ± 0.30
A_L from $v_{CH2\&CH1}$	55.14 ± 1.21	51.98 ± 0.69	53.13 ± 0.91	55.98 ± 0.92	58.45 ± 1.16	51.37 ± 0.52	51.97 ± 0.49
$((V_{CH3}/2)$	30.87 ± 0.30	29.65 ± 0.24	27.58 ± 0.19	27.40 ± 0.19	27.49 ± 0.20	27.38 ± 0.13	27.59 ± 0.13
A_L from $(V_{CH3}/2)$	68.26 ± 1.95	61.10 ± 0.99	56.02 ± 1.04	58.51 ± 1.03	61.03 ± 1.35	53.67 ± 0.58	54.90 ± 0.60

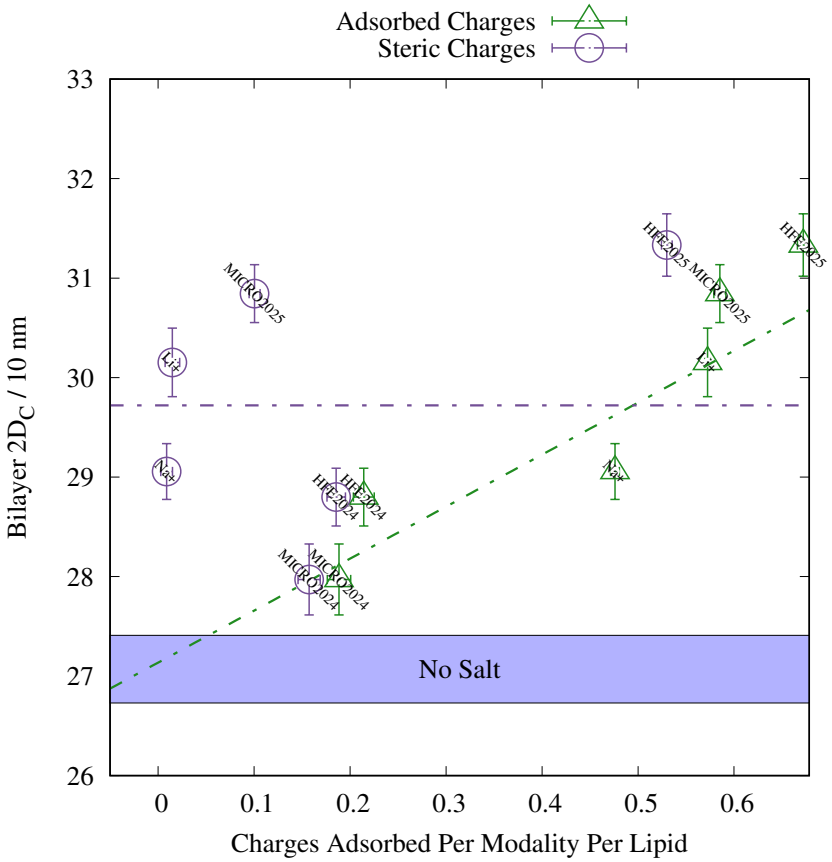

Figure 4.8: Adsorbed charge per adsorption modality per lipid as a function of the lipid bilayer hydrocarbon thickness $2D_C$. We compare both our results from this work, and our previous work with monovalent ions.[102] There is a clear trend in the total number of adsorbed charges (i.e. any charges not in bulk solvent), where more charges results in a greater $2D_C$. However, if one examines the sterically adsorbed charges, the trend is not as strong. This seems to indicate that the non-steric charges are most responsible for the pertubation of the bilayer thickness from that of the no-salt simulation shown as the blue region on the plot.

4.7 Conclusions

We have presented a comparison between two Mg^{2+} parameter sets developed by our group, under two different water–ion interaction models. The Mg^{2+} 2024 parameters, optimized using clusters of ions and lipid-component ligands at sub-full oxygen coordination of the ion,[102] predict steric adsorption with negligible bilayer thickening. By contrast, the Mg^{2+} 2025 parameters, optimized using fully coordinated clusters by replacing the missing ligand oxygens with waters, similar to sets of target data used to improve parameters for Mg^{2+}-nucleotide phosphate interactions,[100] yield significantly more ions in non-steric adsorption modes, greater

direct coordination with lipid phosphates, and a correlated increase in bilayer thickness. Both parameter sets reproduce their respective substitution energy targets, but the choice of partially versus fully coordinated clusters leads to divergent predictions for bilayer behavior. This raises a fundamental question about the nature of Mg^{2+} adsorption, and potentially of divalent ions in general. Both water-separated and direct-interaction adsorption modes have been described for Mg^{2+}–phosphate interactions in biological molecules,[79–82,86,89,103,108,109] and simulations with older ion models tend to favor the water-separated modes.[86,89,103,108,110] With sparse experimental data for lipid bilayers at relevant salt concentrations, it is not yet possible to judge between these models. Thus, the two parameter sets serve as complementary hypotheses and experimental targets, highlighting that the critical open question is not only which parameters best reproduce bilayer structure, but also which underlying reference chemistry most faithfully represents Mg^{2+}–lipid interactions in the condensed phase.

5 Conclusions

TODO We have introduced a framework for classifying ion adsorption at lipid bilayers based on the degree of dehydration observed in molecular dynamics simulations. This classification distinguishes between steric, imperfect, and perfect adsorption modes, corresponding to fully hydrated, partially dehydrated, and completely dehydrated ions within the hydration boundary of the bilayer.

Our results show that the electric field at the hydration shell of an ion correlates strongly with its observed mode of adsorption. Ions with high field strength, such as Mg^{2+}, remain hydrated and adsorb sterically. In contrast, Na^{+} and Li^{+} exhibit lower field strengths and bind with partial or full dehydration.

These adsorption modes are predictive of changes to bilayer structure. Systems with larger populations of imperfect or perfectly adsorbed ions display increased lipid chain order and hydrocarbon thickness. Systems dominated by steric adsorption show bilayer structures closer to the no-salt case.

The observed trends hold across multiple force-field parameterizations, including those with differing water-exchange kinetics for Mg^{2+}. Poisson–Boltzmann modeling confirms that the accumulation of ions within the hydration boundary is distinct from diffuse ionic layering predicted in the bulk.

Altogether, this work provides a mechanistic link between ion properties and lipid structural response, grounded in simulation observables. It suggests that the strength of ion adsorption—and its structural consequences—can be anticipated from the ion's electric field without requiring direct tuning to experimental constraints.

References

[1] M. Abraham, D. van der Spoel, E. Lindahl, B. Hess, the gromacs development team gromacs user manual version 5.1. 2; 2016, MJ Abraham, T. Murtola, R. Schulz, S. Páll, JC Smith, B. Hess, E. Lindahl, SoftwareX 1 (2015) 19.

[2] J. E. Jones, On the determination of molecular fields. i. from the equation of state of a gas, Proceedings of the Royal Society of London. Series A 106 (738) (1924) 441–462. doi:10.1098/rspa.1924.0081.

[3] R. A. Buckingham, The classical equation of state of gaseous helium, neon and argon, Proceedings of the Royal Society of London. Series A 168 (933) (1938) 264–283. doi:10.1098/rspa.1938.0173.

[4] M. L. Berkowitz, Biomembrane Simulations: Computational Studies of Biological Membranes, CRC Press, 2019.

[5] S. A. Pandit, H. L. Scott, Simulations and models of lipid bilayers, in: Soft Matter: Lipid Bilayers and Red Blood Cells, Vol. 4, Wiley Online Library, 2008, Ch. 1, pp. 1–82.

[6] J. Kruczek, S.-W. Chiu, E. Jakobsson, S. A. Pandit, Effects of lithium and other monovalent ions on palmitoyl oleoyl phosphatidylcholine bilayer, Langmuir 33 (4) (2017) 1105–1115.
URL http://dx.doi.org/10.1021/acs.langmuir.6b04166

[7] J. Kruczek, S.-W. Chiu, S. Varma, E. Jakobsson, S. A. Pandit, Interactions of monovalent and divalent cations at palmitoyl-oleoyl-phosphatidylcholine interface, Langmuir 35 (32) (2019) 10522–10532.

[8] M. Saunders, M. Steele, W. Lavigne, S. Varma, S. A. Pandit, Interaction of salt with ether-and ester-linked phospholipid bilayers, Biochimica et Biophysica Acta (BBA)-Biomembranes 1861 (5) (2019) 907–915.

[9] R. A. Böckmann, A. Hac, T. Heimburg, H. Grubmüller, Effect of sodium chloride on a lipid bilayer, Biophysical Journal 85 (3) (2003) 1647–1655.

[10] A. Cordomi, O. Edholm, J. J. Perez, Effect of ions on a dipalmitoyl phosphatidylcholine bilayer. a molecular dynamics simulation study, The Journal of Physical Chemistry B 112 (5) (2008) 1397–1408.

[11] A. A. Gurtovenko, I. Vattulainen, Effect of nacl and kcl on phosphatidylcholine and phosphatidylethanolamine lipid membranes: insight from atomic-scale simulations for understanding salt-induced effects in the plasma membrane, The Journal of Physical Chemistry B 112 (7) (2008) 1953–1962.

[12] A. Cordomi, O. Edholm, J. J. Perez, Effect of force field parameters on sodium and potassium ion binding to dipalmitoyl phosphatidylcholine bilayers, Journal of chemical theory and computation 5 (8) (2009) 2125–2134.

[13] P. Jurkiewicz, L. Cwiklik, A. Vojtíšková, P. Jungwirth, M. Hof, Structure, dynamics, and hydration of popc/pops bilayers suspended in nacl, kcl, and cscl solutions, Biochimica et Biophysica Acta (BBA)-Biomembranes 1818 (3) (2012) 609–616.

[14] G. Pabst, A. Hodzic, J. Štrancar, S. Danner, M. Rappolt, P. Laggner, Rigidification of neutral lipid bilayers in the presence of salts, Biophysical journal 93 (8) (2007) 2688–2696.

[15] H. I. Petrache, S. Tristram-Nagle, D. Harries, N. Kučerka, J. F. Nagle, V. A. Parsegian, Swelling of phospholipids by monovalent salt, Journal of lipid research 47 (2) (2006) 302–309.

[16] D. Uhríková, N. Kučerka, J. Teixeira, V. Gordeliy, P. Balgavỳ, Structural changes in dipalmitoylphosphatidylcholine bilayer promoted by ca2+ ions: a small-angle neutron scattering study, Chemistry and physics of lipids 155 (2) (2008) 80–89.

[17] I. S. Joung, T. E. Cheatham III, Determination of alkali and halide monovalent ion parameters for use in explicitly solvated biomolecular simulations, The journal of physical chemistry B 112 (30) (2008) 9020–9041.

[18] S.-W. Chiu, S. A. Pandit, H. Scott, E. Jakobsson, An improved united atom force field for simulation of mixed lipid bilayers, The Journal of Physical Chemistry B 113 (9) (2009) 2748–2763.

[19] S. Varma, S. B. Rempe, Multibody effects in ion binding and selectivity, Biophysical journal 99 (10) (2010) 3394–3401.

[20] V. Wineman-Fisher, Y. Al-Hamdani, I. Addou, A. Tkatchenko, S. Varma, Ion-hydroxyl interactions: From high-level quantum benchmarks to transferable polarizable force fields, Journal of chemical theory and computation 15 (4) (2019) 2444–2453.

[21] R. Vácha, P. Jurkiewicz, M. Petrov, M. L. Berkowitz, R. A. Bockmann, J. Barucha-Kraszewska, M. Hof, P. Jungwirth, Mechanism of interaction of monovalent ions with phosphatidylcholine lipid membranes, The Journal of Physical Chemistry B 114 (29) (2010) 9504–9509.

[22] I. Vorobyov, T. W. Allen, The electrostatics of solvent and membrane interfaces and the role of electronic polarizability, The Journal of Chemical Physics 132 (18) (2010) 05B602.

[23] J. Melcr, H. Martinez-Seara, R. Nencini, J. Kolafa, P. Jungwirth, O. S. Ollila, Accurate binding of sodium and calcium to a popc bilayer by effective inclusion of electronic polarization, The Journal of Physical Chemistry B 122 (16) (2018) 4546–4557.

[24] P. Chen, I. Vorobyov, B. Roux, T. W. Allen, Molecular dynamics simulations based on polarizable models show that ion permeation interconverts between different mechanisms as a function of membrane thickness, The Journal of Physical Chemistry B 125 (4) (2021) 1020–1035.

[25] G. Lee Warren, J. E. Davis, S. Patel, Origin and control of superlinear polarizability scaling in chemical potential equalization methods, The Journal of chemical physics 128 (14) (2008) 144110.

[26] D. Boda, D. Henderson, The effects of deviations from lorentz–berthelot rules on the properties of a simple mixture, Molecular Physics 106 (20) (2008) 2367–2370.

[27] C. M. Baker, P. E. Lopes, X. Zhu, B. Roux, A. D. MacKerell Jr, Accurate calculation of hydration free energies using pair-specific lennard-jones parameters in the charmm drude polarizable force field, Journal of chemical theory and computation 6 (4) (2010) 1181–1198.

[28] J. Yoo, A. Aksimentiev, Improved parametrization of li+, na+, k+, and mg2+ ions for all-atom molecular dynamics simulations of nucleic acid systems, The journal of physical chemistry letters 3 (1) (2012) 45–50.

[29] M. Fyta, R. R. Netz, Ionic force field optimization based on single-ion and ion-pair solvation properties: Going beyond standard mixing rules, The Journal of chemical physics 136 (12) (2012) 124103.

[30] S. Mamatkulov, M. Fyta, R. R. Netz, Force fields for divalent cations based on single-ion and ion-pair properties, The Journal of chemical physics 138 (2) (2013) 024505.

[31] R. M. Venable, Y. Luo, K. Gawrisch, B. Roux, R. W. Pastor, Simulations of anionic lipid membranes: development of interaction-specific ion parameters and validation using nmr data, The journal of physical chemistry B 117 (35) (2013) 10183–10192.

[32] A. Savelyev, A. D. MacKerell Jr, Balancing the interactions of ions, water, and dna in the drude polarizable force field, The Journal of Physical Chemistry B 118 (24) (2014) 6742–6757.

[33] H. Li, V. Ngo, M. C. Da Silva, D. R. Salahub, K. Callahan, B. Roux, S. Y. Noskov, Representation of ion–protein interactions using the drude polarizable force-field, The Journal of Physical Chemistry B 119 (29) (2015) 9401–9416.

[34] A. Savelyev, A. D. MacKerell Jr, Competition among li+, na+, k+, and rb+ monovalent ions for dna in molecular dynamics simulations using the additive charmm36 and drude polarizable force fields, The Journal of Physical Chemistry B 119 (12) (2015) 4428–4440.

[35] Z. Jing, R. Qi, C. Liu, P. Ren, Study of interactions between metal ions and protein model compounds by energy decomposition analyses and the amoeba force field, The Journal of chemical physics 147 (16) (2017) 161733.

[36] M. M. Reif, C. Kallies, V. Knecht, Effect of sodium and chloride binding on a lecithin bilayer. a molecular dynamics study, Membranes 7 (1) (2017) 5.

[37] J. C. Fogarty, S.-W. Chiu, P. Kirby, E. Jakobsson, S. A. Pandit, Automated optimization of water–water interaction parameters for a coarse-grained model, The Journal of Physical Chemistry B 118 (6) (2014) 1603–1611.

[38] J. C. Fogarty, High Dimensional Non-Linear Optimization of Molecular Models, University of South Florida, 2014.

[39] S. Varma, S. B. Rempe, Coordination numbers of alkali metal ions in aqueous solutions, Biophysical chemistry 124 (3) (2006) 192–199.

[40] P. Mason, S. Ansell, G. Neilson, Neutron diffraction studies of electrolytes in null water: a direct determination of the first hydration zone of ions, Journal of Physics: Condensed Matter 18 (37) (2006) 8437.

[41] M. Galib, M. Baer, L. Skinner, C. Mundy, T. Huthwelker, G. Schenter, C. Benmore, N. Govind, J. L. Fulton, Revisiting the hydration structure of aqueous na+, The Journal of chemical physics 146 (8) (2017) 084504.

[42] J. Timko, D. Bucher, S. Kuyucak, Dissociation of nacl in water from ab initio molecular dynamics simulations, The Journal of chemical physics 132 (11) (2010) 114510.

[43] P. Smirnov, Structure of the nearest environment of na+, k+, rb+, and cs+ ions in oxygen-containing solvents, Russian Journal of General Chemistry 90 (9) (2020) 1693–1702.

[44] V. Blum, R. Gehrke, F. Hanke, P. Havu, V. Havu, X. Ren, K. Reuter, M. Scheffler, Ab initio molecular simulations with numeric atom-centered orbitals, Computer Physics Communications 180 (11) (2009) 2175–2196.

[45] J. P. Perdew, K. Burke, M. Ernzerhof, Generalized gradient approximation made simple, Physical review letters 77 (18) (1996) 3865.

[46] C. Adamo, V. Barone, Toward reliable density functional methods without adjustable parameters: The pbe0 model, The Journal of chemical physics 110 (13) (1999) 6158–6170.

[47] A. Tkatchenko, M. Scheffler, Accurate molecular van der waals interactions from ground-state electron density and free-atom reference data, Physical review letters 102 (7) (2009) 073005.

[48] V. Wineman-Fisher, J. M. Delgado, P. R. Nagy, E. Jakobsson, S. A. Pandit, S. Varma, Transferable interactions of li+ and mg2+ ions in polarizable models, The Journal of Chemical Physics 153 (10) (2020) 104113.

[49] V. Wineman-Fisher, Y. Al-Hamdani, P. R. Nagy, A. Tkatchenko, S. Varma, Improved description of ligand polarization enhances transferability of ion–ligand interactions, The Journal of Chemical Physics 153 (9) (2020) 094115.

[50] M. J. Abraham, T. Murtola, R. Schulz, S. Páll, J. C. Smith, B. Hess, E. Lindahl, Gromacs: High performance molecular simulations through multi-level parallelism from laptops to supercomputers, SoftwareX 1 (2015) 19–25.

[51] S. Pall, M. J. Abraham, C. Kutzner, B. Hess, E. Lindahl, Tackling exascale software challenges in molecular dynamics simulations with gromacs, in: International Conference on Exascale Applications and Software, Springer, 2014, pp. 3–27.

[52] D. V. D. Spoel, E. Lindahl, B. Hess, G. Groenhof, A. Mark, H. Berendsen, Gromacs: fast, flexible, free, J. Comput. Chem. 26 (2005) 1701.

[53] E. Lindahl, B. Hess, D. Van Der Spoel, Gromacs 3.0: a package for molecular simulation and trajectory analysis, Molecular modeling annual 7 (8) (2001) 306–317.

[54] H. J. Berendsen, D. van der Spoel, R. van Drunen, Gromacs: a message-passing parallel molecular dynamics implementation, Computer Physics Communications 91 (1-3) (1995) 43–56.

[55] H. Berendsen, J. Grigera, T. Straatsma, The missing term in effective pair potentials, Journal of Physical Chemistry 91 (24) (1987) 6269–6271.

[56] S. Nosé, M. Klein, Constant pressure molecular dynamics for molecular systems, Molecular Physics 50 (5) (1983) 1055–1076.

[57] M. Parrinello, A. Rahman, Polymorphic transitions in single crystals: A new molecular dynamics method, Journal of Applied physics 52 (12) (1981) 7182–7190.

[58] B. Hess, H. Bekker, H. J. C. Berendsen, J. G. E. M. Fraaije, Lincs: A linear constraint solver for molecular simulations, Journal of Computational Chemistry 18 (12) (1997)

1463–1472.
URL http://dx.doi.org/10.1002/(SICI)1096-987X(199709)18:12<1463::AID-JCC4>3.0.CO;2-H

[59] U. Essmann, L. Perera, M. L. Berkowitz, T. Darden, H. Lee, L. G. Pedersen, A smooth particle mesh ewald method, The Journal of chemical physics 103 (19) (1995) 8577–8593.

[60] H. I. Petrache, S. E. Feller, J. F. Nagle, Determination of component volumes of lipid bilayers from simulations., Biophysical Journal 72 (5) (1997) 2237–2242.
URL http://www.ncbi.nlm.nih.gov/pmc/articles/PMC1184418/

[61] J. F. Nagle, S. Tristram-Nagle, Structure of lipid bilayers, Biochimica et Biophysica Acta (BBA)-Reviews on Biomembranes 1469 (3) (2000) 159–195.

[62] J. C. Fogarty, M. Arjunwadkar, S. A. Pandit, J. Pan, Atomically detailed lipid bilayer models for the interpretation of small angle neutron and x-ray scattering data, Biochimica et Biophysica Acta (BBA)-Biomembranes 1848 (2) (2015) 662–672.

[63] E. Egberts, H. Berendsen, Molecular dynamics simulation of a smectic liquid crystal with atomic detail, The Journal of chemical physics 89 (6) (1988) 3718–3732.

[64] J.-P. Douliez, A. Leonard, E. J. Dufourc, Restatement of order parameters in biomembranes: calculation of cc bond order parameters from cd quadrupolar splittings., Biophysical journal 68 (5) (1995) 1727.

[65] S. Varma, S. B. Rempe, Structural transitions in ion coordination driven by changes in competition for ligand binding, Journal of the American Chemical Society 130 (46) (2008) 15405–15419.

[66] K. Åman, E. Lindahl, O. Edholm, P. Håkansson, P.-O. Westlund, Structure and dynamics of interfacial water in an l α phase lipid bilayer from molecular dynamics simulations, Biophysical journal 84 (1) (2003) 102–115.

[67] J. N. Israelachvili, Intermolecular and surface forces, Academic press, 2011.

[68] O. Stern, The theory of the electrolytic double-layer, Z. Elektrochem 30 (508) (1924) 1014–1020.

[69] D. C. Grahame, The electrical double layer and the theory of electrocapillarity., Chemical reviews 41 (3) (1947) 441–501.

[70] M. C. Smith, R. M. Crist, J. D. Clogston, S. E. McNeil, Zeta potential: a case study of cationic, anionic, and neutral liposomes, Analytical and bioanalytical chemistry 409 (2017) 5779–5787.

[71] J. Marra, J. Israelachvili, Direct measurements of forces between phosphatidylcholine and phosphatidylethanolamine bilayers in aqueous electrolyte solutions, Biochemistry 24 (17) (1985) 4608–4618.

[72] J. Pan, F. A. Heberle, S. Tristram-Nagle, M. Szymanski, M. Koepfinger, J. Katsaras, N. Kucerka, Molecular structures of fluid phase phosphatidylglycerol bilayers as determined by small angle neutron and x-ray scattering, Biochimica et Biophysica Acta (BBA)-Biomembranes 1818 (9) (2012) 2135–2148.

[73] J. Pan, X. Cheng, F. A. Heberle, B. Mostofian, N. Kucerka, P. Drazba, J. Katsaras, Interactions between ether phospholipids and cholesterol as determined by scattering and molecular dynamics simulations, The Journal of Physical Chemistry B 116 (51) (2012) 14829–14838.

[74] H. Casal, H. Mantsch, H. Hauser, Infrared and 31p-nmr studies of the interaction of mg2+ with phosphatidylserines: effect of hydrocarbon chain unsaturation, Biochimica et Biophysica Acta (BBA)-Biomembranes 982 (2) (1989) 228–236.

[75] S. A. Pandit, D. Bostick, M. L. Berkowitz, Molecular dynamics simulation of a dipalmitoylphosphatidylcholine bilayer with nacl, Biophysical journal 84 (6) (2003) 3743–3750.

[76] M. L. Berkowitz, D. L. Bostick, S. Pandit, Aqueous solutions next to phospholipid membrane surfaces: insights from simulations, Chemical reviews 106 (4) (2006) 1527–1539.

[77] V. Kalinin, C. Radke, An ion-binding model for ionic surfactant adsorption at aqueous-fluid interfaces, Colloids and Surfaces A: Physicochemical and Engineering Aspects 114 (1996) 337–350.

[78] M. Saunders, V. Wineman-Fisher, E. Jakobsson, S. Varma, S. A. Pandit, High-dimensional parameter search method to determine force field mixing terms in molecular simulations, Langmuir 38 (9) (2022) 2840–2851.

[79] J. C. Bowman, T. K. Lenz, N. V. Hud, L. D. Williams, et al., Cations in charge: magnesium ions in rna folding and catalysis, Current opinion in structural biology 22 (3) (2012) 262.

[80] L. Rulíšek, J. Šponer, Outer-shell and inner-shell coordination of phosphate group to hydrated metal ions (mg2+, cu2+, zn2+, cd2+) in the presence and absence of nucleobase. the role of nonelectrostatic effects, The Journal of Physical Chemistry B 107 (8) (2003) 1913–1923.

[81] T. Dudev, Lin, M. Dudev, C. Lim, First- second shell interactions in metal binding sites in proteins: A pdb survey and dft/cdm calculations, Journal of the American Chemical Society 125 (10) (2003) 3168–3180.

[82] D. Pörschke, The mode of mg++ binding to oligonucleotides. inner sphere complexes as markers for recognition?, Nucleic Acids Research 6 (3) (1979) 883–898.

[83] A. S. Petrov, J. Funseth-Smotzer, G. R. Pack, Computational study of dimethyl phosphate anion and its complexes with water, magnesium, and calcium, International journal of quantum chemistry 102 (5) (2005) 645–655.

[84] P. Li, B. P. Roberts, D. K. Chakravorty, K. M. Merz Jr, Rational design of particle mesh ewald compatible lennard-jones parameters for+ 2 metal cations in explicit solvent, Journal of chemical theory and computation 9 (6) (2013) 2733–2748.

[85] K. K. Grotz, N. Schwierz, Optimized magnesium force field parameters for biomolecular simulations with accurate solvation, ion-binding, and water-exchange properties in spc/e, tip3p-fb, tip4p/2005, tip4p-ew, and tip4p-d, Journal of Chemical Theory and Computation 18 (1) (2021) 526–537.

[86] K. K. Grotz, S. Cruz-León, N. Schwierz, Optimized magnesium force field parameters for biomolecular simulations with accurate solvation, ion-binding, and water-exchange properties, Journal of Chemical Theory and Computation 17 (4) (2021) 2530–2540.

[87] N. Michaud-Agrawal, E. J. Denning, T. B. Woolf, O. Beckstein, Mdanalysis: a toolkit for the analysis of molecular dynamics simulations, Journal of computational chemistry 32 (10) (2011) 2319–2327.

[88] R. J. Gowers, M. Linke, J. Barnoud, T. J. E. Reddy, M. N. Melo, S. L. Seyler, J. Domanski, D. L. Dotson, S. Buchoux, I. M. Kenney, et al., Mdanalysis: a python package for the rapid analysis of molecular dynamics simulations, Tech. rep., Los Alamos National lab.(LANL), Los Alamos, NM (United States) (2019).

[89] O. Allnér, L. Nilsson, A. Villa, Magnesium ion–water coordination and exchange in biomolecular simulations, Journal of chemical theory and computation 8 (4) (2012) 1493–1502.

[90] J. Kruczek, M. Saunders, M. Khosla, Y. Tu, S. A. Pandit, Molecular dynamics simulations of ether-and ester-linked phospholipids, Biochimica et Biophysica Acta (BBA)-Biomembranes 1859 (12) (2017) 2297–2307.

[91] M. R. Reddy, M. Berkowitz, The dielectric constant of spc/e water, Chemical physics letters 155 (2) (1989) 173–176.

[92] S. Kurakin, O. Ivankov, V. Skoi, A. Kuklin, D. Uhríková, N. Kučerka, Cations do not alter the membrane structure of popc—a lipid with an intermediate area, Frontiers in Molecular Biosciences 9 (2022) 926591.

[93] S. Kurakin, E. Ermakova, A. Ivankov, S. Smerdova, N. Kučerka, The effect of divalent ions on the structure of bilayers in the dimyristoylphosphatidylcholine vesicles, Journal of Surface Investigation: X-ray, Synchrotron and Neutron Techniques 15 (2021) 211–220.

[94] A. Romani, A. Scarpa, Regulation of cell magnesium, Archives of biochemistry and biophysics 298 (1) (1992) 1–12.

[95] J. Neely, R. Connick, Rate of water exchange from hydrated magnesium ion, Journal of the American Chemical Society 92 (11) (1970) 3476–3478.

[96] G. Pálinkás, T. Radnai, Hydration shell structures in an mgcl2 solution from x-ray and md studies, Zeitschrift für Naturforschung A 37 (1982) 1049–1060, provides structural evidence of a highly rigid, octahedral hydration shell around Mg2+, consistent with very long water residence times, though no explicit value is given. doi:10.1515/zna-1982-0912.
URL https://consensus.app/papers/hydration-shell-structures-in-an-mgcl2-solution-from-xray-pÃąli
16b7c39c6b6a50828119dbe4c293bfda/?utm_source=chatgpt

[97] A. Bleuzen, P.-A. Pittet, L. Helm, A. E. Merbach, Water exchange on magnesium (ii) in aqueous solution: a variable temperature and pressure 17o nmr study, Magnetic resonance in chemistry 35 (11) (1997) 765–773.

[98] J. N. Sachs, H. Nanda, H. I. Petrache, T. B. Woolf, Changes in phosphatidylcholine headgroup tilt and water order induced by monovalent salts: molecular dynamics simulations, Biophysical journal 86 (6) (2004) 3772–3782.

[99] G. Pabst, A. Hodzic, J. Štrancar, S. Danner, M. Rappolt, P. Laggner, Rigidification of neutral lipid bilayers in the presence of salts, Biophysical journal 93 (8) (2007) 2688–2696.

[100] J. M. Delgado, P. R. Nagy, S. Varma, Polarizable amoeba model for simulating mg2+· protein· nucleotide complexes, Journal of Chemical Information and Modeling 64 (2) (2023) 378–392.

[101] J. M. Delgado, P. S. Klein, S. Varma, Atp-ion complexation and lithium's bioactive form in cellular solutions, Journal of the American Chemical Society 147 (22) (2025) 19061–19072, pMID: 40405352. arXiv:https://doi.org/10.1021/jacs.5c04061, doi:10.1021/jacs.5c04061.
URL https://doi.org/10.1021/jacs.5c04061

[102] M. Saunders, A. Adekoya-Olowofela, S. Downing, S. A. Pandit, Adsorption modes of na+, li+, and mg2+ to a model zwitterionic lipid bilayer, Langmuir 40 (49) (2024) 25892–25901.

[103] K. K. Grotz, N. Schwierz, Optimized magnesium force field parameters for biomolecular simulations with accurate solvation, ion-binding, and water-exchange properties in spc/e, tip3p-fb, tip4p/2005, tip4p-ew, and tip4p-d, Journal of Chemical Theory and Computation 18 (1) (2021) 526–537.

[104] P. Li, B. P. Roberts, D. K. Chakravorty, K. M. Merz Jr, Rational design of particle mesh ewald compatible lennard-jones parameters for+ 2 metal cations in explicit solvent, Journal of chemical theory and computation 9 (6) (2013) 2733–2748.

[105] M. J. Abraham, T. Murtola, R. Schulz, S. Páll, J. C. Smith, B. Hess, E. Lindahl, Gromacs: High performance molecular simulations through multi-level parallelism from laptops to supercomputers, SoftwareX 1 (2015) 19–25.

[106] H. I. Petrache, S. W. Dodd, M. F. Brown, Area per lipid and acyl length distributions in fluid phosphatidylcholines determined by 2h nmr spectroscopy, Biophysical journal 79 (6) (2000) 3172–3192.

[107] J. Nagle, Area/lipid of bilayers from nmr, Biophysical journal 64 (5) (1993) 1476–1481.

[108] K. K. M. Grotz, Development of optimized magnesium force field parameters for improved simulations of magnesium-rna interactions, Ph.D. thesis, Universitätsbibliothek Johann Christian Senckenberg (2022).

[109] B. P. Fingerhut, J. Schauss, A. Kundu, T. Elsaesser, Contact pairs of rna with magnesium ions-electrostatics beyond the poisson-boltzmann equation, Biophysical Journal 120 (23) (2021) 5322–5332.

[110] J. Puyo-Fourtine, M. Juillé, J. Hénin, C. Clavaguéra, E. Duboué-Dijon, Consistent picture of phosphate–divalent cation binding from models with implicit and explicit electronic polarization, The Journal of Physical Chemistry B 126 (22) (2022) 4022–4034.